THESIS FOR THE DEGREE OF DOCTOR OF PHILOSOPHY

Cluster Effective Field Theory

Proton halos and three-body states

EMIL RYBERG

Department of Physics
CHALMERS UNIVERSITY OF TECHNOLOGY
Göteborg, Sweden 2016

Cover:
One of the log-periodic limit-cycles generated using the Cluster effective field theory formalism for the ^{6}He(0^+) bound state. See Chapter 4 for details.

Cluster Effective Field Theory
Proton halos and three-body states
Thesis for the degree of Doctor of Philosophy
EMIL RYBERG
Department of Physics
Chalmers University of Technology

Abstract

Halo nuclei are loosely bound systems consisting of a core plus valence nucleon(s). In so called Halo, or Cluster, effective field theory, the core of the halo nucleus is treated as an effective degree-of-freedom without internal structure. As such, Cluster effective field theory is a low-energy model, appropriate for the typical momentum scales of halo physics. The advantages of using effective field theory are the systematic way of improving results, by including higher orders in the momentum expansion, and the rigorous error estimates that are available at each order.

In this thesis we present a formalism for treating one-proton and two-neutron halo nuclei in effective field theory, with an emphasis on charge radii, astrophysical S-factors, and the renormalization of three-body states. We also discuss a new power-counting scheme for heavy-core systems and introduce finite-size contributions.

For one-proton halo nuclei we derive formalism for S- and P-wave systems, which we exemplify by studying the one-proton halo states $^{17}\text{F}^*$ and ^8B, respectively. Of particular significance are: (i) our calculation of the radiative capture cross section of $^{16}\text{O}(p,\gamma)^{17}\text{F}^*$ to fifth order in the S-wave system and (ii) our derivation of a leading-order correlation between the charge radius of ^8B and the threshold S-factor of $^7\text{Be}(p,\gamma)^8\text{B}$ for the P-wave system.

Our alternative power counting for halo nuclei with a heavy core leads to a new organizational principle that demotes the naive leading-order contributions to the charge radius for neutron halos. Additionally, in this new power counting we include the finite-size effects of the constituents explicitly into the field theory and derive how their finite sizes contribute to the charge radius of S- and P-wave one-neutron and one-proton halo states.

For two-neutron halo systems we derive the field-theory integral equations to study both bound and resonant states. We apply the formalism to the 0^+ channel of ^6He. In this three-body field theory we include both the $3/2^-$ and the $1/2^-$ channels of the $\alpha - n$ subsystem, together with the 0^+ channel of the $n - n$ part. Furthermore, we include the relevant three-body interactions and analyze, in particular, the renormalization of the system.

Keywords: effective field theory, nuclear physics, halo nuclei, radiative capture, charge radius, power counting, few-body physics, resonant state, renormalization

Acknowledgements

I would like to show my gratitude to:

My supervisor Christian, for all the help you have provided, through our physics discussions, your guidance, and your exemplary and thorough help with my writing. If I ever write a novel, I will ask you to proofread, just so you know. Thanks for your help in organizing the Knoxville stay. You even dared to borrow me one of your beautiful cars! And thank you for all the care you showed me during the tough times.

My supervisor Lucas, for showing me the world of effective field theory. Without your supervision and help on all the loop-diagrams I would be nowhere. I also would like to thank you for all the times that you brought me with you, to have brunch in Seattle, to visit an aquarium in Chicago, to a Thanksgiving in Milwaukee, and more. I am very grateful.

All my colleagues. Thanks for all the input and physics related discussions, and for your encouragement. But in particular, I am grateful for all the coffee breaks and let-us-eat-all-the-fruit-in-the-basket-before-it-rots occasions, with discussions of movies, society, literature, and more.

My mentor Hans-Werner. Whenever I got stuck or had a too difficult question for even my supervisors to answer, you always had a perfectly simple explanation. It has been an honor to work with you.

All my friends for, well, your friendship. Thanks for being there when the night was dark and full of terrors, but maybe most for all the sunny times, playing board games or just having lunch together.

My family, for love and support. I trust that you will all read this thesis. Otherwise, I love you still!

Anna, for everything.

LIST OF APPENDED PAPERS

This thesis consists of an extended summary and the following appended papers:

Paper A   E. Ryberg, C. Forssén, H.-W. Hammer, and L. Platter. Effective field theory for proton halo nuclei. Phys. Rev. C89 (2014), 014325

Paper B   E. Ryberg, C. Forssén, H.-W. Hammer, and L. Platter. Constraining Low-Energy Proton Capture on Beryllium-7 through Charge Radius Measurements. Eur. Phys. J. A50 (2014), 170

Paper C   E. Ryberg, C. Forssén, H.-W. Hammer, and L. Platter. Range corrections in Proton Halo Nuclei. Annals Phys. 367 (2016), 13–32

Paper D   E. Ryberg, C. Forssén, and U. van Kolck. Power Counting and Finite-Size Effects in Halo Effective Theory for Heavy-Core Systems. *In preparation.*

Paper E   E. Ryberg, C. Forssén, H.-W. Hammer, and L. Platter. Three-Body States in Cluster Effective Field Theory. *In preparation.*

Contribution report

There are several authors on the appended papers. My contributions are listed below:

A Performed the derivations and calculations of the diagrams, with input and aid from my supervisors. Participated mainly in the writing of the Theory and Results sections of the paper.

B Developed field theory formalism for the renormalization of two charged particles interacting in a P-wave. Performed the derivations and calculations of the diagrams, with input from my supervisors. Contributed to all sections in the paper, with main responsibility for the Theory and Results sections. Involved in the start-up and evolution of the project.

C Performed the derivations and calculations of the diagrams, with input from my supervisors. Contributed to the writing of all sections in the paper, with main responsibility for the Theory and Results sections. Took the initiative to write the section on fine-tuning and was in general very involved in the evolution of the project.

D Performed the derivations of the formulas. Contributed to the writing of the draft manuscript, with main responsibility for the Form factor and Results sections. Played a large part in the start-up and evolution of the project.

E Performed the derivations of the diagrams and evaluated the resulting amplitude, with input and aid from my supervisors. Took main responsibility for the writing of the manuscript.

CONTENTS

Part I
Extended Summary

1 Introduction

Models are used in all of the natural sciences to interpret results and make predictions. As such, the obtained results will be model dependent to a certain degree. In an effective field theory (EFT) framework, these model dependencies are made as transparent as possible and the uncertainties due to the choice of model can be reduced systematically. The general aim of this thesis is therefore to exploit these strengths of the EFT framework to make model-independent predictions of physical systems with associated error estimates.

In particular, this doctorate thesis presents an application of EFT to describe exotic nuclear systems known as halo nuclei, or more precisely to one-proton and two-neutron halo nuclei. In this first chapter we will introduce concepts of nuclear physics and EFT that will be relevant for the remainder of the thesis.

Nuclear physics is the field in which the constituents of atomic nuclei and their interactions are studied. The basic constituents of nuclei are protons and neutrons, commonly refered to as nucleons. However, through the interactions of nucleons, mediated by mesons, for example pions, one might argue that the ingredients of an atomic nucleus are more involved. One can think of the nucleus as consisting of nucleons living in a sea of pions. As such, the notions of constituents and interactions are tied tightly together. We will therefore introduce the concept of degree-of-freedom, which is very similar to that of constituent, with the difference that a degree-of-freedom is something that is chosen; it is one of the ingredients that defines the model we are working with to describe Nature. Thus, with a given number of degrees-of-freedom one can write down all the possible interactions between them. For example, a model with only the nucleons as degrees-of-freedom will only have contact interactions between these nucleons, while a model with pions included will also have pion-nucleon and pion-pion interactions.

In Nature we have a large amount of different mesons other than the pions, and there are also excitations of the nucleons that could be included as degrees-of-freedom. This raises questions about how the degrees-of-freedom should be chosen; should quarks and gluons be included? The quarks are confined within the pions and the nucleons and are only made visible on the GeV scale, a scale high enough for nucleons to be created out of vacuum. Therefore, although quarks and gluons are the degrees-of-freedom of quantum chromodynamics (QCD), they are not directly relevant for nuclear physics. Though, for example in Chiral EFT, the symmetries of QCD are used to constrain the possible interactions between nucleons and mesons. Note also that even though quarks and gluons are not relevant degrees-of-freedom for nuclear physics, it is a necessity to understand how these combine into nucleons and mesons, if one wants to bridge the gap between QCD and nuclear physics.

What about a model with only nucleons as degrees-of-freedom? Such a model would, as stated above, only have contact interactions between the nucleons. These contact interactions have a typical range of ~ 1 fm, since the nucleons are extended objects with

this size. In such a model we can not really ask questions about the internal structure of the nucleons, since then we will run into pion-physics as the pion mass[1] is about 140 MeV = $(1.4 \text{ fm})^{-1}$. In a sense, the nucleon-only model breaks down around the momentum scale 140 MeV or the length scale 1.4 fm. Can such a nucleon-only model still be useful for nuclear physics? What are the relevant scales?

One important momentum scale in nuclear physics is the pion mass, which can be seen from the fact that the typical binding energy per nucleon is around or below $B \sim 10$ MeV, translating into a momentum scale $\sqrt{mB} \sim 100$ MeV, where $m \approx 939$ MeV is the nucleon mass. There are a few systems though, that can be said to have a significantly smaller momentum scale. The obvious example is the deuteron, which consists of a neutron and a proton bound together by only 2.2 MeV. Thus, for the deuteron the relevant momentum scale is of the order 45 MeV. However, for a system such as ^{4}He, where the one-nucleon separation energies and the excited states are around 20 MeV, the relevant momentum scale is around 140 MeV. This means that ^{2}H can be described accurately using only nucleons, since the relevant momentum scale is smaller than the pion mass, while it is questionable if ^{4}He can.[2] In this sense it becomes apparent that together with the choice of degrees-of-freedom is also an implicit choice of breakdown scale for the model. The concept of breakdown scale is of key importance for effective theories, which we will discuss below.

A defining property of nuclear physics is also the list of relevant observables, that is the quantities that theorists calculate and experimentalists measure. The most basic observable of nuclear physics is energy: binding energies, excitation energies, and so on. For example the 2.2 MeV binding energy of the deuteron and the first excited state energy of ^{7}Be at 0.43 MeV. Discrete quantum numbers, such as nuclear spin J and parity $\pi = \pm$, are of course also very relevant and these are usually combined in the notation J^π. Further, size and shape observables, such as the charge radius and the deformation, are often studied. The observables listed above are examples of nuclear structure observables, also called static observables. There are also dynamic observables, that is properties having to do with nuclear reactions. These can for example be cross sections for transfer reactions, capture reactions and elastic scattering. In this thesis we will present results for three-body bound and resonant states, charge radii, elastic scattering and radiative capture cross sections, while we use some energy levels and nucleon separation energies, together with J^π quantum numbers, as input for the calculations.

As have already been introduced above, the concept of basic constituents of the nucleus, or choice of degrees-of-freedom for the problem at hand, will in a sense define what possible interactions should be present in the chosen model. This will also set some limits on the possible accuracy that can be achieved. It is at this stage of the thesis that we introduce effective theories as a tool to understand nuclear physics, or physics in general. Effective theories take the view that questions about a physical property come also with a statement of the scale at which the property is measured, or viewed. For example, if asking about the potential energy due to the pull of the Earth one should also state at what height above

---

[1] We work in units where $\hbar = c = 1$ and we use MeV fm = 197.327 to convert energy into length.

[2] Note however that ^{4}He have actually been considered at LO in Pionless EFT, with promising results [1]. It will be interesting to see how the continued effort with the inclusion of effective-range corrections influence this result.

the Earth's surface (at radius R), the question is asked. This, since for high altitudes h above the ground one must use Newton's law of gravitation $V = -GM/(R+h) + GM/R$, while close to the surface of the Earth the effective theory using the standard gravity g gives the simpler answer $V_{\text{eff}} = hg$. Of course, expanding Newton's law of gravitation for $h \ll R$, we reproduce the effective standard gravity potential, with $g = GM/R^2$, together with higher-order corrections in powers of h/R. For a large scale separation $h \ll R$ the effective description is therefore very accurate and the result can be systematically improved by including higher-order corrections. However, around $h \sim R$ all the terms in the h/R expansion will be of comparable size and therefore we say that the effective picture breaks down at the length scale R. These key concepts: effective description, separation of scales, higher-order corrections, systematic improvement and breakdown scale, are central for the method and results of this thesis. This discussion of effective theories as a way to view physics sets the foundation for the introduction of EFT in Section 1.2.

The thesis is organized as follows: In the remainder of this introductory section we discuss halo physics and EFT. In Chapter 2, we start by describing Halo, or Cluster, EFT and discuss interactions, renormalization and power counting. Then we move on to the study of heavy-core effects and how these modify the power counting, with focus on finite-size effects and short-range contributions to the observable charge radius. This part of Chapter 2 is based on Paper D. In Chapter 3 we present our work on one-proton halo nuclei. The observables that we consider are charge radii, radiative capture cross sections and low-energy elastic scattering parameters. The first part of Chapter 3, on S-wave one-proton halo nuclei, is based on Paper A and Paper C, while the second part, on P-wave one-proton halo nuclei, is based on Paper B. Next, in Chapter 4 we derive the three-body scattering amplitudes relevant for low-lying states in ^{6}He and we present a renormalization analysis. A summary of the appended papers is given in Chapter 5. Finally, in Chapter 6 we summarize the thesis with a discussion of Halo EFT and our results, and provide an outlook.

1.1 Halo physics

The word halo comes from the ancient Greek word hálōs, which is used to describe the optical phenomenon of a circle of light around the sun or the moon. In nuclear physics, a halo nucleus has nothing to do with astronomy, but rather denotes a nucleus that has a few of its nucleons located at larger distances than the remaining ones in the core. One says that these outer nucleons form a nuclear halo around the core. Halo states were first discovered by Tanihata et al [2] and Hansen and Jonson [3]. In Nature there are both one-nucleon and many-nucleon halos, for example the one-neutron halo nucleus ^{11}Be, which can be seen as consisting of a tightly bound ^{10}Be core and a loosely bound single neutron, and the two-neutron halo ^{6}He, consisting of two valence neutrons orbiting the ^{4}He core. For an early review on halo physics, see for example Ref. [4].

However, the statement that a few of the nucleons are located in a halo around the core is not completely accurate. We can not really measure the position of individual nucleons in the nucleus. What we mean is strictly speaking that the wavefunction of the

halo nucleus is very extended compared to the wavefunction of the core by itself, and that the system is close to a few-nucleon threshold. Connecting this situation to observables one can, for example, characterize a halo nucleus by properties such as a large charge radius and small one-nucleon, or few-nucleon, separation energies.

A typical one-nucleon halo nucleus consists of a tightly bound core with a loosely bound nucleon attached. The typical one-nucleon separation energy is around $S_N \sim 0.1$–1 MeV. The core itself consists of several nucleons and these inner nucleons have momenta which are nuclear-physics-like, that is of order the pion mass. The point here is that the momentum of the valence nucleon, with respect to the core, is very small. Thus, viewing the core as structureless, the relevant momentum scale for the nuclear halo is $\sqrt{mS_N} \sim 10$–30 MeV, which is much smaller than the pion mass. The question then is whether it is actually permissible to treat the core as structureless or, at least, to which level of accuracy such a treatment works.

1.2 Effective field theory

The concept of EFTs was born with the work on effective Lagrangians by Weinberg [5] and it is strongly connected to our discussion of effective theories above. With effective we mean that we do not necessarily include all fundamental particles explicitly in our model, but modify interaction potentials to account for those missing particles. For example, weak-decay processes can be considered without using explicit vector bosons as force-mediating particles, as was done by Fermi and others in the 1930s. This was achieved using an effective coupling strength, the Fermi coupling G_F, which can be given in terms of the coupling constant of the weak force and the mass of the vector boson. That is, even though the vector bosons are not explicitly included, the interaction strengths does depend on the underlying physics. Other examples, from nuclear physics, would be the Pionless EFT, where the only explicit degrees-of-freedom are nucleons, and the Chiral EFT, where also pions are included. We will discuss the Pionless EFT in more detail below. See for example [6] for a review on EFT in general and [7] for a review on the nucleon-nucleon interaction in Chiral EFT.

The first thing to note about EFTs is that they only describe the physics below a certain high-momentum scale, which we will denote k_{hi}. The momentum k_{hi} is called the breakdown scale of the EFT. Having defined the breakdown scale, one should then include all possible degrees-of-freedom below k_{hi} and exclude all the high-momentum degrees-of-freedom. The excluded degrees-of-freedom, usually referred to as short-range or high-energy physics, are implicitly included in the EFT in the form of low-energy constants and short-range operators. The high-energy physics can be said to have been integrated out and this leaves a mark on the remaining long-range model through the modification of the interactions. To be able to remove the high-momentum physics and to define an EFT, there must be a separation of scales $k_{lo} \ll k_{hi}$, where k_{lo} is a low-momentum scale associated with the physics described by the EFT. The reason why such a separation of scales is necessary is a matter of resolution, which can be visualized by thinking in terms of wavelengths: If we measure a small object with low-momentum light, we will not be able to resolve the internal structure of the object since the wavelength is too large. For

very low-momentum probes we might not even see the object as anything else than a point-like particle. Therefore, we are not able to resolve the short-range physics if the momentum is smaller than k_{hi}.

In this thesis we use EFT, which means that we work in a quantum field theory, with Lagrangians and quantum fields. The quantum field theory formalism is frequently used for relativistic theories, for example the Standard Model for particle physics. However, in this thesis we will only work in the non-relativistic limit of quantum field theory, which in principle is equivalent to a standard Schrödinger-equation formalism. The reason why we still choose to use quantum field theory is because it provides a more straightforward way to improve on the theory by including higher-order corrections systematically. For example, the concept of short-range operators is much more natural in a quantum field theory and therefore this framework is convenient for developing effective theories.

The Lagrangian[3] is an energy functional, with dimension energy/volume. Length quantities scale as an inverse momentum while energies scale as momentum squared in a non-relativistic theory. This means that the Lagrangian has scaling dimension equal to 5. The Lagrangian contains both the kinetic-energy density terms of all the included fields, and all the possible interaction terms between these fields. If we, for example, choose the nucleons as our only degrees-of-freedom, we will only have nucleon-nucleon interactions. For such a model the Lagrangian is

$$\mathcal{L} = N^\dagger \left[i\partial_t + \frac{\nabla^2}{2m} + \ldots \right] N - N^\dagger N^\dagger \hat{V}_2 NN - N^\dagger N^\dagger N^\dagger \hat{V}_3 NNN - \ldots \ , \qquad (1.1)$$

where N is the nucleon field, $\hat{V}_2$ is the two-body interaction potential, $\hat{V}_3$ is the three-body interaction potential, and so on. In the Lagrangian (1.1) we have suppressed both spin and isospin indices on the nucleon fields as well as on the interaction potentials. The first term, in square brackets, is the kinetic term and the dots refer to relativistic corrections to the Schrödinger kinetic-energy operator. The dots at the far right indicate that there exist many-body interactions to arbitrary number of nucleons. Note, however, that only the $\hat{V}_2$ interaction potential will contribute if only two nucleons in total are present in the system. Since the Lagrangian (1.1) has scaling dimension 5 and ∂_t is of dimension 2, the nucleon field must have scaling dimension 3/2 (note that powers of the nucleon mass does not contribute to the scaling dimension in a non-relativistic nuclear physics theory).

By expanding the interaction potentials in powers of momentum and keeping only the leading terms, we arrive at what we denote leading-order (LO) in the EFT. As we have excluded contributions one order up in powers of k_{lo}/k_{hi} we expect that this approximation generates an error that is proportional to this ratio. The momentum ratio k_{lo}/k_{hi} is generally called the EFT expansion parameter. If we choose to include the first two terms in the expansion we are doing a next-to-leading order (NLO) calculation, with expected EFT error $(k_{lo}/k_{hi})^2$; include yet an additional order and we are at next-to-next-to-leading order (N^{2}LO), and so on. This way of organizing the EFT is called power counting. For the pionless Lagrangian (1.1) the LO term of the S-wave two-body interaction would just be a constant in momentum space while the NLO term would be given by a momentum-squared operator. In coordinate space, these first two interactions

---

[3]When we use the word Lagrangian we really mean Lagrangian density.

would correspond to a Dirac delta interaction, $\delta(\mathbf{r})$, and a nabla-squared acting on a Dirac delta, $\nabla^2\delta(\mathbf{r})$.

Note that since the Lagrangian (1.1) includes terms of high dimension, it describes what is typically, but inappropriately, called a *non-renormalizable* field theory. While renormalizable theories only need a finite number of counter terms to absorb divergences, the *non-renormalizable* ones need an infinite amount of counter terms. This would indicate a problem of non-predictability. However, this is not the case if an effective perspective is taken. The reason why one can still make predictions using *non-renormalizable* field theories is that only a finite number of counter terms are needed at each order in the momentum expansion. As such, a *non-renormalizable* theory is renormalizable order-by-order and predictions can be made in regimes where the momentum is smaller than the breakdown scale. The Standard Model of particle physics, which is a renormalizable field theory, can as such in principle be valid for all momenta. However, when searching for physics beyond the Standard Model, effective higher-dimension operators are used. Furthermore, the effective description of the weak-decay process mentioned above is given by a *non-renormalizable* field theory and it is valid below the mass of the vector bosons. Even an effective quantum field theory of gravity is predictive [8], but only well below the Planck mass. As such, it should now be clear that the concept of *non-renormalizable* field theories make no sense in effective descriptions of Nature: it is a misnomer. And to emphasize this point, let us quote Weinberg [9]: "Non-renormalizable theories, I realized, are just as renormalizable as renormalizable theories."

Even though it is true that *non-renormalizable* effective theories are renormalizable, they may still be more complicated than so called renormalizable field theories. This is mainly due to the fact that they typically have more parameters and these must be fixed to data before predictions can be made. For example, for some observables we may even run into a road block at a certain order in the form of a short-range operator, entering with an undetermined parameter that we can not fit to data. This can either be due to practical reasons, such as the lack of appropriate data, or formal reasons, such as the short-range parameter appearing only for the observable under consideration. In such a scenario one can say that there is an upper limit on the precision that the EFT can achieve. We will discuss such cases in Chapter 3.

Parallel to the EFT expansion is the effective range expansion (ERE). The ERE is a way to describe low-energy elastic scattering of two particles in terms of only a few low-energy elastic scattering parameters. These parameters are the scattering length a, the effective range r, the shape parameter P, and so on. The range of the interaction needs to be finite for the ERE to be well defined and the size of the ERE parameters is typically related to the range. The defining equation for the low-energy elastic scattering parameters is the momentum expansion of $\cot(\delta)$, where δ is the phase shift:

$$k^{2l+1}\cot(\delta_l) = -\frac{1}{a_l} + \frac{1}{2}r_l k^2 + P_l k^4 + \dots \tag{1.2}$$

In Eq. (1.2) we have included the angular momentum quantum number l as a subscript on the parameters and the phase shift, to make the defining equation more general.

The phase shift can be related to the differential elastic scattering cross section

according to

$$\frac{d\sigma}{d\Omega} = \left| \frac{1}{k} \sum_{l=0}^{\infty} (2l+1) \exp{(i\delta_l)} \sin{(\delta_l)} P_l(\cos\theta) \right|^2 , \qquad (1.3)$$

where $P_l(x)$ is the lth Legendre polynomial. Eq. (1.3) implies that if a momentum expansion is made, and only the zeroth-order term is kept, then the total cross section in the low-momentum limit is given by

$$\sigma_{\text{tot}} \to 4\pi a_0^2 . \qquad (1.4)$$

Comparing Eq. (1.4) with a classical picture, with a geometrical cross section for the particles, then the $l = 0$ scattering length looks much like the radius of the particle in the extreme low-momentum regime. This geometrical picture is of course not correct in the quantum world of nuclear physics and the scattering length can be very different from the actual radius of the particle.

Coming back to EFTs, it is common to express the parameters in the EFT Lagrangian in terms of the low-energy scattering parameters. It is preferable to use actual observable quantities, such as scattering lengths and effective ranges, rather than non-observable ones, such as coefficients of the interaction terms, when discussing and analyzing the physics of the EFT. In EFTs for nuclear physics, the effective range typically scales with the high-momentum scale k_{hi}, which is to say that it scales naturally. The scattering length often scales unnaturally with the low-momentum scale k_{lo}. One would then say that the low-momentum scale emerges due to a fine-tuning in the underlying short-range physics. For example, the S-wave effective range for nucleon-nucleon elastic scattering is of the order a few femtometers, while the scattering length is of the order a few tens of femtometers in some channels. This shows the existence of a clear separation of scales in the nucleon-nucleon system, and it is this separation of scales that is the basis for many of the EFTs for nuclear physics.

In this thesis we will be concerned with the so called Halo EFT, or Cluster EFT, which is similar to the Pionless EFT in the sense that pions are excluded. However, in Halo EFT the relevant momentum scales are even lower than what they typically are in the Pionless EFT, since extremely loosely bound systems are considered. Actually, in Halo EFT not only nucleons, but also tightly bound clusters of nucleons, are used as effective degrees-of-freedom, which then puts a much more severe constraint on the model through a lower breakdown scale. This scale can be associated with the momentum scale of the inner structure of these clusters. A hint of the typical breakdown scale for Halo EFT can be given by the size of the cluster in question: If for example the cluster has a radius of about 3 fm, then this defines the breakdown scale in length and it is translated into a momentum breakdown scale of 60–70 MeV.

2 Halo/Cluster effective field theory

Halo EFT gives an effective description of halo nuclei by treating the core of the halo nucleus as an effective degree of freedom. This means that within this description the core has no internal structure; it is a basic constituent. However, it is clear that the core does consist of nucleons and therefore Halo EFT will not give a valid description of the system for momenta high enough to resolve this internal structure. This is actually not a severe restriction since much of the physics relevant to the characteristics of halo nuclei occur at very low momenta. Expressed in another way, there is a separation of scales present in halo systems such that the physics related to the structure of the core can be well separated from the relevant low-energy physics.

Halo EFT was proposed in Ref. [10] in the context of describing the two-neutron halo ^{6}He. In this paper, the resonant ^{4}He+neutron system was studied, with the purpose of using ^{5}He as a stepping stone to the more interesting ^{6}He halo nucleus. Since then, this approach to study ^{6}He has continued with efforts by several authors [11, 12, 13]. Descriptions of other two-neutron halos, using Halo EFT, can be found in Refs. [14, 15]. Halo EFT has also been applied to one-nucleon halos and few-cluster systems. In Ref. [16] the electromagnetic properties of the one-neutron halo ^{11}Be were studied. Since then even more one-neutron halo nuclei have been analyzed, see Refs. [17, 18, 19]. The cluster systems that have been considered are the resonant α-α scattering [20] and the reaction $d + t \rightarrow n + \alpha$ [21]. The reason for Halo EFT to be applicable to these non-halo systems is the existence of a separation of scales and therefore, if one was to stretch the concept of halo systems, the unbound nuclei ^{5}He and ^{8}Be can be considered as halo-like, since the α-n and α-α interactions have unnaturally large scattering lengths. A more appropriate name for this EFT is then arguably Cluster EFT, since clusters of nucleons are treated as basic constituents, and this is the name we will use in the remainder of this thesis. Much of the work done in Cluster EFT builds on the work by Ref. [22].

Our work mainly regards the treatment of one-proton halo nuclei, but we have also treated resonant states in two-neutron halo nuclei and formal aspects of heavy-core systems.

2.1 One-neutron halos in effective field theory

In Chapter 3 we will consider charged-particle systems in Cluster EFT, where both the strong nuclear force and the Coulomb interaction need to be treated non-perturbatively. And in Chapter 4 we consider two-neutron halo states, where three-body scattering diagrams need to be evaluated numerically in the presence of three-body interactions. Before turning to these more involved systems we will consider one-neutron halo systems and exemplify the approach with a derivation of the matching between the coefficients of the EFT Lagrangian and the effective-range parameters, together with an introduction to the power counting.

One-neutron halo systems such as ^{11}Be and ^{19}C can be studied in Cluster EFT [16, 18]. In ^{11}Be there are two weakly bound states, the $1/2^+$ ground state with neutron separation energy $B_0 = 0.50$ MeV, and the $1/2^-$ excited state with $B_1 = 0.18$ MeV. These halo

states can be modeled as a ^{10}Be(0^+) core field and a valence neutron field n interacting in a relative S-wave or P-wave, respectively, with an unnaturally large scattering length. The neutron separation energies are used to define the binding momenta for the ground state $\gamma_0 = \sqrt{2m_R B_0} = 29$ MeV, and for the excited state $\gamma_1 = \sqrt{2m_R B_1} = 18$ MeV, where m_R is the reduced mass of the system. For a core of mass M and a neutron of mass m, the reduced mass is given by $m_R = Mm/(M + m)$. We treat the binding momenta as our low-momentum scales, that is $\gamma_0 \sim k_{lo}$ or $\gamma_1 \sim k_{lo}$.

It is important to question the assumption of a structure-less ^{10}Be core field, that is if its internal structure is well separated from the momentum scales of the halo states. We do this by considering the first core excitation, which is a 2^+ state. The excitation energy is $E_1 = 3.4$ MeV, which defines a momentum scale corresponding to short-range physics $k_{hi} \sim \sqrt{2m_R E_1} = 76$ MeV. Thus, we note that we have a rather good separation of scales, with EFT expansion parameters $\gamma_0/k_{hi} \sim 0.4$ and $\gamma_1/k_{hi} \sim 0.2$, and that this separation is particularly good for the excited state of ^{11}Be. These EFT expansion parameters determine the rate of convergence in the order-by-order expansion and consequently also provide the uncertainty estimate.

One should also consider possible resonant states in the ^{11}Be system, since these can give short-range contributions to, for example, radiative capture cross sections. The first resonance is a $5/2^+$ state, 1.78 MeV above the ground state. Thus, for observables where this resonance can contribute, it should define the breakdown scale of the EFT. To include the resonance explicitly in a radiative capture calculation one would need to either include D-wave mixing or the 2^+ core excitation.

2.1.1 Interactions and power counting

In this section we write down the Lagrangian for a two-particle EFT, consisting of a neutron and a 0^+ core bound due to an unnaturally large scattering length. We will first consider the neutron-core interaction to be of S-wave nature and then we will continue with the more complicated P-wave system. This type of model is applicable for the two halo-states of ^{11}Be. In this section we will consider elastic scattering and charge form factor observables and, as such, it will follow the work by Hammer and Phillips [16] closely. However, we will also add on to this with our findings from Paper D.

We write the Lagrangian, relevant for the calculation of the charge form factor of the S- and P-wave one-neutron halo state, as

$$\mathcal{L} = \mathcal{L}_1 + \mathcal{L}_2 + \mathcal{L}_{EM} + \dots , \tag{2.1}$$

where $\mathcal{L}_n$ denotes the n-body part and $\mathcal{L}_{EM}$ consists of additional electromagnetic operators (both one- and two-body terms) that are not due to minimal substitution but still contribute to the charge form factor observable. The dots denote terms that are of higher order. The one-body part is given

$$\mathcal{L}_1 = n_s^\dagger \left[i D_0 + \frac{\mathbf{D}^2}{2m} \right] n_s + c^\dagger \left[i D_0 + \frac{\mathbf{D}^2}{2M} \right] c . \tag{2.2}$$

Here, n (c) denotes the neutron (core) field, with mass m (M). The covariant derivative is defined as $D_\mu = \partial_\mu + ie\hat{Q}A_\mu$, with $e > 0$ being the elementary charge, $\hat{Q}$ the charge operator and A_μ the photon four-vector.

The two-body part of the Lagrangian (2.1) is

$$\mathcal{L}_2 = \sigma_s^\dagger \left[\Delta_0 + \nu_0 \left(i\mathrm{D}_0 + \frac{\mathbf{D}^2}{2M_{\mathrm{tot}}} \right) \right] \sigma_s + \pi_s^\dagger \left[\Delta_1 + \nu_1 \left(i\mathrm{D}_0 + \frac{\mathbf{D}^2}{2M_{\mathrm{tot}}} \right) \right] \pi_s \qquad (2.3)$$

$$+ g_0 \left[\sigma_s^\dagger n_s c + \mathrm{h.c.} \right] + g_1 \left[\pi_s^\dagger \mathcal{C}_{ks'}^s c \left((1-f) i \overrightarrow{\nabla}_k - f i \overleftarrow{\nabla}_k \right) n_{s'} + \mathrm{h.c.} \right] . \qquad (2.4)$$

The auxiliary $1/2^+$ $(1/2^-)$ dicluster field σ (π) has been introduced for calculational convenience. Its propagation, together with the interaction strength g_0 (g_1), define the interaction between the neutron and the core up to the effective range. Thus, the coefficients Δ_0 and g_0 (Δ_1 and g_1) are parameters of the EFT to be fitted. The sign $\nu_0 = \pm 1$ is present to allow for both a negative and a positive effective range, since we define g_0 as purely real. The same applies to ν_1 and g_1. Note that at LO the S-wave dicluster field σ_s is static and thus the LO S-wave neutron-core interaction is $\sim g_0^2/\Delta_0$. The combination of derivative operators, using the convenient mass ratio $f = m/M_{\mathrm{tot}}$, for the P-wave interaction term makes sure that the Lagrangian is Galilean invariant. The Clebsch-Gordan coefficient is defined as $\mathcal{C}_{ks'}^s = \left\langle 1k\frac{1}{2}s' \middle| \left(1\frac{1}{2}\right) \frac{1}{2}s \right\rangle$.

The third part of the Lagrangian (2.1) consists of photon-matter interactions that are not included in $\mathcal{L}_1$ or $\mathcal{L}_2$, since they are non-minimal. Note, however, that there are additional non-minimal electromagnetic terms than those that we include in $\mathcal{L}_{\mathrm{EM}}$, but these are either higher-order or do not contribute to the charge form factor. The Lagrangian part, $\mathcal{L}_{\mathrm{EM}}$, is given by

$$\mathcal{L}_{\mathrm{EM}} = - n_s^\dagger \frac{e\rho_n^2}{6} \left[\nabla^2 A_0 - \partial_0 \left(\nabla \cdot \mathbf{A} \right) \right] n_s - c^\dagger \frac{Z_c e \rho_c^2}{6} \left[\nabla^2 A_0 - \partial_0 \left(\nabla \cdot \mathbf{A} \right) \right] c \qquad (2.5)$$

$$- \sigma_s^\dagger \frac{\nu_0 Z_{\mathrm{tot}} e \rho_\sigma^2}{6} \left[\nabla^2 A_0 - \partial_0 \left(\nabla \cdot \mathbf{A} \right) \right] \sigma_s - \pi_s^\dagger \frac{\nu_1 Z_{\mathrm{tot}} e \rho_\pi^2}{6} \left[\nabla^2 A_0 - \partial_0 \left(\nabla \cdot \mathbf{A} \right) \right] \pi_s .$$
$$(2.6)$$

As can be seen the operators are gauge invariant. Note also that they simplify in Coulomb gauge, $\nabla \cdot \mathbf{A} = 0$, and as such the relevant operators are of the form $\psi^\dagger \left(\nabla^2 A_0 \right) \psi$, for $\psi = n, c, \sigma, \pi$. The ρ-parameters are to be fitted against charge form factor observables and, actually, the ρ_n and ρ_c are the charge radii of the neutron and core, respectively. This fact can be visualized through the insight that these operators give the photon-matter Dirac-delta interactions a momentum-squared-dependent contribution, which means that these interactions get a structure, or an extent. This is exactly what a charge radius is: a modification to the trivial electric charge interaction, $\sim e \mapsto e(1 - r_{\mathrm{ch}}^2 Q^2/6)$.

Let us now have a look on the scaling dimension of all the interaction terms in the above Lagrangian (2.1), since the dimension determines at what order in the power counting an operator appears. Firstly, the dimension of the neutron and core fields is $3/2$ and the S-wave dicluster field, representing the intermediate state in the neutron-core interaction, has dimension 2 (see for example [16] for a discussion of the scalings of dicluster fields). As such, the terms in the one-body Lagrangian (2.2) has dimension 5, since $\partial_0 \sim \nabla^2$ scales as dimension 2 operators. Note also that A_0 scales as 2 and $\mathbf{A}$ is of dimension 1. In the two-body Lagrangian (2.4) there are effectively three S-wave terms: the Δ_0-term, the ν_0 term and the g_0 term. The Δ_0 term scales as 4 and the ν_0 term is at dimension
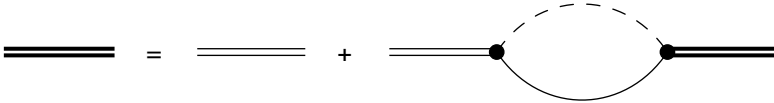
11

Figure 2.1: The full neutron-core dicluster propagator, defined recursively using the bare dicluster propagator and the irreducible self-energy.

6. The g_0 term has a scaling dimension of 5. Note that the field theory is ill-defined below dimension 5, since then the matter-fields can not propagate, nor interact. As such, dimension 5 defines LO. In the Lagrangian part (2.6) the neutron and core terms have scaling dimension 7 and the S-wave dicluster field term has dimension 8. In summary so far, at LO we only have the Lagrangian part (2.2) and the Δ_0 and g_0 terms. At NLO the ν_0 term enters the field theory and its contribution is the effective range correction as we shall see below. Then, at N^{2}LO the neutron and core $\nabla^2 A_0$ terms enter with the contribution due to the finite-size of the constituents. At N^{3}LO the dicluster $\nabla^2 A_0$ term enters and there is also an additional contribution due to the shape-parameter in the ERE at this order, which would come in as a ∇^4 term in the dicluster-term in the two-body Lagrangian (2.4).

For the P-wave system the situation is somewhat different. Firstly, in the two-body Lagrangian (2.4) the g_1 term is of dimension 5, while both the Δ_1 and ν_1 terms are of lower dimension (they are at dimension 2 and 4, respectively). As such, since LO is at dimension 5, both the Δ_1 and ν_1 terms are needed at LO. Expressed in another way, both the scattering length and the effective range are needed at LO to renormalize the interaction. In the Lagrangian part (2.6) the P-wave dicluster field term has dimension 6, which means that it enters already at NLO. The result of this is that the P-wave field theory is only predictive at LO for the charge radius.

The power counting presented above is what we refer to as the standard power counting for one-neutron halo systems. In Sec. 2.2 we will make some alterations to this power counting, due to the effect of the core mass being much heavier than the neutron mass.

2.1.2   Elastic scattering and renormalization

The Lagrangian (2.1) comes with undetermined interaction parameters and these must be fixed to observables. In such a fitting procedure we will also absorb divergences into the parameters of the EFT, giving renormalization conditions. Typically, we fix the interaction parameters to low-energy elastic-scattering observables, that is the ERE parameters. As such, we will usually derive expressions for other observables in terms of the ERE parameters. However, it is not always the case that we actually use ERE parameters as input for our calculations. It is also possible to fit to a measured or calculated asymptotic normalization coefficient (ANC), or to simply fit the interaction to an observable such as the charge radius or radiative capture cross section. Anyway, in this section we will show the renormalization of the S- and P-wave interactions in the Lagrangian (2.1) in terms of the ERE parameters.

Let us start with the S-wave interaction. From the two-body Lagrangian (2.4) we can write down the bare S-wave dicluster propagator. We can give this propagator for

any four-momentum $(E, \mathbf{p})$, but for the all the scenarios in this chapter we only need the dicluster propagator for systems where the field is at rest:

$$iD_0^{\text{bare}}(E) = iD_0^{\text{bare}}(E, \mathbf{0}) = \frac{i}{\Delta_0 + \nu_0 (E + i\varepsilon)} \tag{2.7}$$

However, the bare propagator (2.7) does not describe the full S-wave scattering process between the neutron and the core. For that we need the full dicluster propagator, which is given in Fig. 2.1. The resulting full dicluster propagator can be written as a geometrical series according to

$$iD_0(E) = \frac{i}{\Delta_0 + \nu_0 (E + i\varepsilon) + \Sigma_0(E)} \ , \tag{2.8}$$

where Σ_0 is the S-wave irreducible self-energy, definded by the neutron-core bubble in Fig. 2.1. The irreducible self-energy can be written as an integral in momentum space using the neutron and core propagators

$$iS_{\text{n}}(p_0, \mathbf{p}) = \frac{i}{p_0 - \frac{\mathbf{p}^2}{2m} + i\varepsilon} \tag{2.9}$$

and

$$iS_{\text{c}}(p_0, \mathbf{p}) = \frac{i}{p_0 - \frac{\mathbf{p}^2}{2M} + i\varepsilon} \ , \tag{2.10}$$

where $(p_0, \mathbf{p})$ is the four-momentum of the neutron or core field. The result is evaluated as

$$
\begin{aligned}
i\Sigma_0(E) &= - g_0^2 \int \frac{\mathrm{d}^4 p}{(2\pi)^4} iS_{\text{c}}(p_0, \mathbf{p}) iS_{\text{n}}(E - p_0, \mathbf{p}) \\
&= - ig_0^2 \int \frac{\mathrm{d}^3 p}{(2\pi)^3} S_{\text{tot}}(E, \mathbf{p}) \\
&= \frac{ig_0^2 m_{\text{R}}}{\pi^2} \left(L_1 - \frac{i\pi}{2} \sqrt{2m_{\text{R}} E} \right) \ .
\end{aligned}
\tag{2.11}
$$

In the first step we perform the p_0-residue integration in the lower half-plane to arrive at an integration over the two-body propagator

$$iS_{\text{tot}}(p_0, \mathbf{p}) = \frac{i}{p_0 - \frac{\mathbf{p}^2}{2m_{\text{R}}} + i\varepsilon} \ . \tag{2.12}$$

In the second step we divide the integral into two terms. The S-wave irreducible self-energy has a convergent part and a momentum-independent linear divergence $\Sigma_0^{\text{div}} = \frac{ig_0^2 m_{\text{R}}}{\pi^2} L_1$, where the divergent integral L_1 is defined according to

$$L_n = \int \mathrm{d}p\, p^{n-1} \ . \tag{2.13}$$

In the dicluster propagator (2.8) it can be seen that this momentum-independent divergence must be absorbed by the parameter Δ_0. Matching this to the elastic scattering t-matrix at an energy $E = \frac{k^2}{2m_{\mathrm{R}}}$,

$$iT_0(k) = -\frac{2\pi}{m_{\mathrm{R}}}\frac{1}{\cot\left(\delta_0(k)\right) - ik} \ , \tag{2.14}$$

we find the S-wave renormalization conditions

$$\frac{1}{a_0} = \frac{2\pi}{g_0^2 m_{\mathrm{R}}}\left(\Delta_0 + \Sigma_0^{\mathrm{div}}\right) \tag{2.15}$$

$$r_0 = -\frac{2\pi\nu_0}{g_0^2 m_{\mathrm{R}}^2} \ . \tag{2.16}$$

From the full dicluster propagator we can extract the LSZ-residue, or wavefunction renormalization $\mathcal{Z}_0$ for a bound state at energy $E = -B$. It is given by

$$\mathcal{Z}_0 = \left[\frac{\mathrm{d}\left(D_0(E)^{-1}\right)}{\mathrm{d}E}\right]^{-1}\Bigg|_{E=-B} \ , \tag{2.17}$$

and using the ERE parameters of Eqs. (2.15) and (2.16) we write this as

$$\mathcal{Z}_0 = \frac{2\pi\gamma_0}{m_{\mathrm{R}}^2 g_0^2}\frac{1}{1 - \gamma_0 r_0} \ . \tag{2.18}$$

We could rewrite this expression by replacing the g_0^2 in the denominator using Eq. (2.16) for the effective range. However, for many situations the denominator g_0^2 factor will cancel against another g_0^2 factor from the diagram that is being renormalized by the LSZ residue.

The renormalization procedure for the P-wave system is similar, but more invloved due to the additional powers of momentum from the P-wave interaction vertex. The bare P-wave dicluster propagator is given by

$$iD_1^{\mathrm{bare}}(E) = \frac{i}{\Delta_1 + \nu_1\left(E + i\varepsilon\right)} \tag{2.19}$$

and the full propagator can also be written as a geometrical series

$$iD_1(E) = \frac{i}{\Delta_1 + \nu_1\left(E + i\varepsilon\right) + \Sigma_1(E)} \ . \tag{2.20}$$

So far everything looks to be as straightforward as in the S-wave scenario. However, as we shall soon see, there are two independent divergences in the P-wave irreducible self-energy Σ_1. This fact complicates the renormalization. In momentum space we can write the self-energy as

$$\begin{aligned}
i\left(\Sigma_1(E)\right)_{ij} &= -g_1^2\int\frac{\mathrm{d}^4p}{(2\pi)^4}p_ip_j iS_{\mathrm{c}}(p_0, \mathbf{p})iS_{\mathrm{n}}(E - p_0, \mathbf{p}) \\
&= -ig_1^2\int\frac{\mathrm{d}^3p}{(2\pi)^3}p_ip_j S_{\mathrm{tot}}(E, \mathbf{p}) \ ,
\end{aligned} \tag{2.21}$$

where the p_0 residue integral was performed. The angular integration $\mathrm{d}\Omega$ kills all the off-diagonal elements of $p_i p_j$ and as such we write $\Sigma_1 = \frac{\delta_{ij}}{3} (\Sigma_1)_{ij}$. Therefore the resulting integral becomes

$$
\begin{aligned}
i\Sigma_1(E) &= -\frac{ig_1^2}{6\pi^2} \int \mathrm{d}p p^4 S_{\text{tot}}(E, \mathbf{p}) \\
&= \frac{ig_1^2 m_{\mathrm{R}}}{3\pi^2} \left(L_3 + 2m_{\mathrm{R}} E L_1 - \frac{i\pi}{2} (2m_{\mathrm{R}} E)^{3/2} \right) \ .
\end{aligned} \tag{2.22}
$$

It is now clear that two renormalizations are needed at LO for the P-wave interaction, since there are two independent divergences in the self-energy (2.22): one momentum independent and one at order momentum squared. Thus we can see that in the P-wave dicluster propagator (2.20) both the Δ_1 and the ν_1-terms are needed for proper renormalization. Comparing with the P-wave elastic scattering t-matrix

$$
T_1(k) = -\frac{6\pi}{m_{\mathrm{R}}} \frac{k^2}{\cot \delta_1(k) - ik^3} \ , \tag{2.23}
$$

we get the renormalization conditions

$$
\frac{1}{a_1} = \frac{6\pi}{m_{\mathrm{R}}} \left(\frac{\Delta_1}{g_1^2} + \frac{m_{\mathrm{R}} L_3}{3\pi^2} \right) \tag{2.24}
$$

$$
r_1 = -\frac{12\pi}{m_{\mathrm{R}}} \left(\frac{\nu_1}{2m_{\mathrm{R}} g_1^2} + \frac{m_{\mathrm{R}} L_1}{3\pi^2} \right) \ . \tag{2.25}
$$

Note in particular that both the Δ_1 and ν_1 terms are needed at LO in order to renormalize the P-wave interaction.

For the P-wave system the wavefunction renormalization can be written using the ERE-paramters from Eqs. (2.24) and (2.25) as

$$
\mathcal{Z}_1 = -\frac{6\pi}{m_{\mathrm{R}}^2 g_1^2} \frac{1}{r_1 + 3\gamma_1} \ . \tag{2.26}
$$

If we rewrite the expression (2.26) by replacing the denominator g_1^2 using the effective range expression (2.25), we arrive at

$$
\mathcal{Z}_1 = \frac{1}{r_1 + 3\gamma_1} \left(\frac{r_1}{\nu_1} - \frac{4}{\pi} L_1 \right) \ . \tag{2.27}
$$

The reason why we spell this equation out explicitly is since we can now see that the P-wave wavefunction renormalization has a divergent piece, coming from the L_1 divergent intergral. This will be important for the charge radius considerations in the next section.

2.1.3 The charge form factor

In this section we define the charge form factor and the charge radius for one-neutron halo systems. We write down the formula for the charge radius up to N³LO for the
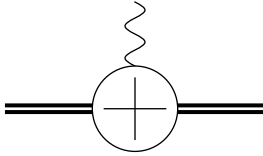
15

Figure 2.2: A sketch of the general charge form factor diagram. The diagram consists of an incoming and outgoing bound halo state, and a virtual photon leg. The crossed white blob corresponds to the nucleus-photon interaction and defines the charge form factor of the halo state.

S-wave one-neutron halo system and to NLO for the P-wave. We also point out that in the standard power counting the Cluster EFT results are predictive up to N^2LO for the S-wave and only at LO for the P-wave.

The charge form factor is given in terms of the zeroth component of the electromagnetic four-current J^μ, as

$$F_C(\mathbf{Q}) = \frac{1}{eZ_{\text{tot}}} \langle \mathbf{k}' | J_{\text{EM}}^0 | \mathbf{k} \rangle \ , \tag{2.28}$$

where $\mathbf{Q} = \mathbf{k}' - \mathbf{k}$ is the momentum transfer and Z_{tot} is the total charge number of the nucleus. Thus, the charge form factor can be calculated as the interaction of the bound state nucleus with a virtual photon in the Breit frame, with energy $\omega = 0$ and momentum $\mathbf{Q}$. The general form of such a diagram is shown in Fig. 2.2. The crossed blob represents all possible interactions with the external virtual photon leg. We measure this observable typically through elastic electron scattering on a nucleus. Of course, if the nucleus is just a point particle, then $J_{\text{EM}}^0 = Z_{\text{tot}}e$ and the charge form factor is simply $F_C(Q) = 1$. However, the atomic nucleus is an extended object, and as such there are momentum-dependent corrections. Such corrections enter with constants of proportionality given by the scale of the charge distribution. Therefore, we usually write the charge form factor in terms of the charge radius r_{ch}:

$$F_C(Q) = 1 - \frac{r_{\text{ch}}^2}{6} Q^2 + \ldots \tag{2.29}$$

The dots refer to terms of higher powers of the momentum. The functional form of the expression (2.29) can be obtained by considering the momentum expansion of the Fourier transform of the charge density. Experimentally the charge radius can be extracted from, for example, elastic electron scattering or from measurements of the atomic isotope shift. Theoretically, one typically calculates the point-proton radius and then adds the contribution from the size of the constituents in quadrature to arrive at the charge radius. Below we will present results for how different contributions to the charge radius appear naturally in Cluster EFT and we will discuss at what order these terms enter.

In Paper D the resulting charge radius formula for an S-wave one-neutron halo is given as

$$r_{\text{ch}}^2 = \frac{1}{1 - \gamma_0 r_0} \left(r_{\text{pt,LO}}^2 + \rho_c^2 + \frac{1}{Z_c} \rho_n^2 - \gamma_0 r_0 \rho_\sigma^2 \right) \ , \tag{2.30}$$

where the LO point-particle result was calculated in [16]:

$$r_{\mathrm{pt,LO}}^2 = \frac{f^2}{2\gamma_0^2} \ . \tag{2.31}$$

In Eq. (2.30) we assume that $r_{\mathrm{pt,LO}} \sim \gamma_0 \sim k_{\mathrm{lo}}$ and that $\rho_{\mathrm{c}} \sim \rho_\sigma \sim 1/r_0 \sim k_{\mathrm{hi}}$. For the purpose of simplicity, let us neglect the neutron finite-size contribution $\rho_{\mathrm{n}}^2/Z_{\mathrm{c}}$. As such, expanding in $k_{\mathrm{lo}}/k_{\mathrm{hi}}$ we arrive at

$$r_{\mathrm{ch}}^2 = \underbrace{r_{\mathrm{pt,LO}}^2}_{\mathrm{LO}} + \underbrace{\gamma_0 r_0 r_{\mathrm{pt,LO}}^2}_{\mathrm{NLO}} + \underbrace{(\gamma_0 r_0)^2 r_{\mathrm{pt,LO}}^2 + \rho_{\mathrm{c}}^2}_{\mathrm{N^2LO}} + \underbrace{\gamma_0 r_0 \left(\rho_{\mathrm{c}}^2 - \rho_\sigma^2\right) + \dots}_{\mathrm{N^3LO}} + \dots \ . \tag{2.32}$$

In the formula (2.32) it can be seen that the finite-size of the constituent core enters at $\mathrm{N^2LO}$ and that an undetermined short-range parameter, ρ_σ, appears at $\mathrm{N^3LO}$ in the standard power counting. Thus, the theory is unpredictive at $\mathrm{N^3LO}$. Note also that corrections due to the shape parameter enter at $\mathrm{N^3LO}$, but these are of no consequence for the charge radius since it is unpredictive at that order anyway. In Ref. [16] the authors denote $r_{\mathrm{pt,LO}}^2/(1 - \gamma_0 r_0)$ as NLO instead, but they give this result relative to the charge radius of the core. This means that they view their NLO result as the difference $r_{\mathrm{ch}}^2 - \rho_{\mathrm{c}}^2$. Note that the actual numerical contributions at each order is strange, since the $\mathrm{N^2LO}$ finite-size contribution is much larger than the LO result. We will come back to this oddity in the next section on heavy-core power counting.

For the P-wave system the charge-radius formula, with explicit terms up to NLO, is

$$r_{\mathrm{ch}}^2 = \underbrace{r_{\mathrm{pt}}^2}_{\mathrm{LO}} + \underbrace{\tilde{\rho}_\pi^2}_{\mathrm{NLO}} + \dots \ , \tag{2.33}$$

where the point-particle result was derived in [16] as

$$r_{\mathrm{pt}}^2 = -\frac{5f^2}{2\gamma_1(3\gamma_1 + r_1)} \tag{2.34}$$

and where we have defined

$$\tilde{\rho}_\pi^2 = -\nu_1 \mathcal{Z}_1 \rho_\pi^2 \ . \tag{2.35}$$

The parameter $\tilde{\rho}_\pi^2$ is allowed to take both positive and negative values. Note that the wavefunction renormalization $\mathcal{Z}_1$ contains a divergent piece, which can be seen in Eq. (2.27). This divergence is absorbed by the parameter ρ_π^2. The resulting $\tilde{\rho}_\pi^2$ parameter is finite. The fact that the short-range ρ_π^2 operator appears before the contribution due to the finite extent of the constituents is troublesome. It results in the somewhat non-expected fact that the charge radii of the constituents are irrelevant for Cluster EFT charge-radius calculations of P-wave halo states. This is in contradiction to previous charge radius considerations in EFT, for example the result of [16], where the charge radius of the constituent $^{10}\mathrm{Be}$ core is added in quadrature to the point-particle charge radius result of the P-wave halo state $^{11}\mathrm{Be}(1/2^-)$.

Let us consider what would happen if we were to include the finite-size contributions of the constituent core, but without the presence of the short-range ρ_π^2 operator. This

finite size contribution enters through the $\rho_{\rm c}^2$ operator in the Lagrangian part (2.6), via a loop-diagram where the photon is attached to the core field. This diagram is basically the same as the one that generated the $r_{\rm pt}^2$ contribution, but with the photon-core interaction replaced according to $ieZ_{\rm c} \mapsto -i\frac{eZ_{\rm c}\rho_{\rm c}^2}{6}Q^2$. Note, however, that the point-particle result $r_{\rm pt}^2$ comes from the second-order term of a Q-expansion of an exponential function in the integrand of this loop-diagram, while the core-contribution is already at order Q^2. This means that the charge radius of the core enters the resulting charge form factor of the P-wave halo state as

$$-\frac{\Gamma_{\rm loop}^{(0)}}{eZ_{\rm c}}\frac{\rho_{\rm c}^2}{6}Q^2 \ . \tag{2.36}$$

The $\Gamma_{\rm loop}^{(0)}$ is the zeroth-order part of the charge form factor loop-diagram, which is divergent. It can be written as

$$\Gamma_{\rm loop}^{(0)} = \frac{eZ_{\rm c}}{r_1 + 3\gamma_1}\left(3\gamma_1 + \frac{4\nu_1}{\pi}L_1\right) \ , \tag{2.37}$$

where the divergent L_1-part is explicit. Since the parameter $\rho_{\rm c}^2$ is an observable (it has been fixed to the charge radius of the core), this means that the core contribution comes with a divergence that can not be absorbed. As such, it is not possible to add the core contribution unless also the ρ_π^2-operator is present, since the parameter ρ_π^2 is a free parameter that can absorb the divergence.

2.2 Heavy-core systems

For two-body systems where one of the particles is much heavier than the other, certain kinematical suppressions exist. These suppressions only appear for some specific contributions to observables. For a one-neutron halo, the core mass, $M \sim A_{\rm c}m$, can be much heavier than the neutron mass. For example $A_{\rm c} = 10 \gg 1$ for ^{11}Be. This results in a suppression of the point-particle result for the charge radius of the halo state, as can be seen in Eq. (2.31), since $f = 1/(A_{\rm c} + 1)$. Actually, for ^{11}Be this suppression is of the order 100, which motivates us to modify the power counting for systems where the core is heavy.

In the heavy-core power counting we do not only count powers of momenta, but also factors of the core mass number, $A_{\rm c}$, (or the mass factor f if that is more appropriate). As an example, at LO in the heavy-core power counting the core propagator would be static, that is

$$S_{\rm c}(E, \mathbf{p}) = \frac{1}{E - \frac{\mathbf{p}^2}{2A_{\rm c}m} + i\varepsilon} \to S_{\rm c}^{\rm LO} = \frac{1}{E + i\varepsilon} \ , \tag{2.38}$$

as the $1/A_{\rm c}$ term would be considered higher order.

2.2.1 Heavy-core power counting

In the heavy-core power counting, which is outlined in Paper D, we want to both count powers of momentum, $k_{\rm lo}/k_{\rm hi}$, and the large-$A_{\rm c}$ suppression. As such we will match these

two expansion parameters according to

$$k_{\mathrm{lo}}/k_{\mathrm{hi}} \sim 1/A_{\mathrm{c}}^x \ , \tag{2.39}$$

with $x > 0$. The choice of x depends on what system is under consideration. For example, for a system with $A_{\mathrm{c}} = 10$ and $k_{\mathrm{lo}}/k_{\mathrm{hi}} \sim 0.4$ we find that $x = 2/5$ is appropriate.

If we go back to Eqs. (2.30) and (2.32), but assign powers of both $k_{\mathrm{lo}}/k_{\mathrm{hi}}$ and $1/A_{\mathrm{c}}$ to the terms, we find the following:

$$r_{\mathrm{ch}}^2 = \underbrace{r_{\mathrm{pt,LO}}^2}_{1/(k_{\mathrm{lo}}^2 A_{\mathrm{c}}^2)} + \underbrace{\gamma_0 r_0 r_{\mathrm{pt,LO}}^2}_{1/(k_{\mathrm{lo}} k_{\mathrm{hi}} A_{\mathrm{c}}^2)} + \underbrace{(\gamma_0 r_0)^2 r_{\mathrm{pt,LO}}^2}_{1/(k_{\mathrm{hi}}^2 A_{\mathrm{c}}^2)} + \underbrace{\rho_{\mathrm{c}}^2}_{1/k_{\mathrm{hi}}^2} + \underbrace{\gamma_0 r_0 \left(\rho_{\mathrm{c}}^2 - \rho_{\sigma}^2 \right)}_{k_{\mathrm{lo}}/k_{\mathrm{hi}}^3} + \ldots \tag{2.40}$$

Thus, in the heavy-core power counting it is clear from Eq. (2.40) that if A_{c} is sufficiently large, then the point-particle contribution is actually sub-leading. If $k_{\mathrm{lo}}/k_{\mathrm{hi}} \sim 1/A_{\mathrm{c}}$, then the point-particle contribution, $r_{\mathrm{pt,LO}}^2$, and the finite-size contribution, ρ_{c}^2, are both at LO. As an example, we can analyze the case of $^{11}\mathrm{Be}(1/2^+)$, where we argued that $x = 2/5$ is a good choice. Then, we organize the terms as

$$r_{\mathrm{ch}}^2 = \underbrace{\rho_{\mathrm{c}}^2}_{1/k_{\mathrm{hi}}^2} + \underbrace{\gamma_0 r_0 \left(\rho_{\mathrm{c}}^2 - \rho_{\sigma}^2 \right)}_{(k_{\mathrm{lo}}/k_{\mathrm{hi}})/k_{\mathrm{hi}}^2} + \underbrace{(\gamma_0 r_0)^2 \left(\rho_{\mathrm{c}}^2 - \rho_{\sigma}^2 \right)}_{(k_{\mathrm{lo}}/k_{\mathrm{hi}})^2/k_{\mathrm{hi}}^2} + \underbrace{r_{\mathrm{pt,LO}}^2 + \ldots}_{(k_{\mathrm{lo}}/k_{\mathrm{hi}})^3/k_{\mathrm{hi}}^2} + \ldots \ . \tag{2.41}$$

In Eq. (2.41), note that the point-particle contribution does not enter until $\mathrm{N}^3\mathrm{LO}$, since it scales three powers higher in $k_{\mathrm{lo}}/k_{\mathrm{hi}}$ than the first term. Instead the LO result is given by the finite-size contribution. Note also that already at NLO, given by the second term, we have a short-range contribution due to the ρ_{σ} parameter and as such the field theory for this system is only predictive at LO in the heavy-core power counting.

For P-waves the heavy-core power counting result for the charge radius is simply

$$r_{\mathrm{ch}}^2 = \underbrace{\tilde{\rho}_{\pi}^2}_{\mathrm{LO}} + \ldots \ , \tag{2.42}$$

that is an unknown parameter at LO. The point-particle contribution is proportional to f^2 and as such it is severly suppressed for a heavy core nucleus. Therefore Cluster EFT in the heavy-core power counting is unpredictive for charge radii of P-wave neutron halo states. This is of course a severe restriction of Cluster EFT applied to P-wave systems with a heavy core, but one should emphasize that there exist more observables than the charge radius and that these might be better behaved.

3 One-proton halos in effective field theory

In the previous chapter, we introduced Cluster EFT and we demonstrated details on the renormalization of S- and P-wave interactions. For neutron halos, the only interaction is through the strong force, and due to a fine-tuning this kind of system becomes very weakly bound. In this chapter we want to study one-proton halo nuclei using Cluster EFT and therefore we must also introduce the Coulomb interaction.

There has been some work on charged systems within EFT, starting with the efforts by Kong and Ravndal [23, 24, 25] and continuing with work on for example α-α scattering [20] in Cluster EFT and ^{3}He [26, 27] in Pionless EFT. Our work extends this list with one-proton halo nuclei.

For some nuclear systems the Coulomb interaction can be treated as rather weak, compared to the strong interaction. However, for proton halo systems this is not possible since the relevant low-momentum scale k_{lo} of the system is of the same size or smaller than the Coulomb momentum $k_C = Z_c \alpha m_R$, where $\alpha \approx 1/137$ is the fine-structure constant. What this means is that for proton halo nuclei the very small binding energy is a result of an interplay between the strong and the Coulomb interactions.

There are just a few one-proton halo candidates in the chart of nuclides, for example the $1/2^+$ excited state of ^{17}F, which consists mostly of a proton and an ^{16}O(0^+) core in a relative S-wave. This excited state of ^{17}F has a proton separation energy of only 0.1 MeV, while the $5/2^+$ ground state is bound by 0.6 MeV. Since the first excitation of the ^{16}O core is at $E_1 = 6$ MeV, ^{17}F should be a perfect system to apply Cluster EFT on. Actually, both the ground state and the excited state are well separated from the momentum scale of the core excitation, and therefore both states can be treated in Cluster EFT. In this work we have only included the excited state ^{17}F* into the field theory. We show results for the charge radius of ^{17}F* and the radiative capture process ^{16}O$(p, \gamma)^{17}$F* in Sec. 3.2. In order to also describe the ground state we would have to consider the D-wave nature of the interaction.

Other examples of proton halo nuclei in Nature are the ^{8}B one-proton halo nucleus, where a proton and a ^{7}Be core interact in a P-wave, and the two-proton halo ^{17}Ne. To be able to treat two-proton halo nuclei one would need to derive three-body Coulomb propagators, which is beyond the present reach of our formalism. We have considered the P-wave one-proton halo nucleus ^{8}B and we have calculated its charge radius and the S-factor for the radiative capture cross section ^{7}Be$(p, \gamma)^8$B. These results are presented in Chapter 3.3. We also present a correlation between the charge radius and the S-factor. This system has also been considered recently in Ref. [28].

3.1 Coulomb interactions

For low momenta the Coulomb interaction must be included to all orders and we do this by using the full Coulomb propagator G_C, shown in Fig. 3.1. The Coulomb propagator, or Coulomb Green's function, can be written in the spectral representation as

$$(\mathbf{r}|G_C(E)|\mathbf{r}') = \int \frac{d^3p}{(2\pi)^3} \frac{\psi_{\mathbf{p}}(\mathbf{r})\psi_{\mathbf{p}}^*(\mathbf{r}')}{E - \mathbf{p}^2/(2m_R) + i\varepsilon} , \tag{3.1}$$
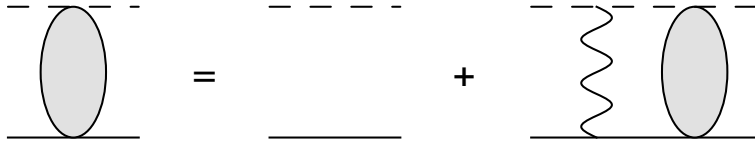
Figure 3.1: The Coulomb propagator, defined recursively. The shaded blob denotes the resummation of the Coulomb interaction.

where we have represented it in coordinate space, using round brackets. For momentum-space representations we will use angle brackets. We define the Coulomb wavefunction $\psi_{\mathbf{p}}(\mathbf{r})$ by its partial wave expansion

$$\psi_{\mathbf{p}}(\mathbf{r}) = \sum_{l=0}^{\infty} (2l+1) i^l \exp\left(i\sigma_l\right) \frac{F_l(\eta, \rho)}{\rho} P_l(\hat{\mathbf{p}} \cdot \hat{\mathbf{r}}) \ . \tag{3.2}$$

Here we have defined $\rho = pr$ and $\eta = k_{\mathrm{C}}/p$, with the Coulomb momentum $k_{\mathrm{C}} = Z_1 Z_2 \alpha m_{\mathrm{R}}$, where Z_1 and Z_2 are the proton number of the clusters. We also define the pure Coulomb phase shift $\sigma_l = \arg \Gamma(l+1+i\eta)$. The partial-wave projected Coulomb wavefunctions F_l and G_l can be expressed in terms of the Whittaker functions. The regular wavefunction F_l is written using the Whittaker M-function according to

$$F_l(\eta, \rho) = A_l(\eta) M_{i\eta, l+1/2}(2i\rho) \ , \tag{3.3}$$

with A_l defined as

$$A_l(\eta) = \frac{|\Gamma(l+1+i\eta)| \exp\left[-\pi\eta/2 - i(l+1)\pi/2\right]}{2(2l+1)!} \ . \tag{3.4}$$

The irregular Coulomb wave function, G_l, is given by

$$G_l(\eta, \rho) = i F_l(\eta, \rho) + B_l(\eta) W_{i\eta, l+1/2}(2i\rho) \ , \tag{3.5}$$

where W is the Whittaker W-function and the coefficient B_l is defined as

$$B_l(\eta) = \frac{\exp\left(\pi\eta/2 + il\pi/2\right)}{\arg \Gamma(l+1+i\eta)} \ . \tag{3.6}$$

Since we work with both bound-state and free Coulomb wavefunctions it is important to note that the absolute value and the argument of the Gamma-function are defined as

$$|\Gamma(l+1+i\eta)| = \sqrt{\Gamma(l+1+i\eta)\Gamma(l+1-i\eta)} \tag{3.7}$$

and

$$\arg \Gamma(l+1+i\eta) = \sqrt{\frac{\Gamma(l+1+i\eta)}{\Gamma(l+1-i\eta)}} \ . \tag{3.8}$$

The Gamow-Sommerfeld factor $C_\eta^2 = |\psi(0)|^2$ is given by

$$
\begin{aligned}
C_\eta^2 = C(0,\eta)^2 &= \frac{2\pi\eta}{\exp{(2\pi\eta)} - 1} \\
&= \exp{(-\pi\eta)}\Gamma(1 + i\eta)\Gamma(1 - i\eta)
\end{aligned} \tag{3.9}
$$

and we will also need its generalization to higher partial waves

$$
C(l,\eta)^2 = \exp{(-\pi\eta)}\Gamma(l + 1 + i\eta)\Gamma(l + 1 - i\eta) \ . \tag{3.10}
$$

Note in particular that

$$
C(1,\eta)^2 = (1 + \eta^2)C_\eta^2 \ . \tag{3.11}
$$

While the total phase shift is $\sigma_l + \delta_l$, the Coulomb-modified phase shift δ_l is what is usually referred to as the phase shift. The Coulomb-modified ERE defines the Coulomb-modified low-energy scattering parameters $a_l, r_l, \ldots$ through the phase shift:

$$
k^{2l+1}C(l,\eta)^2(\cot\delta_l - i) + 2k_{\rm C}h_l(\eta) = -\frac{1}{a_l} + \frac{1}{2}r_l k^2 + \ldots \ . \tag{3.12}
$$

The function h_l is given by

$$
h_l(\eta) = p^{2l}\frac{C(l,\eta)^2}{C(0,\eta)^2}\left(\psi(i\eta) + \frac{1}{2i\eta} - \log{(i\eta)}\right) \ , \tag{3.13}
$$

where ψ is the polygamma function.

3.1.1 Partial-wave projected Coulomb Green's function

We now continue by analyzing the Coulomb Green's function $(\mathbf{r}_1|G_{\rm C}|\mathbf{r}_2)$. It is useful to express the Green's function in its partial-wave expanded form

$$
(\mathbf{r}_1|G_{\rm C}(E)|\mathbf{r}_2) = \sum_{l=0}^{\infty}(2l+1)G_{\rm C}^{(l)}(E; r_1, r_2)P_l(\hat{\mathbf{r}}_1 \cdot \hat{\mathbf{r}}_2) \ . \tag{3.14}
$$

The form of $G_{\rm C}^{(l)}$ is derived by using the Coulomb wavefunctions (3.2), using spherical harmonics,

$$
\psi_{\mathbf{p}}(\mathbf{r}) = \sum_{l,m}4\pi i^l \exp{(i\sigma_l)}\frac{F_l(\eta,\rho)}{\rho}Y_{lm}^*(\theta,\phi)Y_{lm}(\theta,\phi) \ . \tag{3.15}
$$

23

We start from the spectral representation (3.1). In the first step we use the orthogonality of the harmonics and in the second step the addition theorem is used:

$$
\begin{aligned}
(\mathbf{r}_1|G_{\mathrm{C}}(E)|\mathbf{r}_2) &= \sum_{l_1 m_1}\sum_{l_2 m_2}\int\frac{\mathrm{d}^3 p}{(2\pi)^3}(4\pi)^2\frac{i^{l_1-l_2}\exp\left(i\sigma_{l_1}-i\sigma_{l_2}\right)\frac{F_{l_1}(\eta,\rho_1)}{\rho_1}\frac{F_{l_2}^{*}(\eta,\rho_2)}{\rho_2}}{E-\frac{\mathbf{p}^2}{2m_{\mathrm{R}}}} \\
&\quad\times Y_{l_1 m_1}(\theta_1,\varphi_1)Y_{l_1 m_1}^{*}(\theta_p,\varphi_p)Y_{l_2 m_2}(\theta_p,\varphi_p)Y_{l_2 m_2}^{*}(\theta_2,\varphi_2) \\
&= \sum_{lm}\int\frac{\mathrm{d}^3 p}{(2\pi)^3}4\pi\frac{F_l(\eta,\rho_1)F_l^{*}(\eta,\rho_2)}{\rho_1\rho_2}\frac{1}{E-\frac{\mathbf{p}^2}{2m_{\mathrm{R}}}} \\
&\quad\times Y_{lm}(\theta_1,\varphi_1)Y_{lm}^{*}(\theta_2,\varphi_2) \\
&= \sum_{l}(2l+1)P_l(\hat{\mathbf{r}}_1\cdot\hat{\mathbf{r}}_2)\int\frac{\mathrm{d}^3 p}{(2\pi)^3}\frac{F_l(\eta,\rho_1)F_l^{*}(\eta,\rho_2)}{\rho_1\rho_2}\frac{1}{E-\frac{\mathbf{p}^2}{2m_{\mathrm{R}}}} \quad (3.16)
\end{aligned}
$$

Thus, comparing Eqs. (3.14) and (3.16), the Green's function for a specific partial wave is given by

$$
G_{\mathrm{C}}^{(l)}(E;r_1,r_2) = \int\frac{\mathrm{d}^3 p}{(2\pi)^3}\frac{F_l(\eta,\rho_1)F_l^{*}(\eta,\rho_2)}{\rho_1\rho_2}\frac{1}{E-\frac{\mathbf{p}^2}{2m_{\mathrm{R}}}}\ . \quad (3.17)
$$

It is convenient to use the Coulomb Green's function in a non-integral form and below we present such a form for the bound-state Green's function. This can be done by doing a partial-wave projection and forming the Green's function as a product between two independent Coulomb wavefunctions, satisfying one boundary condition each, in accordance with the definition of Green's function. For the $r=0$ boundary condition we must use the regular Coulomb wave function F_l, while to satisfy the condition for a bound state at $r=\infty$ we need to form the combination

$$
iF_l + G_l\ . \quad (3.18)
$$

This can be seen from the $r\to\infty$ asymptotics

$$
F_l(\eta,\rho) \to \sin\left(\rho - l\pi/2 - \eta\log\left(2\rho\right) + \sigma_l\right) \quad (3.19)
$$

and

$$
G_l(\eta,\rho) \to \cos\left(\rho - l\pi/2 - \eta\log\left(2\rho\right) + \sigma_l\right), \quad (3.20)
$$

using that for a bound state $\rho = i\gamma r$, with $\gamma > 0$. The only combination that yields only an $\exp\left(-\gamma r\right)$ dependence is the combination given in (3.18). Therefore, the partial-wave projected Coulomb Green's function is

$$
G_{\mathrm{C}}^{(l)}(-B;\rho',\rho) = -\frac{m_{\mathrm{R}}p}{2\pi}\frac{F_l(\eta,\rho')\left[iF_l(\eta,\rho)+G_l(\eta,\rho)\right]}{\rho'\rho}\ . \quad (3.21)
$$

The normalization is given by the discontinuity of the slope at $\rho = \rho'$, according to

$$
\left.\left(\partial_{r'}-\partial_r\right)G_{\mathrm{C}}(E;pr',pr)\right|_{\rho'\to\rho} = \frac{1}{f(r)}\ , \quad (3.22)
$$

24

where $f(r) = 2\pi r^2/m_{\rm R}$ for the Schrödinger-Coulomb equation.

Many of the diagrams we consider will have a factor of a Coulomb Green's function with one end at zero separation. Using the identity

$$iF_l(\eta, \rho) + G_l(\eta, \rho) = \exp\left(i\sigma_l + \pi\eta/2 - li\pi/2\right)W_{-i\eta, l+1/2}(-2i\rho) \qquad (3.23)$$

and the limits

$$\lim_{\rho \to 0} \frac{F_0(\eta, \rho)}{\rho} = \exp\left(-\pi\eta/2\right)\sqrt{\Gamma(1+i\eta)\Gamma(1-i\eta)} \qquad (3.24)$$

and

$$\lim_{r \to 0} \left(\frac{F_1(\eta, \rho)}{\rho^2}\right) = \frac{1}{3}\exp\left(-\pi\eta/2\right)\sqrt{\Gamma(2+i\eta)\Gamma(2-i\eta)} \qquad (3.25)$$

we can write the relevant objects for propagation down to zero separation as

$$G_{\rm C}^{(0)}(-B; 0, \rho) = -\frac{m_{\rm R}p}{2\pi}\Gamma(1+i\eta)\frac{W_{-i\eta, 1/2}(-2i\rho)}{\rho} \qquad (3.26)$$

for S-wave interactions and

$$\lim_{\rho' \to 0} \left(\frac{G_{\rm C}^{(1)}(E; r', r)}{\rho'}\right) = i\frac{m_{\rm R}p}{6\pi}\Gamma(2+i\eta)\frac{W_{-i\eta, 3/2}(-2i\rho)}{\rho} \qquad (3.27)$$

for P-wave interactions. These results, Eqs. (3.26) and (3.27), are used when we evaluate the proton halo loop-integrals in this chapter numerically.

3.2   S-wave one-proton halo nuclei – The $^{17}{\rm F}^*$ state

In this section we present Cluster EFT formalism for calculating the charge radius and the radiative capture cross section for a one-proton halo nucleus, bound by an S-wave interaction between the core and the proton fields. We exemplify this formalism by showing results for the one-proton halo state $^{17}{\rm F}^*$. This section is based on the work presented in Papers A and C.

3.2.1   Interactions

Using Cluster EFT we treat the one-proton halo state $^{17}{\rm F}^*(1/2^+)$ as consisting of a proton and an $^{16}{\rm O}(0^+)$ core in a relative S-wave. The proton and the $^{16}{\rm O}$ core are therefore the effective degrees of freedom of the field theory.

Since the core is a 0^+ particle there is only one S-wave channel, namely $J = 1/2^+$, and thus the LO interaction is given by a single Dirac delta, $\delta(\mathbf{r})$. Higher-order interactions between the constituents come in as higher and higher powers of derivatives of the Dirac-delta, that is $\nabla^2\delta(\mathbf{r})$ and so on. By matching these interactions to low-energy scattering parameters of the S-wave Coulomb-modified ERE

$$kC_\eta^2(\cot\delta_0 - i) + 2k_{\rm C}h_0(\eta) = -\frac{1}{a_0} + \frac{1}{2}r_0k^2 + Pk^4 + \dots , \qquad (3.28)$$

one finds that the Dirac delta interaction $\delta(\mathbf{r})$ gives the scattering length a_0 and the derivative interaction $\nabla^2\delta(\mathbf{r})$ enters with the effective range r_0, as is shown in Sec. 2 in Paper C. In Eq. (3.28) the Gamow-Sommerfeld factor $C_\eta^2 = 2\pi\eta/(\exp{(2\pi\eta)} - 1)$ and the function $h_0(\eta) = \psi(i\eta) + \frac{1}{2i\eta} - \log{(i\eta)}$ are needed. Since each derivative scales as the low-momentum scale k_{lo}, the $\nabla^2\delta(\mathbf{r})$ interaction should be suppressed by two orders compared to the LO $\delta(\mathbf{r})$ interaction. However, for weakly bound systems such as halo nuclei, the scattering length is unnaturally large compared to the natural scaling k_{hi}. This implies that the $\nabla^2\delta(\mathbf{r})$ interaction is actually at NLO, as one can see from the Coulomb-modified ERE Eq. (3.28), using that $1/a_0 \sim k_{\mathrm{lo}}$, $r_0 \sim 1/k_{\mathrm{hi}}$ and $k \sim k_{\mathrm{lo}}$. The next interaction term $\nabla^4\delta(\mathbf{r})$ enters at N³LO, assuming that the shape parameter scales naturally as $P \sim 1/k_{\mathrm{hi}}^3$.

We will now treat the S-wave interaction using an auxiliary dicluster field in the Lagrangian. The Lagrangian for a spin-0 core and a proton, interacting only in the S-wave, using the dicluster field is given by

$$\mathcal{L} = \mathrm{p}_\sigma^\dagger\left(iD_t + \frac{\mathbf{D}^2}{2m}\right)\mathrm{p}_\sigma + \mathrm{c}^\dagger\left(iD_t + \frac{\mathbf{D}^2}{2M}\right)\mathrm{c} + \mathrm{d}_\sigma^\dagger\left[\Delta + \nu\left(iD_t + \frac{\mathbf{D}^2}{2M_{\mathrm{tot}}}\right)\right]\mathrm{d}_\sigma$$
$$- g\left[\mathrm{d}_\sigma^\dagger\mathrm{c}\mathrm{p}_\sigma + \mathrm{h.c.}\right] . \tag{3.29}$$

Here p_σ, with the spin index $\sigma = \pm 1/2$ denotes the spin-1/2 proton field with mass m and c the 0^+ core field with mass M. The covariant derivatives are defined as $D_\mu = \partial_\mu + ie\hat{Q}A_\mu$, with $\hat{Q}\mathrm{p}_\sigma = \mathrm{p}_\sigma$, $\hat{Q}\mathrm{c} = Z_c\mathrm{c}$ and $\hat{Q}\mathrm{d}_\sigma = (Z_c + 1)\mathrm{d}_\sigma$, where Z_c is the proton number of the core. The operator $\hat{Q}$ is simply the charge operator. The dicluster field d_σ has mass M_{tot} and the vertex, where the dicluster field breaks up into a proton and a core, has strength g. The parameter Δ is needed for renormalization of the S-wave interaction. The energy signature $\nu = \pm 1$ of the kinetic term of the dicluster field is present to allow for the possibility of a positive effective range, since we use the convention where the coupling g is real.

From the Lagrangian (3.29) we extract the Feynman rules for the propagators and the interactions. Firstly, the proton, core and the bare dicluster propagators are given by the inverse of the kinetic terms in Eq. (3.29). This gives the proton propagator

$$iS_{\mathrm{p}}(E, \mathbf{p}) = \frac{i}{E - \frac{\mathbf{p}^2}{2m} + i\varepsilon} , \tag{3.30}$$

the core propagator

$$iS_{\mathrm{c}}(E, \mathbf{p}) = \frac{i}{E - \frac{\mathbf{p}^2}{2M} + i\varepsilon} \tag{3.31}$$

and the bare dicluster propagator

$$iD^{(0)}(E, \mathbf{p}) = \frac{i}{\Delta + \nu\left(E - \frac{\mathbf{p}^2}{2M_{\mathrm{tot}}} + i\varepsilon\right)} . \tag{3.32}$$

This dicluster propagator is called bare, since it will be dressed by proton-core loops and thereby gain an additional energy dependence in the denominator.

There is only one contact interaction vertex, which is given by the $d_\sigma^\dagger c p_\sigma$ term, and its coefficient is $-g$. The Feynman rule for this vertex is given by

$$- ig \ . \tag{3.33}$$

In addition we have three vertices, where an A_0 photon interacts with the matter fields, which happens through the $iD_t = i\partial_t - e\hat{Q}A_0$, or νiD_t, operators. Thus we have the Feynman rules for the A_0 photon interaction with the proton

$$- ie \ , \tag{3.34}$$

the core

$$- ieZ_c \tag{3.35}$$

and the dicluster

$$- i\nu e(Z_c + 1) \ . \tag{3.36}$$

The dicluster-photon interaction can be thought of as a two-body current. Finally, we also have the vertices where a vector photon A_i couples to either of the matter fields. The responsible operators are $\frac{\mathbf{D}^2}{2m}$, $\frac{\mathbf{D}^2}{2M}$ and $\nu\frac{\mathbf{D}^2}{2M_{\text{tot}}}$, for interactions with the proton, core and dicluster, respectively. We chose to work in the Coulomb gauge, where $\nabla_i A_i = 0$, and therefore the $\mathbf{D}^2$ operator is expanded as $\mathbf{D}^2 = \nabla^2 + 2ie\hat{Q}A_i\nabla_i - e^2\hat{Q}^2 A_i A_i$. In this work we will only consider vertices with one photon field and therefore, using $\nabla = i\mathbf{p}$, we arrive at the Feynman rules for the A_i photon interaction with the proton

$$- i\frac{ep_p^i}{m} \ , \tag{3.37}$$

the core

$$- i\frac{eZ_c p_c^i}{M} \ , \tag{3.38}$$

and the dicluster

$$- i\frac{e(Z_c + 1)p_{\text{di}}^i}{M_{\text{tot}}} \ . \tag{3.39}$$

The momenta $\mathbf{p}_p$, $\mathbf{p}_c$ and $\mathbf{p}_{\text{di}}$ are the momenta of the proton, core and dicluster, respectively. Defining the relative momentum

$$\mathbf{p} = \frac{M\mathbf{p}_p - m\mathbf{p}_c}{M_{\text{tot}}} \tag{3.40}$$

and positioning us in the center-of-mass (c.m.) frame, where $\mathbf{p}_p = -\mathbf{p}_c$, we have $\mathbf{p}_p = \mathbf{p} = -\mathbf{p}_c$. Note that for a single dicluster field in the c.m. frame we have $\mathbf{p}_{\text{di}} = 0$, which means that the Feynman rule (3.39) is identically zero. For the Feynman rules with the vector photon A_i it is important to note that there are photon polarization vectors ϵ_1 and ϵ_2 needed also, which we will eventually multiply with the amplitudes.

The full dicluster propagator is defined in Fig. 3.2. In the c.m. frame it is constructed from the bare dicluster propagator $iD^{(0)}(E, 0)$, Eq. (3.32), as the geometrical series

$$\begin{aligned} iD(E) &= iD^{(0)}(E, 0) + iD^{(0)}(E, 0)i\Sigma(E)iD^{(0)}(E, 0) + \dots \\ &= \frac{i}{\Delta + \nu(E + i\varepsilon) + \Sigma(E)} \ , \end{aligned} \tag{3.41}$$
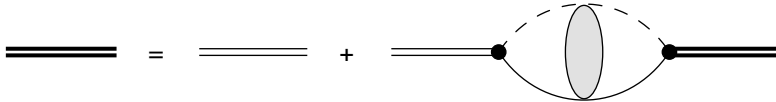
Figure 3.2: The full one-proton halo propagator, defined recursively using the bare halo propagator and the irreducible self-energy.
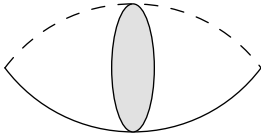

Figure 3.3: The irreducible self-energy diagram for the proton-core pair.

where we have also introduced the irreducible self-energy Σ. The irreducible self-energy is the bubble-diagram shown in Fig. 3.3, and it is simply given by $(-ig)^2$, from the Feynman rule (3.33), times the Coulomb propagator $(0|G_C(E)|0)$:

$$\Sigma(E) = -g^2 \int \frac{\mathrm{d}^3 p}{(2\pi)^3} \frac{\psi_{\mathbf{p}}(0)\psi_{\mathbf{p}}^*(0)}{E - \mathbf{p}^2/(2m_R) + i\varepsilon} \ . \tag{3.42}$$

The integral (3.42) is evaluated to[1]

$$\Sigma(E) = g^2 \frac{k_C m_R}{\pi} h_0(\eta) + \Sigma^{\mathrm{div}} \ . \tag{3.43}$$

Note that the irreducible self-energy is formally infinite, with a divergent part Σ^{div} that is independent of the energy. This is analogous to the renormalization procedure in Chapter 2. The matching to low-energy elastic scattering parameters and the renormalization is given in Sec. 2 of Paper C.

Whenever a bound state observable is to be calculated one needs to include the wavefunction renormalization $\mathcal{Z}$, such as to normalize the bound-state fields properly. An easy example of such a wavefunction renormalization is for an uncharged S-wave two-body system, with radial bound-state wavefunction $u_0(r) = \exp(-\gamma r)$. The proper normalization is off by a factor of $\sqrt{2\gamma}$, which can be seen by evaluating the integral $\int_0^\infty \mathrm{d}r |u_0(r)|^2$. The wavefunction renormalization for the bound state is given by

$$\mathcal{Z} = \frac{1}{\nu + \Sigma'(-B)} \tag{3.44}$$

and in terms of the effective range it can be written as

$$\mathcal{Z} = \frac{6\pi k_C}{g^2 m_R^2} \left[-3k_C r_0 + \frac{6k_C^2}{m_R} \frac{\mathrm{d}}{\mathrm{d}E} h_0(\eta) \right]^{-1} \Bigg|_{E=-B} \ . \tag{3.45}$$

---

[1]See Ref. [24] for details on the integration.

Note that for small values of $\gamma/k_{\rm C}$, the second term in the denominator of Eq. (3.45) can be expanded as $1 + \mathcal{O}(\gamma^2/k_{\rm C}^2)$. It is instructive to compare the $k_{\rm C} \gg \gamma$ limit

$$\mathcal{Z} = \frac{6\pi k_{\rm C}}{g^2 m_{\rm R}^2} \frac{1}{1 - 3k_{\rm C}r_0} + \mathcal{O}\left(\frac{\gamma^2}{k_{\rm C}^2}\right) \tag{3.46}$$

with the wavefunction renormalization for a one-neutron halo [16]

$$\mathcal{Z}^{\text{neutron halo}} = \frac{2\pi\gamma}{g^2 m_{\rm R}^2} \frac{1}{1 - \gamma r_0} \ . \tag{3.47}$$

While the universal low-energy physics for a one-neutron halo is defined by the momentum scale γ, it seems as though the low-energy physics for a one-proton halo, in the limit where $k_{\rm C} \gg \gamma$, is given in terms of a scale $3k_{\rm C}$. One can now ask whether such a limit is realized anywhere in Nature. We will consider the ^{17}F* one-proton halo nucleus for which we have $\gamma/k_{\rm C} = 0.265$, that is actually small enough for the limit to be qualitatively realized. The consequences for ^{17}F* are discussed in Sec. 5 of Paper C. One result is that the separation of scales for the proton-core interaction is reduced to $k_{\rm C}/k_{\rm hi}$, which can be handled by fixing the wavefunction renormalization by the use of the ANC. The relation to the ANC, A, is given by

$$\mathcal{Z} = \frac{\pi}{g^2 m_{\rm R}^2 \Gamma(1 + k_{\rm C}/\gamma)^2} A^2 \ . \tag{3.48}$$

If we compare the expression (3.48) with Eq. (3.46) we note that these are basically two different parameterizations of the LSZ residue: one in terms of the ERE parameters and one in terms of the ANC. Both parameterizations are of course valid, but for some cases one of them might be preferable to the other.

For ^{17}F* we note that there is a fine tuning in the effective range such that the denominator in Eq. (3.45) is very close to zero, that is the wavefunction renormalization $\mathcal{Z}$ is extremely large. The large value for $\mathcal{Z}$ can be seen from the fact that the ANC for ^{17}F* is very large (on the order of 80 fm$^{-1/2}$ [29, 30]). This means that all observables that involves the bound state, for example the charge radius and the radiative capture cross section, are enhanced by a large factor $\mathcal{Z}$. However, due to the large value of the Coulomb momentum for this system, $k_{\rm C} = 51.2$ MeV, the Cluster EFT prediction for the ^{17}F* charge radius is at a rather expected value anyway, as we will see in Section 3.2.4.

3.2.2 The charge form factor

We now turn to the calculation of the observable charge form factor, or more specifically the charge radius. Including effective-range corrections there are two charge form factor diagrams for an S-wave interaction, and these are shown in Fig. 3.4. In the following parts of this section we construct these amplitudes and show how they give the charge form factor of the system.

Charge form factor diagrams

The loop-diagram in Fig. 3.4(b), $\Gamma_{\rm loop}(Q)$, consists of a proton-core bubble, where the external photon line couples to either the core or the proton, with Feynman rules given by
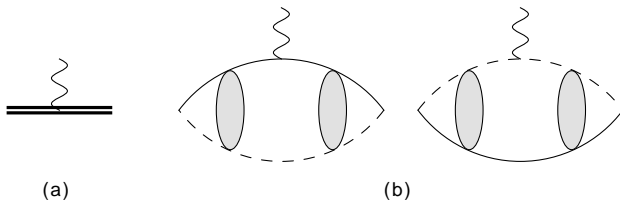
Figure 3.4: The charge form factor diagrams. (a) The tree-level diagram Γ_{tree}, where the virtual photon couples to the halo field, and (b) the loop-diagram $\Gamma_{\text{loop}}(Q)$, where the photon couples to the core and the proton fields, respectively. The loop-diagram depends on the momentum transfer Q, while the tree-level diagram only gives a constant contribution to the charge form factor.

Eqs. (3.35) and (3.34), respectively. The shaded blobs denote the Coulomb resummation and they are simply given by two-body Coulomb propagators $\langle \mathbf{p}'|G_{\text{C}}(-B)|\mathbf{p}\rangle$, where the angle brackets are used for momentum space. In total, therefore, we have one interaction vertex between an A_0 photon and either a core or a proton, two contact interaction vertices with Feynman rule given in Eq. (3.33), two Coulomb propagators and three momentum loops to be integrated over. In momentum space the loop-diagram is therefore given by

$$
\begin{aligned}
\Gamma_{\text{loop}}(Q) =& g^2 e Z_{\text{c}} \int \frac{\mathrm{d}^3 p_1}{(2\pi)^3} \frac{\mathrm{d}^3 p_2}{(2\pi)^3} \frac{\mathrm{d}^3 p_3}{(2\pi)^3} \langle \mathbf{p}_1|G_{\text{C}}(-B)|\mathbf{p}_2 + f\mathbf{Q}/2\rangle \\
&\times \langle \mathbf{p}_2 - f\mathbf{Q}/2|G_{\text{C}}(-B)|\mathbf{p}_3\rangle \\
&+ [(f \to 1-f) , (Z_{\text{c}} \to 1)] .
\end{aligned}
\tag{3.49}
$$

Note that in using the two-body Coulomb propagators we have already performed the energy residue integrals; the Coulomb propagators are at the bound state energy $E = -B$. The $[(f \to 1-f) , (Z_{\text{c}} \to 1)]$ term is due to the fact that the photon can interact with both the core and the proton. The mass ratio $f = m/M_{\text{tot}}$ defines the differences in kinematics for the proton and the core. The momentum dependencies in the Coulomb propagators are relative momenta of the proton and the core. For example, in the loop where the photon is attached to the core we define the proton momentum as $\mathbf{p}_2$, while the core momentum is $-\mathbf{p}_2 - \mathbf{Q}/2$ before the photon interaction and $-\mathbf{p}_2 + \mathbf{Q}/2$ after. This gives the relative momenta $\mathbf{p}_2 + f\mathbf{Q}/2$ and $\mathbf{p}_2 - f\mathbf{Q}/2$, respectively, using the defining equation (3.40).

Performing a Fourier transform on each of the momentum-space kets and bras, we arrive at the much simpler coordinate-space integral

$$
\begin{aligned}
\Gamma_{\text{loop}}(Q) &= g^2 e Z_{\text{c}} \int \mathrm{d}^3 r (0|G_{\text{C}}(-B)|\mathbf{r}) \exp\left(if\mathbf{Q}\cdot\mathbf{r}\right)(\mathbf{r}|G_{\text{C}}(-B)|0) \\
&\quad + [(f \to 1-f) , (Z_{\text{c}} \to 1)] ,
\end{aligned}
\tag{3.50}
$$

where the coordinate space Coulomb propagators must be purely S-wave since they have

one end at zero separation. Using Eq. (3.26) we write these propagators as

$$|(0|G_{\rm C}(-B)|\mathbf{r})|^2 = \frac{m_{\rm R}^2}{(2\pi)^2}\Gamma(1 + k_{\rm C}/\gamma)^2\frac{W_{-k_{\rm C}/\gamma,1/2}(2\gamma r)^2}{r^2} \ , \tag{3.51}$$

where W is the Whittaker-W function. The integral (3.50) is now straightforward to evaluate numerically.

The finite-size corrections from the constituent core and proton can be added straightforwardly to the loop-diagram (3.50), as was discussed in Paper D. We simply make the substitution $\exp{(if\mathbf{Q}\cdot\mathbf{r})} \mapsto \exp{(if\mathbf{Q}\cdot\mathbf{r})}\left(1 - \frac{Z_{\rm X}\rho_{\rm X}^2 Q^2}{6Z_{\rm tot}}\right)$, where X is p (c) for the term where the photon couples to the proton (core). This full loop-diagram then includes both the point-particle and the finite-size contributions.

The tree-level diagram in Fig. 3.4(a), $\Gamma_{\rm tree}$, is from a two-body current operator, and it enters with an effective-range correction. The diagram is simply

$$\Gamma_{\rm tree} = \nu e(Z_{\rm c} + 1) \ , \tag{3.52}$$

which is a constant. Following Paper D, we can straightforwardly add the short-range contribution from the $d^\dagger(\nabla^2 A_0)d$ operator to the diagram (3.52). The full result then is

$$\Gamma_{\rm tree,full}(Q) = \nu e(Z_{\rm c} + 1)\left(1 - \frac{\rho_{\rm d}^2 Q^2}{6}\right) \ . \tag{3.53}$$

Summing the contributions from the diagrams, the full version of diagram (3.50) and (3.53), we can arrive at the observable $\langle\mathbf{k}'|J^0|\mathbf{k}\rangle$ in Eq. (2.28); we only need to normalize the diagrams properly first. This is done with one square root of the LSZ residue factor, Eq. (3.45), for each bound-state end of the diagrams in Fig. 3.4. The charge form factor is therefore given in terms of the diagrams Eqs. (3.50) and (3.52) and in total one power of the LSZ residue $\mathcal{Z}$ as

$$F_{\rm C}(Q) = \frac{\mathcal{Z}}{e(Z_{\rm c} + 1)}(\Gamma_{\rm loop,full}(Q) + \Gamma_{\rm tree,full}(Q) + \dots) \tag{3.54}$$

where the dots refer to higher-order diagrams that we do not consider here.

Normalization of the charge form factor

At zero momentum transfer ($Q = 0$) the charge form factor must be equal to one, as is evident from Eq. (2.29). In this section we show that this is indeed the case, using Eq. (3.54) for the charge form factor.

At $Q = 0$ Eq. (3.50) reduces to

$$\Gamma_{\rm loop}(0) = g^2 e(Z_{\rm c} + 1)\int {\rm d}^3 r(0|G_{\rm C}(-B)|\mathbf{r})(\mathbf{r}|G_{\rm C}(-B)|0) \ . \tag{3.55}$$

Using the spectral representation of the Coulomb Green's function

$$(0|G_{\rm C}(E)|\mathbf{r}) = \int\frac{{\rm d}^3 p}{(2\pi)^3}\frac{\psi_{\mathbf{p}}(0)\psi_{\mathbf{p}}^*(\mathbf{r})}{E - \mathbf{p}^2/(2m_{\rm R}) + i\varepsilon} \ , \tag{3.56}$$

31

and orthonormality of the Coulomb wave functions

$$\int \mathrm{d}^3 r \ \psi_{\mathbf{p}}^*(\mathbf{r})\psi_{\mathbf{p}'}(\mathbf{r}) = (2\pi)^3 \delta^{(3)}(\mathbf{p} - \mathbf{p}') \ , \tag{3.57}$$

Eq. (3.55) is simply

$$\begin{aligned}
\Gamma_{\mathrm{loop}}(0) =& g^2 e(Z_{\mathrm{c}} + 1) \int \frac{\mathrm{d}^3 p}{(2\pi)^3} \frac{\psi_{\mathbf{p}}(0)\psi_{\mathbf{p}}^*(0)}{(-B - \mathbf{p}^2/(2m_{\mathrm{R}}) + i\varepsilon)^2} \\
=& e(Z_{\mathrm{c}} + 1)\Sigma'(-B) \ ,
\end{aligned} \tag{3.58}$$

where we used Eq. (3.42) for the irreducible self-energy in the last step.

The form factor (3.54) at $Q = 0$ is now given by, using Eqs. (3.44), (3.52) and (3.58),

$$\begin{aligned}
F_{\mathrm{C}}(0) =& \frac{1}{\nu + \Sigma'(-B)} \frac{1}{e(Z_{\mathrm{c}} + 1)} \left(\Gamma_{\mathrm{tree}} + \Gamma_{\mathrm{loop}}(0) \right) \\
=& \frac{1}{\nu + \Sigma'(-B)} \left(\nu + \Sigma'(-B) \right) \\
=& 1 \ ,
\end{aligned} \tag{3.59}$$

which demonstrates proper normalization.

The charge radius

We have shown that the charge form factor is properly normalized and it is straightforward to show that the order Q term is identically zero, since it will integrate to zero in Eq. (3.50). In obtaining the charge radius, we can therefore focus completely on the order Q^2 term.

The charge radius r_{ch} is defined by the Q^2 coefficient of the charge form factor, according to Eq. (2.29), $F_{\mathrm{C}}(Q) = 1 - \frac{r_{\mathrm{ch}}^2}{6}Q^2 + \dots$. Therefore, using Eq. (3.54), the charge radius is given by

$$\begin{aligned}
r_{\mathrm{ch}}^2 =& -\frac{3}{e(Z_{\mathrm{c}} + 1)} \mathcal{Z}\Gamma''_{\mathrm{loop,full}}(0) \\
=& r_{\mathrm{pt}}^2 + \frac{1}{1 - 3k_{\mathrm{C}}r_0} \left(\frac{Z_{\mathrm{c}}}{Z_{\mathrm{c}} + 1}\rho_{\mathrm{c}}^2 + \frac{1}{Z_{\mathrm{c}} + 1}\rho_{\mathrm{p}}^2 - 3k_{\mathrm{C}}r_0\rho_{\mathrm{d}}^2 \right) \ ,
\end{aligned} \tag{3.60}$$

with

$$r_{\mathrm{pt}}^2 = -\frac{3}{e(Z_{\mathrm{c}} + 1)} \mathcal{Z}\Gamma''_{\mathrm{loop}}(0) \ . \tag{3.61}$$

The prime in Eq. (3.60) denotes a derivative with respect to the momentum Q. Thus, by evaluating the integral (3.50) numerically and inserting the result into Eq. (3.60) together with the charge radii of the constituents, the Cluster EFT charge radius result for a given system can in principle be obtained. However, the short-range contribution $3k_{\mathrm{C}}r_0\rho_{\mathrm{d}}^2$ enters already at N^{2}LO if $3k_{\mathrm{C}}r_0 \sim 1$, which is the case for $^{17}\mathrm{F}^*$. As such the Cluster EFT charge radius calculation for $^{17}\mathrm{F}^*$ is only predictive to NLO.
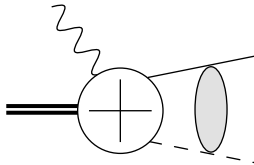
Figure 3.5: Sketch of the general radiative capture diagram. The diagram consists of an incoming proton-core pair, which is given by a Coulomb wave function, an outgoing bound halo state and an outgoing real photon. The crossed white blob indicates all the possible relevant interactions. The direction of time is from right to left.

3.2.3 Radiative capture and the astrophysical S-factor

Radiative nucleon capture is the capture of a nucleon on a core, while emitting a photon. There also exist radiative capture of clusters of nucleons, for example $^3\mathrm{He}(^4\mathrm{He}, \gamma)^7\mathrm{Be}$, and the formalism we present below can straightforwardly be extended to include these. When the captured nucleon is a proton, the cross section is exponentially suppressed at low energies, due to the repulsive Coulomb barrier; the proton must tunnel through this barrier. Therefore, this process is very difficult to measure experimentally. However, many of the important reactions in the nucleosynthesis are radiative capture processes of charged particles and therefore, if we wish to understand how the elements in Nature were created, we need to consider these processes.

The fact that these reactions are so hard to measure only makes them even more interesting from the viewpoint of a nuclear theorist. Accurate cross-section predictions is important input for the nucleosynthesis modeling. In the solar-fusion processes these reactions occur at energies around 10 keV. Therefore, the effort of pinning down the exact cross sections for radiative capture reactions is a joint venture between nuclear experiment and theory, where experiments can only measure accurately down to some hundred keV and theory can provide good models for extrapolation of the data down to threshold.

The conventional way of presenting radiative proton capture cross sections is through the astrophysical S-factor

$$S(E) = E \exp{(2\pi\eta)}\sigma_{\mathrm{tot}}(E) \ , \tag{3.62}$$

where E is the c.m. energy. The S-factor is defined in such a way that the exponential Coulomb repulsion has been removed, and as such the S-factor is a much more convenient object than the exponentially suppressed cross section $\sigma_{\mathrm{tot}}(E)$.

In Fig. 3.5 a sketch of a general capture diagram is shown. On the right side of the diagram is the incoming proton-core pair, which interacts to all orders via the Coulomb interaction. This incoming proton-core pair has a relative momentum $\mathbf{p}$ and energy $E = \mathbf{p}^2/(2m_\mathrm{R})$, and can be described by a Coulomb wavefunction $\psi_\mathbf{p}$. To the left are the outgoing halo field with momentum $-\mathbf{k}$, represented by the double-line, and the real photon with four momentum $(\omega, \mathbf{k})$, in the zero-momentum frame. Energy conservation implies that $\omega = -M_{\mathrm{tot}} + \sqrt{M_{\mathrm{tot}}^2 + 2M_{\mathrm{tot}}(E + B)}$, where B is the binding energy or one-proton separation energy. Considering energies much smaller than the total mass M_{tot} we find $\omega \approx B + E$. The crossed white blob denotes all the possible interactions
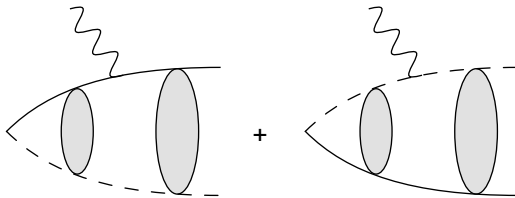
Figure 3.6: The LO radiative capture diagrams, where the incoming proton and core interact with a real vector photon. Since the formed halo bound state is due to an S-wave interaction, the incoming proton-core pair is in a relative P-wave, if only E1 capture is considered. The direction of time is from right to left.

that can take place in the process, and it is these interactions that can be organized in a power counting in the EFT.

In Sec. 4 of Paper C the radiative capture amplitude is derived up to N^{5}LO. The LO radiative capture diagrams is shown in Fig. 3.6. The resulting LO amplitude, is given by

$$\mathcal{A} = - ig\sqrt{\mathcal{Z}}\frac{eZ_\text{c}f}{m_\text{R}} \int \mathrm{d}^3r \ G_\text{C}^{(0)}(-B;0,\rho) \exp\left(-if\mathbf{k}\cdot\mathbf{r}\right)\nabla\psi_\mathbf{p}(\mathbf{r})$$
$$- \left[(f \to 1-f) \ , \ (Z_\text{c} \to 1)\right] \ . \tag{3.63}$$

One can understand Eq. (3.63) in terms of standard quantum mechanics. At the far right there is an incoming Coulomb wavefunction $\psi_\mathbf{p}(\mathbf{r})$. In the middle we have the vector current operator $\frac{eZ_\text{c}f}{m_\text{R}} \exp\left(-if\mathbf{k}\cdot\mathbf{r}\right)\nabla$, corresponding to the interaction between the core and the vector photon. And at the far left in the integrand is the bound state wavefunction $G_\text{C}^{(0)}(-B;0,\rho) \propto W_{-k_\text{C}/\gamma,1/2}(2\gamma r)/r$, given in Eq. (3.27). Due to the presence of one bound-state field, there is a wavefunction renormalization $\sqrt{\mathcal{Z}}$ present. Of course the photon can couple to both the core and the proton and hence the $-\left[(f \to 1-f) \ , \ (Z_\text{c} \to 1)\right]$ piece, where the minus sign can be traced back to the Feynman rule for the interaction with the vector photon.

At NLO there are no additional capture diagrams. One could imagine new diagrams where the vector photon couples through an operator $\nabla + ie\hat{Q}\mathbf{A}$, coming from the effective-range correction, but such a diagram can only appear if initial-wave (strong) scattering is included. In the field theory that we use, only the strong S-wave interaction is included, while the incoming proton-core wave must be a P-wave due to the fact that the E1 photon changes the angular momentum by one (remember that the final bound state is an S-wave). However, the proton-core interaction receives a correction from the effective-range. This correction appears in the LSZ-factor, as is given in Eq. (3.45) and it is the only correction at NLO.

The shape parameter enters at N^{3}LO, but it will also not add any new capture diagrams, since they can only appear through initial-wave (strong) scattering. And similarly as for the effective-range correction, the shape parameter enters as a correction in the LSZ-factor (this is true for all corrections to the proton-core interaction). Thus, if we use an ANC as input to constrain the parameters of the field theory, then the theory will be determined to N^{3}LO, since the ANC is proportional to the LSZ-factor according
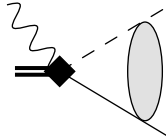
Figure 3.7: The N^{4}LO radiative capture diagram. The direction of time is from right to left.

to Eq. (3.48). As such, by fitting the interaction to an ANC the result is correct up to N^{3}LO.

At N^{4}LO a short-range operator enters. The interaction term is given in Paper C as [2]

$$\left[D_{3/2}^{(\mathrm{E1})} \mathcal{C}_{is}^{a} \mathcal{C}_{aj}^{s'} + D_{1/2}^{(\mathrm{E1})} \mathcal{C}_{is}^{\sigma} \mathcal{C}_{\sigma j}^{s'} \right] d_{s'}^{\dagger} \left(\partial_0 A_j - \nabla_j A_0 \right) \left(c \overset{\leftrightarrow}{\nabla}_i p_s \right) + \mathrm{h.c.} \ . \tag{3.64}$$

The coefficients $D_{3/2}^{(\mathrm{E1})}$ and $D_{1/2}^{(\mathrm{E1})}$ correspond to the two possible spin-channels in the incoming P-wave wavefunction. Note that the gauge-invariant operator $(\partial_0 A_j - \nabla_j A_0)$ is non-minimal. Counting dimensions of the operator we find that it scales as dimension 9, which is four orders above LO.

The contribution due to the N^{4}LO operator is through the diagram in Fig. 3.7, resulting in the amplitude

$$\mathcal{B} = D^{(\mathrm{E1})} \sqrt{\mathcal{Z}} \omega \exp\left(i\sigma_1\right) \mathbf{p} \sqrt{(1+\eta^2) C_\eta^2} \ . \tag{3.65}$$

In this amplitude we have, for simplicity, introduced the combined coefficient $D^{(\mathrm{E1})}$. Note that the photon energy-dependence comes from the ∂_0 and the last part comes from the P-wave integral $\int \frac{\mathrm{d}^3 k}{(2\pi)^3} \mathbf{k} \psi_{\mathbf{p}}(\mathbf{k})$ (see the appendix of Paper B). Note that the next operator that contributes to the radiative capture cross section appears at N^{6}LO, which is discussed in Paper C. As such this calculation is valid to N^{5}LO.

By multiplying the amplitude Eq. (3.63) with the photon polarization vectors ϵ_i (note that both $\mathcal{A}$ and ϵ_i are vector quantities) and squaring, we arrive at the differential cross section, Eq. (3.66)

$$\frac{\mathrm{d}\sigma}{\mathrm{d}\Omega} = \frac{m_{\mathrm{R}}\omega}{8\pi^2 p} \sum_i |\epsilon_i \cdot \mathcal{A}|^2 \ , \tag{3.66}$$

where in Coulomb gauge we have the Ward identity

$$\epsilon_i \cdot \mathbf{k} = 0 \ . \tag{3.67}$$

Once Eq. (3.63) has been multiplied with the photon polarization vectors the angular

---

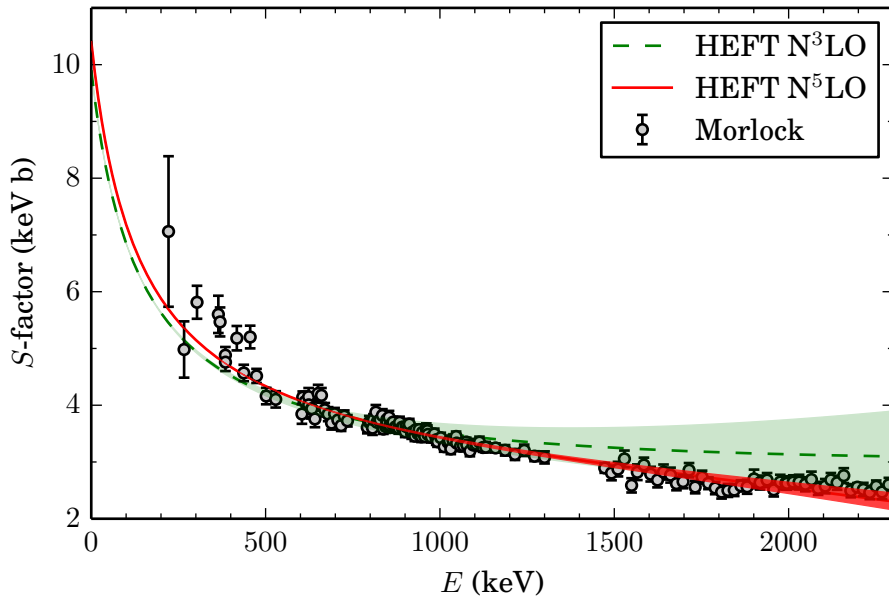[2]There is a typo in Paper C, where the subscript is written as 5/2 instead of 3/2.

Figure 3.8: The astrophysical S-factor for $^{16}O(p,\gamma)^{17}F^*$, plotted as a function of the c.m. energy E. The Cluster EFT results are fitted, at N³LO and N⁵LO, to the experimental data by Morlock *et al.* [31]. The Morlock data is shown without the uncertainty due to the absolute normalization. The error bands are given by the omission of higher-orders.

integrals are easily evaluated and we arrive at the integral

$$\sum_i |\epsilon_i \cdot \mathcal{A}|^2 = \left| \sqrt{\mathcal{Z}} \sin\theta(\cos\phi + \sin\phi) \frac{4\pi g e Z_c f \exp(i\sigma_1)}{m_R p} \right.$$
$$\times \int dr\, G_C^{(0)}(-B; 0, \rho) j_0(f\omega r) \frac{\partial}{\partial r} [r F_1(k_C/p, pr)]$$
$$\left. - [(f \to 1-f),\ (Z_c \to 1)] \right|^2, \tag{3.68}$$

which can be calculated numerically. The P-wave Coulomb wavefunction, F_1, was introduced in Sec. 3.1. Note that the result (3.68) depends on the angles ϕ and θ. These are the angles that are integrated over when going from the differential cross section (3.66) to the total cross section.

3.2.4   Results for the halo state $^{17}F^*$

In Paper C the radiative capture formalism is exemplified by calculating the astrophysical S-factor of $^{16}O(p,\gamma)^{17}F^*$. The S-factor is calculated at both N³LO, where the ANC is

the only non-trivial free parameter, and N^{5}LO, where the short-range operator (3.64) is included also. The resulting S-factor is shown in Fig. 3.8. The procedure in Paper C was to fit these free parameters to the experimentally measured S-factor, and thereby be able to both extract the ANC and the threshold S-factor. The fitted ANC could then be compared with previously extracted ones and it was also used as input for the charge radius calculation of the halo state ^{17}F*.

The obtained ANC is

$$A = \begin{cases} (77.4 \pm 0.2 \text{ (stat)} \pm 3.8 \text{ (norm)}) \text{ fm}^{-1/2} \text{ , N}^3\text{LO} \\ (79.3 \pm 0.2 \text{ (stat)} \pm 3.9 \text{ (norm)}) \text{ fm}^{-1/2} \text{ , N}^5\text{LO} \end{cases} , \qquad (3.69)$$

which can be compared to those of Huang $et\ al.$ $A = 77.21$ fm$^{-1/2}$ [29] and Gagliardi $et\ al.$ (80.6 ± 4.2) fm$^{-1/2}$ [30]. The resulting threshhold S-factor is

$$S = \begin{cases} (9.9 \pm 0.1 \text{ (stat)} \pm 1.0 \text{ (norm)}) \text{ keV b , N}^3\text{LO} \\ (10.4 \pm 0.1 \text{ (stat)} \pm 1.0 \text{ (norm)}) \text{ keV b , N}^5\text{LO} \end{cases} . \qquad (3.70)$$

The 1% error due to the EFT fit is mainly a statistical error, but it also includes the EFT error. The EFT error is given by $(p/k_{\text{hi}})^{n+1}$, where p is the incoming momentum and n is the order at which the calculation was performed. The 10% error is due to the uncertainty in the absolute normalization of the experimental data.

Using the extracted N^{5}LO ANC, the NLO charge radius result for ^{17}F* is

$$r_{\text{ch}} = (2.20 \pm 0.11 \text{ (ANC)}) \text{ fm} . \qquad (3.71)$$

Note that this charge radius result does not include the finite-size contributions from the core and proton charge radii, since these appear at the same order as the undetermined short-range operator. In Paper C an EFT error of 0.04 fm is given, as the charge radius has been calculated to NLO in the power counting and the expansion parameter is γ/k_{hi}. However, a more cautious error estimate could place the estimated EFT error much larger, due to the fine-tuning coming from the strong Coulomb repulsion $k_{\text{C}} \gg \gamma$. As is shown in Paper C, the charge radius actually scales with the Coulomb momentum in this regime and as such a pessimistic EFT expansion parameter (for the charge radius alone) might be $k_{\text{C}}/k_{\text{hi}} = 0.7$. This finding would actually result in an EFT error of 0.5 fm at this order.

It would be interesting to use low-energy elastic scattering data, in addition to the ANC fitting, to constrain the S-factor. However, since the effective range is very close to the pole position $r_0 \approx 1.2$ fm, it would have to be measured to the third (fourth) digit for the resulting S-factor error to be about 10% (1%). For such accuracies the shape parameter is needed, and possibly also higher-order terms in the ERE.

3.3 P-wave one-proton halo nuclei – The ^{8}B nucleus

In this section we present formalism and results for a one-proton halo nucleus bound by a P-wave interaction. The interaction being of P-wave nature implies that two parameters

are needed at LO to renormalize the theory. We show results for the charge radius of ^{8}B and the radiative proton capture cross section for ^{7}Be$(p, \gamma)^8$B. A particularly interesting result is the demonstration of a correlation between the charge radius and the threshold S-factor. This section is based on work presented in Paper B.

3.3.1 Interactions

One of the main reasons, in this thesis, for studying P-wave interactions in Cluster EFT is the one-proton halo nucleus ^{8}B. It consists of a ^{7}Be core and a proton being dominantly in a relative P-wave and the one-proton separation energy of ^{8}B is $B = 0.1375$ MeV. The ground-state core of ^{7}Be has spin and parity $3/2^-$ and this state together with the proton, of spin $1/2^+$, then define two spin channels $S = 1, 2$. Both of these channels contribute to the ^{8}B(2^+) ground state via a P-wave interaction. In addition, there is an excited $1/2^-$ state of ^{7}Be, at $E_* = 0.4291$ MeV, which can combine in a P-wave with a proton to form the ^{8}B(2^+) state if the spin channel is $S = 1$. Comparing this system with the simpler case of the S-wave one-proton halo nucleus ^{17}F*, where only one channel was present, we note that the ^{8}B halo is a more involved system both counting the number of spin-coupled channels and the increased complexity due to the P-wave nature of the interaction.

The reason why the P-wave interaction introduces difficulties is the need for two independent renormalizations already at LO. This difficulty comes from the fact that the LO Dirac delta contact interaction enters with one power of the relative momentum of the proton-core pair. This momentum dependence of the interaction vertex makes the irreducible self-energy have an additional divergence compared to the S-wave case, Eq. (3.43). See Sec. 2 in Paper B, or Ref. [10], for a full derivation of these renormalization issues.

For a P-wave interaction, the Coulomb-modified ERE is given by Eq. (3.12) with $l = 1$. However, the elastic scattering process of a proton and a ^{7}Be core has a contribution from the core excitation ^{7}Be* and therefore, for the case at hand, we have the ERE

$$k^3 C(1, \eta)^2 (\cot \delta_1 - i) + 2k_C h_1(\eta) + \frac{g_*^2}{g^2} 2k_C h_1(\eta_*) = -\frac{1}{a_1} + \frac{1}{2} r_1 k^2 + \dots . \qquad (3.72)$$

In Eq. (3.72) we have introduced two new parameters: the ratio between the interaction vertices of proton-^{7}Be* and proton-^{7}Be, g_*/g, and the Coulomb parameter $\eta_* = k_C/k_*$, with $k_* = \sqrt{k^2 - 2m_R E_*}$. The effective range r_1 and the ratio g_*/g will be fitted to calculated and measured ANCs in Section 3.3.2. Details on how the ERE (3.72) is obtained from the interactions of the field theory can be found in Sec. 2 in Paper B.

The Lagrangian for a system consisting of a proton interacting with a spin-3/2 core state and a spin-1/2 excited-core state, in a relative P-wave with total spin $J = 2$, is

given by

$$
\begin{aligned}
\mathcal{L} =\,&\mathrm{p}_\sigma^\dagger\Big(iD_t+\frac{\mathbf{D}^2}{2m}\Big)\mathrm{p}_\sigma + \mathrm{c}_a^\dagger\Big(iD_t+\frac{\mathbf{D}^2}{2M}\Big)\mathrm{c}_a + \tilde{\mathrm{c}}_\sigma^\dagger\Big(iD_t+\frac{\mathbf{D}^2}{2M}-E_*\Big)\tilde{\mathrm{c}}_\sigma \\
&+ \mathrm{d}_\alpha^\dagger\Big[\Delta+\nu\Big(iD_t+\frac{\mathbf{D}^2}{2M_{\mathrm{tot}}}\Big)\Big]\mathrm{d}_\alpha \\
&- g_1\Big[\mathrm{d}_\alpha^\dagger \mathcal{C}_{ji}^\alpha \mathcal{C}_{a\sigma}^j \mathrm{c}_a \Big((1-f)i\overrightarrow{D}_i - fi\overleftarrow{D}_i\Big)\mathrm{p}_\sigma + \text{h.c.}\Big] \\
&- g_2\Big[\mathrm{d}_\alpha^\dagger \mathcal{C}_{\beta i}^\alpha \mathcal{C}_{a\sigma}^\beta \mathrm{c}_a \Big((1-f)i\overrightarrow{D}_i - fi\overleftarrow{D}_i\Big)\mathrm{p}_\sigma + \text{h.c.}\Big] \\
&- g_*\Big[\mathrm{d}_\alpha^\dagger \mathcal{C}_{ji}^\alpha \mathcal{C}_{\chi\sigma}^j \tilde{\mathrm{c}}_\chi \Big((1-f)i\overrightarrow{D}_i - fi\overleftarrow{D}_i\Big)\mathrm{p}_\sigma + \text{h.c.}\Big] \\
&+ \dots .
\end{aligned}
\tag{3.73}
$$

In this Lagrangian, the proton field is denoted by p_σ, the ground state core field by c_a, the excited state core field by $\tilde{\mathrm{c}}_\sigma$ and the spin-2^+ dicluster field by d_α. The core fields have mass M and charge eZ_{c}, the proton field has mass m and charge e, and the dicluster field has mass $M_{\mathrm{tot}}=M+m$ and charge $e(Z_{\mathrm{c}}+1)$. Note also that the excited-state core field has excitation energy E_*. The factors of $(1-f)$ and f in the interaction part of the Lagrangian (3.73) make sure that it is Galilean invariant. The interaction vertices for the ground-state core field and the proton have coupling strengths g_1 and g_2 for the two spin channels $S=1,2$. To the order that we consider, these couplings always appear in the combination $g^2=g_1^2+g_2^2$. The interaction vertex for the excited-state core field and the proton have coupling strength g_*. With the Clebsch-Gordan coefficients $\mathcal{C}$ the different interaction channels are defined, with indices according to $\alpha,\beta=-2,-1,0,1,2$, $a=-3/2,-1/2,1/2,3/2$, $i,j,k=-1,0,1$, and $\sigma,\chi=-1/2,1/2$. The covariant derivatives are given by $D_\mu=\partial_\mu+ie\hat{Q}A_\mu$. The dots refer to higher-order terms that we do not include.

The P-wave interaction vertices for the ground state core-proton-dicluster interactions are

$$
ig_1\mathcal{C}_{ji}^\alpha \mathcal{C}_{a\sigma}^j k_i \,,
\tag{3.74}
$$

for the $S=1$ channel, and

$$
ig_2\mathcal{C}_{\beta i}^\alpha \mathcal{C}_{a\sigma}^\beta k_i \,,
\tag{3.75}
$$

for the $S=2$ channel, and for the excited state core field

$$
ig_*\mathcal{C}_{ji}^\alpha \mathcal{C}_{\chi\sigma}^j k_i \,,
\tag{3.76}
$$

where $\mathbf{k}$ is the relative momentum of the proton-core pair. Therefore, in all loop-diagrams that we consider for the P-wave bound state there will be additional powers of the loop-momentum $\mathbf{k}$. We consider the most basic P-wave loop-integrals in Appendix B of Paper B. The Feynman rules for the A_0 and the A_i photon interaction with the proton, ground- and excited-state core and dicluster fields are analogous to the rules given in Section 3.2.1. However, for the P-wave interaction at hand, there is also an interaction vertex where an A_i photon is attached to a proton-core-dicluster vertex. This vertex exists for both the ground- and excited-state core, but for the purpose of obtaining the results

presented here we only need the one with the ground-state core field. The Feynman rules for this vertex is, for $S = 1$,

$$ig_1 \mathcal{C}_{ji}^{\alpha} \mathcal{C}_{a\sigma}^{j} e[1 - f(Z_c + 1)] \tag{3.77}$$

and for $S = 2$

$$ig_2 \mathcal{C}_{\beta i}^{\alpha} \mathcal{C}_{a\sigma}^{\beta} e[1 - f(Z_c + 1)] \ . \tag{3.78}$$

The bare dicluster propagator for P-wave interactions in the c.m. frame is given by

$$iD^{(0)}(E) = \frac{i}{\Delta + \nu \left(E + i\varepsilon \right)} \ , \tag{3.79}$$

taking the inverse of the kinetic term in the Lagrangian Eq. (3.73). The full dicluster propagator is obtained by dressing the bare propagator Eq. (3.79) by proton-core and proton-excited core loops, that is by including the irreducible self-energies of the proton-core and proton-excited core systems, analogous to the procedure in Chapter 3.2.1. The construction of these irreducible self-energies is given in Paper B. The resulting full dicluster propagator is

$$iD(E) = \frac{i}{\Delta + \nu \left(E + i\varepsilon \right) + \Sigma(E) + \Sigma_*(E)} \ . \tag{3.80}$$

One can understand the sum of the irreducible self-energies $\Sigma(E) + \Sigma_*(E)$ in the denominator by the fact that the propagation of the dicluster will have contributions from both the ground- and the excited-state core fields. Even higher-energy states would also contribute, had we not excluded these from the EFT. That is, these higher modes are considered short-range physics and are implicitly included in the parameters of the EFT. Note that the total irreducible self-energy $\Sigma(E) + \Sigma_*(E)$ for the P-wave interaction has two independent divergences, compared to only one for the S-wave interaction, and therefore two parameters are needed at LO to renormalize the interaction. This is independent of the fact that we have one irreducible self-energy per core field.

The wavefunction renormalization of the P-wave bound state ^{8}B system is given by

$$\mathcal{Z} = \frac{6\pi}{g^2 m_{\mathrm{R}}^2} \left[r_1 - \frac{2k_{\mathrm{C}}}{m_{\mathrm{R}}} \frac{\mathrm{d}}{\mathrm{d}E} \left(h_1(\eta) + \frac{g_*^2}{g^2} h_1(\eta_*) \right) \right]^{-1} \Bigg|_{E=-B} \ . \tag{3.81}$$

It is evident that both the ground and excited state of the ^{7}Be core contribute to the bound-state properties of ^{8}B, through the $h_1(\eta)$ and $\frac{g_*^2}{g^2} h_1(\eta_*)$ pieces. When we match to ANCs in Section 3.3.2, we will fix both the effective range r_1 and the excited-to-bound state interaction strength ratio g_*/g by matching to the ANCs relevant for the ^{8}B system. In terms of these ANCs the wavefunction renormalization can be written as

$$\mathcal{Z} = -\frac{3\pi}{g^2 m_{\mathrm{R}}^2 \gamma^2 \Gamma(2 + k_{\mathrm{C}}/\gamma)^2} \left(A_1^2 + A_2^2 \right) \tag{3.82}$$

$$= -\frac{3\pi}{g_*^2 m_{\mathrm{R}}^2 \gamma_*^2 \Gamma(2 + k_{\mathrm{C}}/\gamma_*)^2} A_*^2 \ , \tag{3.83}$$

40

Table 3.1: Relevant parameters and scales for the ^{8}B system.

k_{C}	γ	γ_*	r_1
26.79 MeV	14.97 MeV	30.39	~ 60–70 MeV

k_α	$1/R_{^7\mathrm{Be}}$	$f = m/M_{\mathrm{tot}}$	Z_{c}
50.86	74.55 MeV	1/8	4

combining Eq. (3.81) and the ANC formula in Eq. (85) of Ref. [32]. In Eqs. (3.82) and (3.83), A_1 (A_2) is the ANC for the proton and the ground-state core in the $S = 1$ ($S = 2$) channel and A_* is the ANC for the proton and excited-state core in the $S = 1$ channel. The binding momenta for the bound- and ground-state channels are defined as $\gamma = \sqrt{2m_{\mathrm{R}}B}$ and $\gamma_* = \sqrt{2m_{\mathrm{R}}(B + E_*)}$.

3.3.2 Fixing parameters

In this section we will discuss how to extract parameters from ANCs. We will use two different field theories for the P-wave system under consideration: (i) A field theory with only the ground-state core included and (ii) a field theory where the excited-state core is also included. Therefore, in the ground-state only theory the breakdown scale is given by the excited-state energy.

For the P-wave system at hand, we need to fix at least two parameters at LO to be able to make predictions, for example the binding momentum and the effective range. Thus, if we only include the ground state of the core in the field theory we would need to fit the effective range to, for example, low-energy elastic scattering data or to an extracted ANC for the bound system, consisting of a proton and a ground-state core. If the excited-core field is also included in the field theory, then an additional parameter needs to be fixed. This parameter is related to the relative importance of the ground- and excited-state core fields, that is in what proportions these fields appear in the halo state. We choose to work with the binding momentum γ of the halo nucleus, the $J = 2^+$ effective range r_1, and the ratio of the interaction strengths g_*/g as our parameters. Note that neither g_1 or g_1^* are observable, but the ratio g_*/g is, which can be seen by taking the ratio of Eqs. (3.82) and (3.83).

The binding momentum is trivially extracted from the one-proton separation energy B, as $\gamma = \sqrt{2m_{\mathrm{R}}B}$. The two remaining parameters can be fitted to the ground-state core field ANCs, A_1 and A_2. Note that ANCs are observable quantities that can be both measured experimentally and calculated in, for example, *ab initio* theories. We us the ANCs that have been calculated by (i) Nollett and Wiringa [33], (ii) Navrátil et al. [34] and measured by (iii) Tabacaru et al. [35] and the excited state core field ANC A_* calculated by Zhang et al. [28]. The A_* ANC is also a crucial input if the excited core is to be included in the field theory. The ground-state ANCs, A_1 and A_2, are for the $S = 1$ and $S = 2$ spin channels, respectively, and the excited-state ANC, A_*, is for the $S = 1$ spin channel. These ANCs are given in Table 3.2.

For the field theory with both the ground- and excited-state core fields included the

Table 3.2: Asymptotic Normalization Coefficients (ANCs) calculated by Nollett and Wiringa [33] and Zhang et al. [28] (denoted "Nollett"), by Navrátil et al. [34], and extracted from a proton-transfer reaction by Tabacaru et al. [35]. The ANCs are given in $\text{fm}^{-1/2}$ for the two spin-channels $S = 1, 2$ (A_1, A_2) and for the $S = 1$ channel with an excited core (A_*).

Ref.	A_1	A_2	A_*
"Nollett" [33], [28]	$-0.315(19)$	$-0.662(19)$	$0.3485(51)$
"Navrátil" [34]	-0.294	-0.650	–
"Tabacaru" [35]	$0.294(45)$	$0.615(45)$	–

breakdown scale k_{hi} is defined by the α-threshold at $k_\alpha = 50.86$ MeV. There is also a low-lying 1^+ resonance in ^{8}B at $E_{\text{res}} = 0.77$ MeV, but this state does not contribute to the charge form factor of the ^{8}B ground state and only contributes to the radiative capture process $^7\text{Be}(p, \gamma)^8\text{B}$ for a narrow energy region around E_{res}. The estimate for the EFT expansion parameter that determines the error is therefore $k_{\text{lo}}/k_{\text{hi}} \sim \gamma/k_\alpha = 0.29$. For the field theory with only the ground-state core field included the high-momentum scale is defined by the energy of the core excited state $\tilde{k}_{\text{hi}} \sim \sqrt{2m_{\text{R}}E_*} = 26.4$ MeV, giving the expansion parameter $k_{\text{lo}}/\tilde{k}_{\text{hi}} \sim 0.57$.

Using the ANC-formula in [32][3], and generalizing it to our case with two core fields, we have for P-waves

$$A_1^2 + A_2^2 = \left. \frac{2\gamma^2 \Gamma(2 + k_{\text{C}}/\gamma)^2}{-r_1 + \frac{2k_{\text{C}}}{m_{\text{R}}} \frac{\text{d}}{\text{d}E}\left(h_1(\eta) + \frac{g_*^2}{g^2}h_1(\eta_*)\right)} \right|_{E=-B} \tag{3.84}$$

and

$$A_*^2 = \left. \frac{2\gamma_*^2 \Gamma(2 + k_{\text{C}}/\gamma_*)^2}{-\frac{g^2}{g_*^2}r_1 + \frac{2k_{\text{C}}}{m_{\text{R}}} \frac{\text{d}}{\text{d}E}\left(\frac{g^2}{g_*^2}h_1(\eta) + h_1(\eta_*)\right)} \right|_{E=-B}. \tag{3.85}$$

Note that these ANC formulas are for a field theory with both the ground- and excited-state core fields included. For a field theory with only the ground-state core field we would only have a single ANC formula

$$A_1^2 + A_2^2 = \left. \frac{2\gamma^2 \Gamma(2 + k_{\text{C}}/\gamma)^2}{-\tilde{r}_1 + \frac{2k_{\text{C}}}{m_{\text{R}}} \frac{\text{d}}{\text{d}E}h_1(\eta)} \right|_{E=-B}, \tag{3.86}$$

where the effective range r_1 for the full field theory, and $\tilde{r}_1$ for the ground-state only field theory are different. Of course, Nature has an exact value for the effective range and r_1 and $\tilde{r}_1$ are approximations of the exact value, with EFT errors of the order $k_{\text{lo}}/k_{\text{hi}}$ and $k_{\text{lo}}/\tilde{k}_{\text{hi}}$, respectively. Note that the break-down scale is larger for the field theory that does include the excited core and therefore r_1 is likely to be a better approximation to the true effective range than the ground-state-only result $\tilde{r}_1$.

---

[3]There is a minor error in the formula Eq. (85) of [32]: the $\tilde{C}_{\eta,l}$ should be in the numerator.

Using the full field theory with both the ground- and excited-state core fields, the resulting effective range is,

$$r_1 = \begin{cases} (60 \pm 4) \text{ MeV} & \text{(Nollett ANCs)} \\ 63 \text{ MeV} & \text{(Navrátil ANCs)} \\ (69 \pm 13) \text{ MeV} & \text{(Tabararu ANCs)} \end{cases} . \qquad (3.87)$$

Note that no error is presented for the ANCs computed by Navrátil et al. [34]. If the simpler field theory is used instead, with only the ground-state core field, and with the central value of the "Nollett" ANCs, the resulting effective range is $\tilde{r}_1 = 56$ MeV, that is about 7% smaller. In this way, by including more physics successively, one can see convergence towards the physical value of the observable. Note that the effective range result presented in Eq. (3.87) is a prediction, with an estimated error $k_{\text{lo}}/k_{\text{hi}} \sim 29\%$.

The effective range scales naturally with the high momentum scale $r_1 \sim k_{\text{hi}}$. Comparing to the $^{17}\text{F}^*$ S-wave one-proton halo case, where the system is fine-tuned such that both the scattering length and effective range was needed to fix the LSZ residue of the bound state pole, we instead have that the pole is approximately determined by $1/r_1$. This is because r_1 is very large compared to the rest of the terms in the denominators of Eqs. (3.84), (3.85) and (3.86). The observation that the ^8B one-proton halo system is more natural than the $^{17}\text{F}^*$ system is connected to the fact that for ^8B we have $k_{\text{C}} \sim \gamma$, while for $^{17}\text{F}^*$ we have $k_{\text{C}} \gg \gamma$.

3.3.3 The charge form factor

As was discussed in the beginning of Chapter 3.2.2 the charge form factor is given by the interaction of the system with an off-shell A_0 photon in the Breit frame, that is Eq. (2.28). The charge form factor diagrams are derived in Sec. 3 of Paper B. The goal of this section is to calculate the charge radius r_{ch}, defined in Eq. (2.29).

In Sec. 3.B of Paper B the charge form factor loop-diagram Γ_{loop} is given and simplified. The diagrams are shown in Fig. 3.4, that is they can be visualized to be the same as for the S-wave proton halo charge form factor, but with P-wave interaction vertices of course. The resulting integral from the loop-diagrams is

$$\begin{aligned} \Gamma_{\text{loop}}(Q) = & -i3g^2 eZ_{\text{c}} \int \mathrm{d}^3 r \exp\left(if\mathbf{Q} \cdot \mathbf{r}\right) \left| \lim_{r' \to 0} \left(\frac{G_{\text{C}}^{(1)}(-B; r', r)}{r'} \right) \right|^2 \\ & -i3g_*^2 eZ_{\text{c}} \int \mathrm{d}^3 r \exp\left(if\mathbf{Q} \cdot \mathbf{r}\right) \left| \lim_{r' \to 0} \left(\frac{G_{\text{C}}^{(1)}(-B - E_*; r', r)}{r'} \right) \right|^2 \\ & + \left[(f \to 1 - f),\ (Z_{\text{c}} \to 1) \right] . \end{aligned} \qquad (3.88)$$

In Eq. (3.88) both the ground- and excited-state core field contributions are explicitly visible, as the first row is only from the ground-state core and the second row from the excited-state core field. The integrals (3.88) are solved numerically using the partial-wave projected Coulomb Green's function Eq. (3.27). The charge radius is now given by

numerical integration of the order Q^2 part of Eq. (3.88), according to Eq. (3.89)

$$r_{\mathrm{ch}}^2 = -\frac{3}{e(Z_{\mathrm{c}}+1)} \mathcal{Z} \Gamma_{\mathrm{loop}}''(0) \ , \tag{3.89}$$

Apart from the resulting charge radius it is also important that the Cluster EFT formalism gives the correct normalization of the charge form factor at $Q = 0$, that is $F_{\mathrm{C}}(0) = 1$. This is indeed the case, as shown in Sec. 3.C of Paper B.

We apply the resulting Eqs. (3.88) and (3.89), together with the partial-wave projected Coulomb Green's function (3.27), on the one-proton halo nucleus ^{8}B. As was discussed above, the ^{7}Be core has an excited state only 0.429 MeV above the ground state and therefore we use a field theory where both the ground- and excited-state core fields are included. This is the reason why the loop-integral (3.88) was derived using both of these fields. However, we may remove the excited-state core field at any time, by setting the coupling strength g_* to zero. The reason why we want to do this is because we wish to see the convergence of the observable charge radius of ^{8}B, with respect to the included physics.

The resulting charge radius of ^{8}B is

$$r_{\mathrm{ch}} = \begin{cases} (2.56 \pm 0.08) \ \mathrm{fm} & \text{(Nollett ANCs)} \\ 2.50 \ \mathrm{fm} & \text{(Navrátil ANCs)} \\ (2.41 \pm 0.18) \ \mathrm{fm} & \text{(Tabacaru ANCs)} \end{cases} , \tag{3.90}$$

where the ANCs of Nollett and Wiringa [33] (Nollett ANCs), Navrátil et al. [34] (Navrátil ANCs) and measured by Tabacaru et al. [35] (Tabacaru ANCs) have been used as input. The excited-state core field ANC A_* calculated by Zhang et al. [28] has been used for all three results in Eq. (3.90). The binding momentum $\gamma = 14.97$ MeV and the excited state energy $E_* = 0.429$ MeV has also been used as input. The errors given in Eq. (3.90) are due to the errors of the input ANCs.

If the simpler field theory is used, with only the ground-state core field and a proton, then the LO Cluster EFT result for the ^{8}B charge radius is smaller than for the full field theory result. The expected EFT error of the charge radius squared is of order $k_{\mathrm{lo}}/\tilde{k}_{\mathrm{hi}} \sim 57\%$, which propagates to an error of 25% on the charge radius. Using the Nollett ANCs for the ground-state only and the full field theory, the resulting charge radius of ^{8}B is

$$r_{\mathrm{ch}} = \begin{cases} (2.32 \pm 0.58(\mathrm{EFT}) \pm 0.08(\mathrm{ANC})) \ \mathrm{fm} & \text{, only ground state} \\ (2.56 \pm 0.35(\mathrm{EFT}) \pm 0.08(\mathrm{ANC})) \ \mathrm{fm} & \text{, ground and excited state} \end{cases} . \tag{3.91}$$

These results clearly demonstrate the convergence of the charge radius with respect to the inclusion of more physics. This convergence is not due to higher-order calculations. However, it is quite similar since a higher-order calculation would imply the implicit inclusion of more short-range physics.

At NLO in the EFT expansion there is a short-range operator $\mathrm{d}^\dagger \nabla^2 A_0 \mathrm{d}$, corresponding to a two-body current, and as of now we have no means to fit the coefficient of this operator to anything but the charge radius. Therefore we are currently limited to a LO calculation only. This restriction is due to the choice of degrees-of-freedom in our
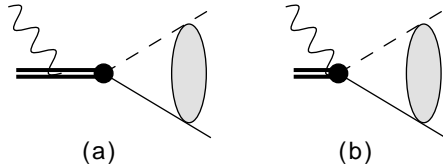
Figure 3.9: Radiative capture diagram that is present for states bound due to a P-wave interaction. The direction of time is from right to left.

model and it implies that any cluster model should have a minimum error given by this short-range operator.

One would like to add the corrections due to the finite size of the constituents. However, as is derived in Paper D, these appear at N^2LO. Therefore, in the presence of the short-range operator at NLO, it would be incorrect to add the finite-size correction to the point-particle results (3.90) and (3.91).

3.3.4 Radiative capture

In this section we will give results for the radiative capture cross section of a one-proton halo nucleus, where the constituent particles are bound due to a P-wave interaction. We exemplify the formalism by showing results for capture to the ^{8}B halo. This process is of particular interest since it determines the high-energy tail of the solar neutrino spectrum. The radiative capture process and the astrophysical S-factor was discussed and defined in Chapter 3.2.3.

Radiative capture diagrams

The LO radiative capture diagrams for a P-wave proton-core interaction are shown in Figs. 3.9 and 3.10. All these diagrams consist of an incoming Coulomb wavefunction and a final bound state. While the diagrams in Fig. 3.9 are effectively at tree level, the ones in Fig. 3.10 are more involved due to the photon-leg being attached on the momentum loop. Below we will consider these diagrams, with spin quantum numbers appropriate for the reaction ^{7}Be$(p, \gamma)^8$B.

Let us start with the diagram in Fig. 3.9(a). The photon-dicluster interaction vertex is proportional to the momentum flowing into the vertex, in Coulomb gauge, and as such this diagram is identically zero in the zero-momentum frame:

$$i\mathcal{A}^{i(\alpha)}_{1(\sigma a)} = 0 \qquad (3.92)$$

Note that we have defined the amplitude with a few indices. There is one spin-2 halo-state index α, which will be summed over, and two incoming-particle indices σ, for the spin-1/2 proton field, and a, for the spin-3/2 ground state core field, which will be averaged over. These matter-field indices are in parentheses. The superscript i will be contracted by the photon polarization vectors. The next two amplitudes below also have these indices.

45
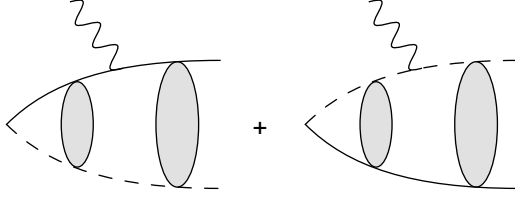
Figure 3.10: Radiative capture diagram, where the incoming proton and core interact with the real vector photon. Since the formed halo bound state is due to a P-wave interaction, the incoming proton-core pair is in a relative S- or D-wave, if only E1 capture is considered. The direction of time is from right to left.

The next diagram, Fig. 3.9(b), is effectively at tree level, which is shown in Paper B. The amplitude is given by

$$i\mathcal{A}_{2(\sigma a)}^{i(\alpha)} = ie(1 - f(Z_c + 1)) \left(g_1 \mathcal{C}_{ki}^\alpha \mathcal{C}_{\sigma a}^k + g_2 \mathcal{C}_{\beta i}^\alpha \mathcal{C}_{\sigma a}^\beta \right) \psi_{\mathbf{p}}(0) \tag{3.93}$$

Note that this contribution is completely from an incoming S-wave, since the incoming Coulomb wavefunction is evaluated at zero separation $\psi_{\mathbf{p}}(0)$.

The third contribution to the capture amplitude is from the loop-diagrams in Fig. 3.10, where the photon leg is attached to either the core or the proton field. The proton and the core propagates down to zero separation after the interaction with the photon, thereby forming a loop. The integral in momentum space is derived in Paper B and it is given by

$$\begin{aligned}
i\mathcal{A}_{3(\sigma a)}^{i(\alpha)} =& i \left(g_1 \mathcal{C}_{kj}^\alpha \mathcal{C}_{\sigma a}^k + g_2 \mathcal{C}_{\beta j}^\alpha \mathcal{C}_{\sigma a}^\beta \right) \\
&\times \int \frac{\mathrm{d}^3 k_1 \mathrm{d}^3 k_2}{(2\pi)^6} \, k_2^j \langle \mathbf{k}_2 | G_C(-B) | \mathbf{k}_1 + f\mathbf{Q} \rangle \left(-i \frac{feZ_c(-k_1^i)}{m_R} \right) \psi_{\mathbf{p}}(\mathbf{k}_1) \\
&- [(f \to 1 - f) , (Z_c \to 1)] ,
\end{aligned} \tag{3.94}$$

where the first and second (third) row comes from when the photon is attached to the core (proton) field. By using the P-wave projected Coulomb Green's function we may write the integral in a much simpler form, in terms of the Whittaker-W function and an incoming Coulomb wavefunction F_0:

$$\begin{aligned}
i\mathcal{A}_{3(\sigma a)}^{i(\alpha)} =& - \left(g_1 \mathcal{C}_{ki}^\alpha \mathcal{C}_{\sigma a}^k + g_2 \mathcal{C}_{\beta i}^\alpha \mathcal{C}_{\sigma a}^\beta \right) \frac{2\gamma p}{3} \Gamma(2 + k_C/\gamma) \exp(i\sigma_0) \\
&\times \int \mathrm{d}r \, r W_{-k_C/\gamma, 3/2}(2\gamma r) j_0(f\omega r) \partial_\rho \left(\frac{F_0(\eta, \rho)}{\rho} \right) \\
&- [(f \to 1 - f) , (Z_c \to 1)] ,
\end{aligned} \tag{3.95}$$

where $\eta = k_C/p$ and $\rho = pr$ for incoming relative momentum p. This integral is easily evaluated by numerical integration.

The S-factor for $^7\mathrm{Be}(p,\gamma)^8\mathrm{B}$

As an example of the P-wave radiative capture formalism above, we present S-factor results for the $^7\mathrm{Be}(p,\gamma)^8\mathrm{B}$ reaction. As input parameters we use the binding momentum
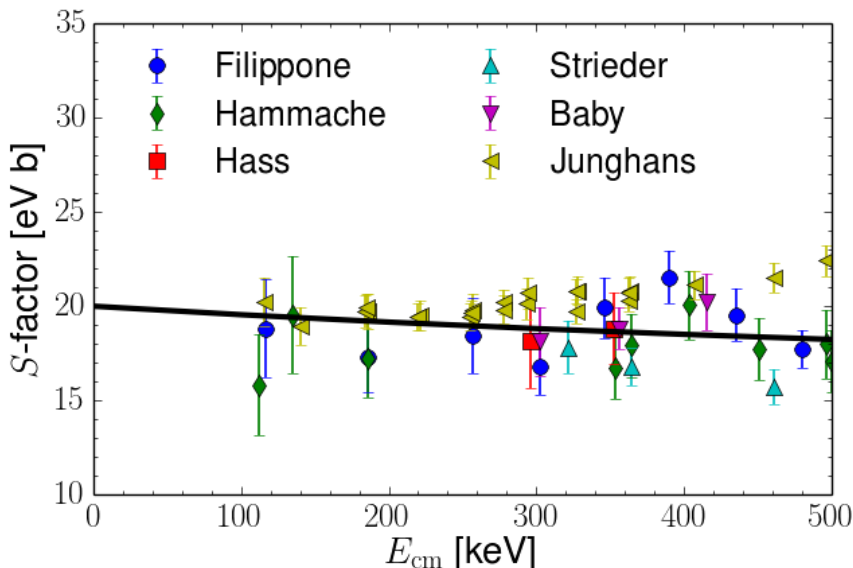
Figure 3.11: The S-factor for the radiative capture reaction $^7\text{Be}(p,\gamma)^8\text{B}$ as a function of c.m. energy. The data are from Refs. [36, 37, 38, 39, 40, 41, 42, 43] and the solid line is the LO Cluster EFT result using the "Nollett" ANCs as input.

γ of the ^8B one-proton halo and the ANCs for the $S = 1, 2$ channels A_1 and A_2. The ANCs were discussed in Chapter 3.3.2 and we use the same list of three different sets of ANCs (see Table 3.2). In the subsequent section, we shall instead correlate the threshold S-factor with the charge radius of ^8B.

The resulting S-factor, using ANCs as input, is shown in black in Fig. 3.11, together with experimental data from Refs. [36, 37, 38, 39, 40, 41, 42, 43]. The Cluster EFT result presented here follows the experimental data well for low energies, but at higher energies there will be an increasing discrepancy due to the non-inclusion of initial-wave scattering, the M1-resonance, plus higher-order operators. In addition, the neglected D-wave component of the incoming Coulomb wavefunction becomes important for higher energies. The obtained threshold value, using the different available ANCs, is

$$S(0) = \begin{cases} (20.0 \pm 1.4) \text{ eV b} & \text{(Nollett ANCs)} \\ 18.9 \text{ eV b} & \text{(Navrátil ANCs)} \\ (17.3 \pm 3.0) \text{ eV b} & \text{(Tabacaru ANCs)} \end{cases} . \tag{3.96}$$

The errors presented for the Cluster EFT result (3.96) are due to the error on the input ANCs. These Cluster EFT results are in accordance with the currently accepted value [44], obtained through extrapolation of compiled experimental data, $S(0) = (20.8 \pm 0.7(\text{expt.}) \pm 1.4(\text{theor.}))$ eV b. For Cluster EFT results with initial-wave scattering and the D-wave component included, see Zhang et al. [28].

Apart from the ANC errors, there is also an EFT error due to the calculation being

at LO. We can separate the EFT error into two distinct parts: (i) The error due to the contact interactions being at LO, that is the exclusion of low-energy scattering parameters in the ERE above the effective range term and (ii) the exclusion of short-range photon-interaction vertices. Since ANCs are used as input, there will be an error on the low-energy scattering parameters extracted, of the order of the EFT expansion parameter. However, due to the fact that the threshold S-factor is directly proportional to the LSZ factor, which in turn is proportional to the ANCs squared, there is no need to extract the effective range parameters to predict the S-factor. This means that there is no EFT error due to the ERE since the ANCs are used as input. The higher-order photon couplings must enter with additional powers of the photon energy ω and the energy of the photon is approximately given by $\omega \approx B$ at threshold, for one-proton separation energies much smaller than the total mass of the system. Therefore, at threshold, the estimated EFT error due to short-range photon operators is of the order $k_{\mathrm{lo}}^2/k_{\mathrm{hi}}^2$, which is small. Note that this means that the calculation is actually to NLO. For the ^{8}B system under consideration, the EFT error is $\sim 9\%$, using $k_{\mathrm{lo}} = 14.97$ MeV and $k_{\mathrm{hi}} \sim k_\alpha = 50.86$ MeV. We therefore have a rather small LO EFT error at threshold for the S-factor. Note however that the error due to the short-range photon couplings should grow with energy; for example at a c.m. energy $E = 0.5$ MeV this error should be of order $\sim 40\%$. In addition, at these energies there are also errors due to the neglected D-wave component and initial-wave scattering, see [28] for an EFT treatment of this same system, but with the initial wave scattering and the D-wave component included, and [45] for a higher-order calculation.

While the result of this section is interesting on its own, the main result of our work on the ^{7}Be$(p,\gamma)^8$B reaction is when this reaction is put in relation to the charge radius of the halo nucleus ^{8}B. We will now turn our attention to the correlation of these two observables.

3.3.5 Correlating the threshold S-factor and charge radius of ^{8}B

In this section we use the fact that both the threshold S-factor for the radiative capture reaction ^{7}Be$(p,\gamma)^8$B and the charge radius of ^{8}B are free of short-range operators at LO. This will allow us to show a LO correlation between these two observables. Such a correlation is very useful since it is experimentally very difficult to measure the low-energy capture cross section, while a very precise charge radius measurement of ^{8}B is planned to take place in the near future. The charge radius will be measured through the atomic isotope shift, which should be very accurate. However, the resulting charge radius is then given relative to that of another boron isotope. The main source of error in such a measurement is therefore expected to be due to the uncertainty in the charge radius of the reference nucleus.

This correlation can be seen as using the effective range, or the sum of squared ground-state ANCs $A_1^2 + A_2^2$, as a free parameter. The parameters k_{C}, γ, γ_* in Table 3.1 and the excited state ANC, A_*, given in Table 3.2 are used as fixed input for the calculation. Since the correlation is at LO, the expected EFT error for the charge radius is 29%, as discussed above in Chapter 3.3.2. This uncertainty is too large to be able to compete with more sophisticated methods. However, if the EFT for this system can be extended to include more physics or if an actual higher-order calculation can be made, the error can
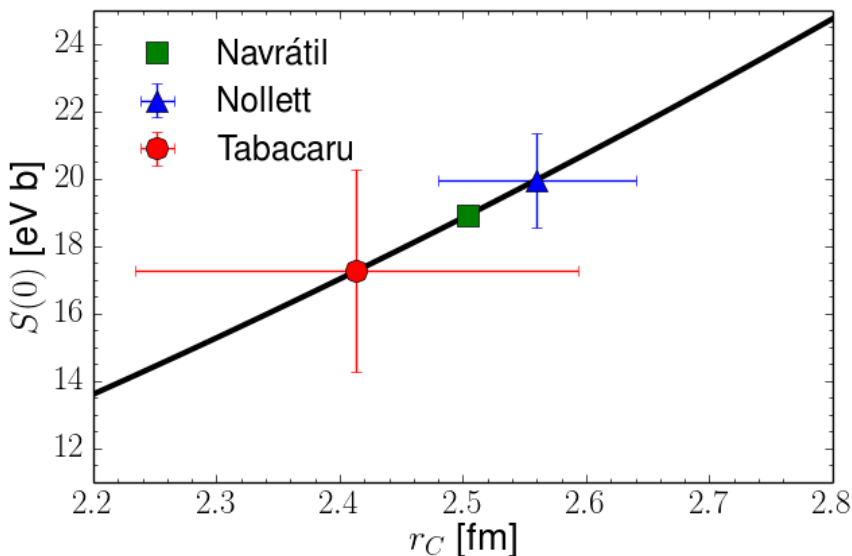
Figure 3.12: The LO Cluster EFT correlation plot, between the threshold S-factor and the charge radius of ^{8}B. The three data points with error bars correspond to results obtained with input ANCs from Nollett and Wiringa [33], Navrátil et al. [34] and Tabacaru et al. [35]. The error bars are due to the errors on the extracted ANCs.

be brought down. At that point this procedure would provide a model independent way of determining the threshold S-factor without having to rely on extrapolations. However, since there is an undetermined short-range operator already at NLO for the charge radius of the P-wave system, this correlation is most likely restricted to LO.

The LO correlation plot is shown in Fig. 3.12. The solid line shows the Cluster EFT correlation result, while the triangle, square and circle show the Cluster EFT results using the ANCs from Nollett, Navrátil and Tabacaru, respectively. For this LO Cluster EFT prediction, only points on the solid line are allowed, and these points correspond to different values of the effective range, or the sum of squared ground-state ANCs $A_1^2 + A_2^2$. The error bars shown in the correlation plot are due to the errors on the extracted ANCs. The expected EFT error of 29% on the charge radius squared is understood to be present. Note that due to this large EFT error a measurement of the ^{8}B charge radius of around 2.8 fm would be consistent with a threshold S-factor of 20 eV b, as can be seen by comparing the charge radius result with EFT errors (3.91) and the correlation plot Fig. 3.12.

4 Three-body bound and resonant states

In this chapter we present the formalism for treating bound and resonant states of three-body systems in Cluster EFT, with focus on the ^{6}He nucleus. We view this system as consisting of an α-particle and two neutrons and we include the S-wave dineutron channel and both the $3/2^-$ and $1/2^-$ α+n P-wave channels. In order to achieve proper renormalization we consider the three-body interactions of lowest scaling dimension. The contents of this chapter builds upon the work in Paper E, but also includes some preliminary results on resonant states in the three-body system.

4.1 Lagrangian

The fields that are included in this field theory are the $1/2^+$ neutron, n_σ, the 0^+ α core, c, the 0^+ dineutron field, b, the ^{5}He($3/2^-$) field, d_a, and the ^{5}He($1/2^-$) field, $\tilde{d}_\sigma$. The spin indices are defined as $\sigma = -1/2, 1/2$ and $a = -3/2, -1/2, 1/2, 3/2$. We will also use χ as a spin-1/2 index and b as a spin-3/2 index.

We write the Lagrangian as a sum of a one-body, a two-body and a three-body part:

$$\mathcal{L} = \mathcal{L}^{(1)} + \mathcal{L}^{(2)} + \mathcal{L}^{(3)} \tag{4.1}$$

The one body part is

$$\mathcal{L}^{(1)} = c^\dagger \left[i\partial_t + \frac{\nabla^2}{8m} \right] c + n_\sigma^\dagger \left[i\partial_t + \frac{\nabla^2}{2m} \right] n_\sigma + \dots \, , \tag{4.2}$$

where the neutron (core) mass is m ($4m$) and minimal substitution has not been performed since we will not consider electromagnetic observables. The dots refer to relativistic corrections.

The two-body Lagrangian is given by

$$
\begin{aligned}
\mathcal{L}^{(2)} = & d_a^\dagger \left[\Delta_1 + \nu_1 \left(i\partial_t + \frac{\nabla^2}{10m} \right) \right] d_a + g_1 \mathcal{C}_{i\chi}^a \left[d_a^\dagger c \left(\frac{4}{5} i \overrightarrow{\nabla}_i - \frac{1}{5} i \overleftarrow{\nabla}_i \right) n_\chi + \text{h.c.} \right] \\
& + \tilde{d}_\sigma^\dagger \left[\tilde{\Delta}_1 + \tilde{\nu}_1 \left(i\partial_t + \frac{\nabla^2}{10m} \right) \right] \tilde{d}_\sigma + \tilde{g}_1 \mathcal{C}_{i\chi}^\sigma \left[\tilde{d}_\sigma^\dagger c \left(\frac{4}{5} i \overrightarrow{\nabla}_i - \frac{1}{5} i \overleftarrow{\nabla}_i \right) n_\chi + \text{h.c.} \right] \\
& + b^\dagger \Delta_0 b + \frac{1}{2} g_0 \mathcal{C}_{\sigma\chi}^0 \left(b^\dagger n_\sigma n_\chi + \text{h.c.} \right) + \dots \, .
\end{aligned}
\tag{4.3}
$$

The parameters Δ_1, ν_1 and g_1 define the neutron-core P-wave interaction in the $3/2^-$ channel, $\tilde{\Delta}_1$, $\tilde{\nu}_1$ and $\tilde{g}_1$ define the neutron-core P-wave interaction in the $1/2^-$ channel, and Δ_0 and g_0 define the neutron-neutron S-wave interaction in the 0^+ channel. All other channels and interactions are not included explicitly in this field theory. The Clebsch-Gordan coefficients, $\mathcal{C}_{i\chi}^a = \langle 1i \frac{1}{2}\chi | \left(1\frac{1}{2} \right) \frac{3}{2} a \rangle$, $\mathcal{C}_{i\chi}^\sigma = \langle 1i \frac{1}{2}\chi | \left(1\frac{1}{2} \right) \frac{1}{2}\sigma \rangle$ and $\mathcal{C}_{\sigma\chi}^0 = \langle \frac{1}{2}\sigma \frac{1}{2}\chi | \left(\frac{1}{2}\frac{1}{2} \right) 00 \rangle$, and the Galilean invariant P-wave operators $\left(\frac{4}{5} i \overrightarrow{\nabla}_i - \frac{1}{5} i \overleftarrow{\nabla}_i \right)$ make sure that the interactions are in the proper channel. The dots denote higher-order two-body interactions that we will not consider.

The 0^+ three-body Lagrangian is

$$
\begin{aligned}
\mathcal{L}^{(3,0^+)} =\, & h_1^{(0^+)} \mathcal{C}^0_{a\chi i} \mathcal{C}^0_{a'\chi' i'} \left(d_a^\dagger i \overleftrightarrow{\nabla}_i n_\chi^\dagger \right) \left(d_{a'} i \overleftrightarrow{\nabla}_{i'} n_{\chi'} \right) \\
& + h_2^{(0^+)} \mathcal{C}^0_{\sigma\chi i} \mathcal{C}^0_{a'\chi' i'} \left[\left(\tilde{d}_\sigma^\dagger i \overleftrightarrow{\nabla}_i n_\chi^\dagger \right) \left(d_{a'} i \overleftrightarrow{\nabla}_{i'} n_{\chi'} \right) + \text{h.c.} \right] \\
& + h_3^{(0^+)} \mathcal{C}^0_{\sigma\chi i} \mathcal{C}^0_{\sigma'\chi' i'} \left(\tilde{d}_\sigma^\dagger i \overleftrightarrow{\nabla}_i n_\chi^\dagger \right) \left(\tilde{d}_{\sigma'} i \overleftrightarrow{\nabla}_{i'} n_{\chi'} \right) \\
& + h_4^{(0^+)} b^\dagger c^\dagger b c \\
& + h_5^{(0^+)} \mathcal{C}^0_{a\chi i} \left[\left(d_a^\dagger i \overleftrightarrow{\nabla}_i n_\chi^\dagger \right) bc + \text{h.c.} \right] \\
& + h_6^{(0^+)} \mathcal{C}^0_{\sigma\chi i} \left[\left(\tilde{d}_\sigma^\dagger i \overleftrightarrow{\nabla}_i n_\chi^\dagger \right) bc + \text{h.c.} \right] + \dots \,.
\end{aligned}
\tag{4.4}
$$

The Galilean invariant P-wave interaction operators are defined as $\overleftrightarrow{\nabla} = \frac{5}{6}\overrightarrow{\nabla} - \frac{1}{6}\overleftarrow{\nabla}$. The Clebsch-Gordan-like coefficents are defined as $\mathcal{C}^0_{a\chi i} = \mathcal{C}^j_{a\chi} \mathcal{C}^0_{ij}$ and $\mathcal{C}^0_{\sigma\chi i} = \mathcal{C}^j_{\sigma\chi} \mathcal{C}^0_{ij}$. All the explicit terms in this Lagrangian part are of dimension 7 and, as such, they should enter at N^{2}LO since LO is at dimension 5. We can see this by the fact that the matter fields, n and c, have dimension $3/2$, the P-wave dicluster fields, d and $\tilde{d}$, are of scaling dimension 1, the S-wave dineutron field, b, has scaling dimension 2 and the derivative operators have dimension 1. The dots refer to three-body terms of even higher scaling dimension. However, due to renormalization issues there is a need for a three-body interaction to be promoted to LO. In previous papers only the $h_1^{(0^+)}$-term has been considered [12, 13]. The main two arguments for such a treatment are that (i) the S-wave three-body interactions is viewed as suppressed since the actual α-dineutron interaction is Pauli blocked and (ii) the $3/2^-$ channel should be dominant since it is related to a lower momentum scale than the $1/2^-$ channel. According to this, the ^{5}He($3/2^-$)+neutron to ^{5}He($3/2^-$)+neutron diagonal three-body interaction, that is the $h_1^{0^+}$ term, should be of most importance. However, this does not mean that only one three-body interaction is needed for numerically sane results to be obtainable or to achieve proper renormalization. The other two diagonal three-body interactions of the Lagrangian part (4.4) is the $h_3^{(0^+)}$, where we start and end with ^{5}He($1/2^-$)+neutron, and the $h_4^{(0^+)}$ interaction, where we start and end with dineutron+α legs. The other three interaction terms are mixed terms, or off-diagonal, as the incoming legs differ from the outgoing.

As an example we also present the 2^+ part of the three-body Lagrangian:

$$
\begin{aligned}
\mathcal{L}^{(3,2^+)} =\, & h_1^{(2^+)} \mathcal{C}^\mu_{a\chi i} \mathcal{C}^\mu_{a'\chi' i'} \left(d_a^\dagger i \overleftrightarrow{\nabla}_i n_\chi^\dagger \right) \left(d_{a'} i \overleftrightarrow{\nabla}_{i'} n_{\chi'} \right) \\
& + h_2^{(2^+)} \mathcal{C}^\mu_{\sigma\chi i} \mathcal{C}^\mu_{a'\chi' i'} \left[\left(\tilde{d}_\sigma^\dagger i \overleftrightarrow{\nabla}_i n_\chi^\dagger \right) \left(d_{a'} i \overleftrightarrow{\nabla}_{i'} n_{\chi'} \right) + \text{h.c.} \right] \\
& + h_3^{(2^+)} \mathcal{C}^\mu_{\sigma\chi i} \mathcal{C}^\mu_{\sigma'\chi' i'} \left(\tilde{d}_\sigma^\dagger i \overleftrightarrow{\nabla}_i n_\chi^\dagger \right) \left(\tilde{d}_{\sigma'} i \overleftrightarrow{\nabla}_{i'} n_{\chi'} \right) + \dots
\end{aligned}
\tag{4.5}
$$

The terms that are shown explicitly here are of dimension 7. The Clebsch-Gordan-like coefficents are defined as $\mathcal{C}^\mu_{a\chi i} = \mathcal{C}^j_{a\chi} \mathcal{C}^\mu_{ij} + \mathcal{C}^\nu_{a\chi} \mathcal{C}^\mu_{i\nu}$ and $\mathcal{C}^\mu_{\sigma\chi i} = \mathcal{C}^j_{\sigma\chi} \mathcal{C}^\mu_{ij}$, where $\mu, \nu = -2, -1, 0, 1, 2$. There are also terms involving the dineutron field b, but these are of higher
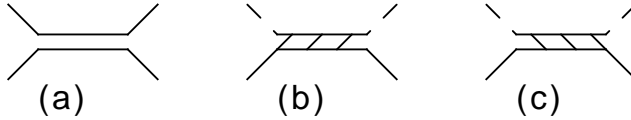
Figure 4.1: Elastic scattering in the two-body subsystems of ^{6}He. (a) The neutron-neutron scattering diagram. The full dineutron propagator is denoted by the double line. (b) The α-n elastic scattering diagram in the $3/2^-$ channel. The full ^{5}He($3/2^-$) dicluster propagator is denoted by the double line with internal bottom-to-top right tilted lines. (c) The α-n elastic scattering diagram in the $1/2^-$ channel. The full ^{5}He($1/2^-$) dicluster propagator is denoted by the double line with internal bottom-to-top left tilted lines.

scaling dimension. For example, at dimension 9 there is a term

$$
\mathcal{C}_{ij}^{\mu}\mathcal{C}_{a\chi'i'}^{\mu}\left[\left(b^{\dagger}\overleftrightarrow{\mathcal{O}}_{ij}c^{\dagger}\right)\left(d_{a'}i\overleftrightarrow{\nabla}_{i'}n_{\chi'}\right)+\text{h.c.}\right] \ , \tag{4.6}
$$

where

$$
\begin{aligned}
\overleftrightarrow{\mathcal{O}}_{ij} =& \frac{1}{9}\left(\overrightarrow{\nabla}_i\overrightarrow{\nabla}_j - \frac{1}{3}\delta_{ij}\overrightarrow{\nabla}^2\right) + \frac{4}{9}\left(\overleftarrow{\nabla}_i\overleftarrow{\nabla}_j - \frac{1}{3}\delta_{ij}\overleftarrow{\nabla}^2\right) \\
&- \frac{2}{9}\left(\overleftarrow{\nabla}_i\overrightarrow{\nabla}_j + \overleftarrow{\nabla}_j\overrightarrow{\nabla}_i - \frac{2}{3}\delta_{ij}\overleftarrow{\nabla}\cdot\overrightarrow{\nabla}\right)
\end{aligned} \tag{4.7}
$$

is the Galilean invariant D-wave interaction operator. Such higher-order terms are denoted by the dots. As such the three-body sector in the 2^+ channel seems to be less complicated than that of the 0^+ channel, since less three-body interactions are present at the lowest scaling dimension.

4.2   Two-body physics

In this section we define the relevant dicluster propagators for the ^{6}He system. We also discuss three different prescriptions regarding how to handle the unphysical pole of the P-wave dicluster propagators.

4.2.1   The dineutron subsystem

The neutron-neutron S-wave interaction has an unnaturally large scattering length, $a_0 = -18.9$ fm, and as such the interaction needs to be summed to all orders. From the two-body Lagrangian (4.3) we can write down the bare LO dineutron propagator

$$
iB^{(0)}(E,\mathbf{p}) = \frac{i}{\Delta_0} \ . \tag{4.8}
$$

We have written the propagator for a four-momentum $(E,\mathbf{p})$, but note that the propagator is static at LO. Summing the interaction to all orders in the parameter g_0, we arrive at

the full dineutron propagator

$$iB(E, \mathbf{p}) = \frac{i}{\Delta_0 + \Sigma_0(E, \mathbf{p})} \ , \tag{4.9}$$

where the irreducible self-energy is given by

$$\Sigma_0(E, \mathbf{p}) = \frac{g_0^2 m}{2\pi^2} \left[L_1 - \frac{i\pi}{2} \sqrt{mE - \frac{\mathbf{p}^2}{4}} \right] \ . \tag{4.10}$$

The divergence L_1, defined in Eq. (2.13), is absorbed by the parameter Δ_0. The neutron-neutron scattering diagram is shown in Fig. 4.1(a), where also the graphics of the full dineutron propagator is defined. Matching to the t-matrix and the ERE parameters, we may write the full propagator as

$$B(E, \mathbf{p}) = \frac{4\pi}{g_0^2 m} \frac{1}{\frac{1}{a_0} + i\sqrt{m\left(E - \frac{\mathbf{p}^2}{4m}\right)}} \ . \tag{4.11}$$

The expression (4.11) then defines the S-wave neutron-neutron scattering at LO. For more details on S-wave elastic scattering and renormalization, see Sec. 2.1.2.

4.2.2 The ^{5}He subsystem

In the ^{5}He subsystem there are two low-lying resonances, the $3/2^-$ state with energy position and width $E^{(3/2^-)} = 0.798$ MeV and $\Gamma^{(3/2^-)} = 0.648$ MeV and the $1/2^-$ state with $E^{(1/2^-)} = 2.07$ MeV and $\Gamma^{(1/2^-)} = 5.57$ MeV. We expect the $3/2^-$ to be the most important of these two channels, since it is lower in energy. However, a field theory in which the $1/2^-$ is also included can be expected to give higher accuracy. For the scalings of the P-wave ERE parameters we will assume that the effective ranges scale as k_{hi} and the scattering lengths scale as $1/(k_{\mathrm{lo}}^2 k_{\mathrm{hi}})$.

From the Lagrangian part (4.3) we have that the P-wave $3/2^-$ field has a bare dicluster propagator at LO

$$iD^{(0)}(E, \mathbf{p}) = \frac{i}{\Delta_1 + \nu_1 \left(E - \frac{\mathbf{p}^2}{10m} \right)} \ . \tag{4.12}$$

Resumming the interaction we arrive at the full dicluster propagator, that is with the irreducible self energy included:

$$iD(E, \mathbf{p}) = \frac{i}{\Delta_1 + \nu_1 \left(E - \frac{\mathbf{p}^2}{10m} \right) + \Sigma_1(E, \mathbf{p})} \tag{4.13}$$

For the P-wave $3/2^-$ the irreducible self energy is given by

$$\Sigma(E, \mathbf{p}) = \frac{4g_1^2 m}{15\pi^2} \left[L_3 + \left(\frac{8mE}{5} - \mathbf{p}^2 \right) L_1 - \frac{i\pi}{2} \left(\frac{8mE}{5} - \mathbf{p}^2 \right)^{3/2} \right] \ . \tag{4.14}$$

Note in particular that there are two independent divergences, L_1 and L_3, which are absorbed by the parameter Δ_1 and the ν_1 term. The α-neutron scattering diagram in the $3/2^-$ channel is shown in Fig. 4.1(b), where also the graphics of the full ^{5}He($3/2^-$) dicluster propagator is defined. If we match to the $3/2^-$ t-matrix we can write the full dicluster propagator at LO as

$$D(E, \mathbf{p}) = \frac{15\pi}{2mg_1^2} \frac{1}{\frac{1}{a_1} - \frac{1}{2}r_1\left(\frac{8mE}{5} - \mathbf{p}^2\right) + i\left(\frac{8mE}{5} - \mathbf{p}^2\right)^{3/2}} \, , \tag{4.15}$$

in terms of the $3/2^-$ ERE parameters a_1 and r_1.

The $1/2^-$ dicluster propagator is given in the same way as above. The difference is simply that we replace $g_1, \Delta_1, \nu_1, \Sigma_1, a_1, r_1 \mapsto \tilde{g}_1, \tilde{\Delta}_1, \tilde{\nu}_1, \tilde{\Sigma}_1, \tilde{a}_1, \tilde{r}_1$ in Eqs. (4.12)–(4.15). The resulting $1/2^-$ full dicluster propagator at LO is therefore written as

$$\tilde{D}(E, \mathbf{p}) = \frac{15\pi}{2m\tilde{g}_1^2} \frac{1}{\frac{1}{\tilde{a}_1} - \frac{1}{2}\tilde{r}_1\left(\frac{8mE}{5} - \mathbf{p}^2\right) + i\left(\frac{8mE}{5} - \mathbf{p}^2\right)^{3/2}} \, . \tag{4.16}$$

The α-neutron scattering diagram in the $1/2^-$ channel is shown in Fig. 4.1(c), where also the graphics of the full ^{5}He($1/2^-$) dicluster propagator is defined.

From the pole structure of the propagators (4.15) and (4.16) we can extract the values of the scattering lengths $a_1, \tilde{a}_1$ and effective ranges $r_1, \tilde{r}_1$, since we know the pole positions and widths of the $3/2^-$ and $1/2^-$ resonances. We obtain $a_1 = -76.12$ fm^3, $r_1 = -141.84$ MeV, $\tilde{a}_1 = -60.37$ fm^3 and $\tilde{r}_1 = 66.87$ MeV. However, analyzing the pole structure of the P-wave dicluster propagators we also find poles at negative energy, that is we also have unphysical bound states present in the field theory. The reason for these unphysical states to be present is the finite number of terms included in the ERE. If we do not remove these unphysical states in some way, there will be issues when we later evaluate the three-body integral equations. As such we will now turn to three different prescriptions, that were discussed in Paper E, of how to modify the two-body sector such that the unphysical states are removed.

In Ref. [13] the issue with the unphysical state in the $3/2^-$ channel was solved by removing the unitarity piece, ik^3, in the dicluster propagator (4.15). One can argue that this can be done since at low momentum the ik^3 term is negligible compared to the remaining $1/a_1$ and $r_1k^2/2$ terms, if it is assumed that $r_1 \sim k_{\text{hi}}$ and $1/a_1 \sim k_{\text{lo}}^2 k_{\text{hi}}$. Such a prescription is thus only only valid at LO. The resulting propagator in this unitarity piece removal prescription (UP) is

$$D^{(\text{UP})}(E, \mathbf{p}) = \frac{15\pi}{2mg_1^2} \frac{1}{\frac{1}{a_1} - \frac{1}{2}r_1k^2} \, , \tag{4.17}$$

where $k = \sqrt{\frac{8mE}{5} - \mathbf{p}^2}$. Note that this expression only have real momentum poles. As such, the UP moves the resonance to the real momentum axis. If we consider the low-momentum physics of the propagator (4.17) we note that the UP does not change the values of the scattering length and the effective range, that is low-momentum physics is unchanged.

Another way to handle the unphysical pole would be to simply remove it by subtracting $\frac{\mathcal{R}_0}{k - k_0}$ from the dicluster propagator. We call this the subtraction prescription (SP). Here, we have defined the quantities k_0 and $\mathcal{R}_0$ to denote the unphysical pole position in momentum and the corresponding residue. The resulting propagator in the SP is then given by

$$D^{(\text{SP})}(E, \mathbf{p}) = \frac{15\pi}{2mg_1^2} \frac{1}{\frac{1}{a_1} - \frac{1}{2}r_1 k^2 + ik^3} - \frac{\mathcal{R}_0}{k - k_0} \;, \tag{4.18}$$

On the bright side, the SP removes the unphysical pole without moving the physical resonance. However, by analyzing the low-momentum physics of the SP we see that it does change the values of the ERE parameters.

A third prescription is what we call the expansion prescription (EP), for which the unphysical pole is expanded to the second order in momentum. We can write this as

$$\begin{aligned} D^{(\text{EP})}(E, \mathbf{p}) =& \frac{15\pi}{2mg_1^2} \frac{1}{\frac{1}{a_1} - \frac{1}{2}r_1 k^2 + ik^3} \\ &- \mathcal{R}_0 \left(\frac{1}{k - k_0} + \frac{1}{k_0} + \frac{k}{k_0^2} + \frac{k^2}{k_0^3} \right) \;. \end{aligned} \tag{4.19}$$

The EP does not move the physical pole and it leaves the low-momentum physics unchanged, up to second order. Therefore the EP is preferable from a physics perspective. However, the large-momentum asymptotics does become severely modified. The reason is that the propagator now behaves as k^2, compared to $1/k^2$ asymptotics for the UP and SP. From an EFT perspective this should not introduce any problems, if we only renormalize the theory properly. Said in another way, the large-momentum asymptotics can be absorbed in the three-body interaction parameters. Note, however, that for very large momenta there can be numerical issues due to the momentum-squared dependence, and as such we expect that the EP will be limited to lower cutoffs than the UP or SP.

4.3   Three-body scattering diagrams

We now turn to the derivation of the three-body scattering diagrams. These diagrams are shown in Fig. 4.2. In total, we need three scattering amplitudes to close the integral equations: (i) The A-amplitude, with an incoming $^5\text{He}(3/2^-)$ dicluster field and a neutron field, (ii) the B-amplitude, with an incoming $^5\text{He}(1/2^-)$ dicluster field and a neutron field, and (iii) the C-amplitude with an incoming dineutron dicluster field and an α-particle field. For all three ampitudes the outgoing fields are choosen to be a $^5\text{He}(3/2^-)$ dicluster field and a neutron field. The $^5\text{He}(3/2^-)$ dicluster field is shown as a double line with internal bottom-to-top right tilted lines, the $^5\text{He}(1/2^-)$ dicluster field is shown as a double line with internal bottom-to-top left tilted lines, and the dineutron dicluster field is shown as just a double line.

On the first line for each of the amplitudes in Fig. 4.2 the two inhomogeneous terms are shown. The first inhomogeneous term for each amplitude is simply the exchange of a neutron, shown as a solid line, or an α-particle, shown as a dashed line. The second inhomogeneous term of each amplitude is due to the relevant three-body interaction. For
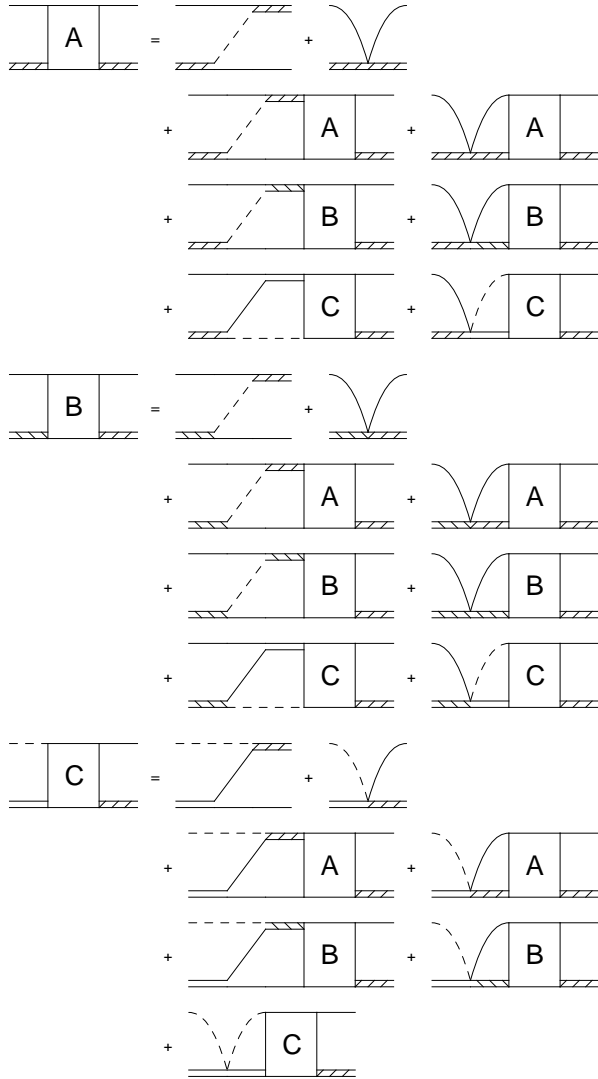
Figure 4.2: The three-body scattering diagrams. Since there are three two-body channels the scattering equation is given by a coupled integral equation of three parts.

the A-amplitude it is the $h_1^{(J^\pi)}$ that is responsible, while for the B- and C- amplitudes it is the $h_2^{(J^\pi)}$ and $h_5^{(J^\pi)}$, respectively, that give those terms (see Eq. (4.4)). For the 0^+

channel these inhomogeneous amplitudes are given by the following expressions:

$$iA_{(0^+)}^{(\text{inhom.})}(k,p) = -ig_1^2 \frac{16\pi m}{3} K_{(0^+)}^{(AA)}(k,p) \tag{4.20}$$

$$iB_{(0^+)}^{(\text{inhom.})}(k,p) = -ig_1\tilde{g}_1 \frac{16\pi m}{3} K_{(0^+)}^{(BA)}(k,p) \tag{4.21}$$

$$iC_{(0^+)}^{(\text{inhom.})}(k,p) = 2ig_0 g_1 \frac{8\pi m}{\sqrt{6}} K_{(0^+)}^{(CA)}(k,p) \tag{4.22}$$

We have defined the incoming (outgoing) momentum of the dicluster lines as $\mathbf{k}$ ($\mathbf{p}$) and since we work in the c.m. frame the single-particle lines are at momentum $-\mathbf{k}$ ($-\mathbf{p}$). We denote the total energy flowing through the diagram by E. The 0^+ kernels $K_{(0^+)}^{(XY)}$, for $X,Y = A,B,C$, are defined as

$$K_{(0^+)}^{(AA)}(k,p) = \frac{27}{25} Q_0(\rho_1(k,p)) + \frac{2}{5} \frac{k^2+p^2}{kp} Q_1(\rho_1(k,p)) + Q_2(\rho_1(k,p))$$
$$- H_1^{(0^+)} \frac{kp}{\Lambda^2} , \tag{4.23}$$

$$K_{(0^+)}^{(AB)}(k,p) = K_{(0^+)}^{(BA)}(k,p)$$
$$= \frac{\sqrt{2}}{25} Q_0(\rho_1(k,p)) + \frac{\sqrt{2}}{5} \frac{k^2+p^2}{kp} Q_1(\rho_1(k,p)) + \sqrt{2} Q_2(\rho_1(k,p))$$
$$- H_2^{(0^+)} \frac{kp}{\Lambda^2} , \tag{4.24}$$

$$K_{(0^+)}^{(AC)}(k,p) = K_{(0^+)}^{(CA)}(p,k)$$
$$= \frac{4}{5p} Q_0(\rho_2(k,p)) + \frac{1}{k} Q_1(\rho_2(k,p)) - H_5^{(0^+)} \frac{k}{\Lambda^2} , \tag{4.25}$$

$$K_{(0^+)}^{(BB)}(k,p) = \frac{26}{25} Q_0(\rho_1(k,p)) + \frac{1}{5} \frac{k^2+q^2}{kq} Q_1(\rho_1(k,q)) - H_3^{(0^+)} \frac{kp}{\Lambda^2} , \tag{4.26}$$

$$K_{(0^+)}^{(BC)}(k,p) = K_{(0^+)}^{(CB)}(p,k)$$
$$= \frac{4}{5\sqrt{2}p} Q_0(\rho_2(k,p)) + \frac{1}{\sqrt{2}k} Q_1(\rho_2(k,p)) - H_6^{(0^+)} \frac{k}{\Lambda^2} , \tag{4.27}$$

$$K_{(0^+)}^{(CC)}(k,p) = -H_4^{(0^+)} \frac{1}{\Lambda^2} . \tag{4.28}$$

The arguments to the Legendre-Q functions Q_L are given by

$$\rho_1(k,p) = \frac{4mE}{kp} - \frac{5k}{2p} - \frac{5p}{2k} , \tag{4.29}$$

$$\rho_2(k,p) = \frac{mE}{kp} - \frac{k}{p} - \frac{5p}{8k} . \tag{4.30}$$

In Eqs. (4.23)–(4.28) we have introduced new three-body parameters, in terms of the cutoff Λ, the two-body interaction g-paramters and the old three-body h-parameters.

These new parameters are defined according to

$$H_1^{(0^+)} = \frac{h_1^{(0^+)}}{4mg_1^2}\Lambda^2 \tag{4.31}$$

$$H_2^{(0^+)} = \frac{h_2^{(0^+)}}{4mg_1\tilde{g}_1}\Lambda^2 \tag{4.32}$$

$$H_3^{(0^+)} = \frac{h_3^{(0^+)}}{4m\tilde{g}_1^2}\Lambda^2 \tag{4.33}$$

$$H_4^{(0^+)} = \frac{h_4^{(0^+)}}{mg_0^2}\Lambda^2 \tag{4.34}$$

$$H_5^{(0^+)} = \frac{h_5^{(0^+)}}{\sqrt{2}mg_0g_1}\Lambda^2 \tag{4.35}$$

$$H_6^{(0^+)} = \frac{h_6^{(0^+)}}{mg_0\tilde{g}_1}\Lambda^2 \ . \tag{4.36}$$

For the purposes of this chapter we will not need the inhomogeneous terms, since we only search for states that are defined by the scattering amplitude having a pole for the energy E of the state in question. Therefore, at the energy of the state the inhomogeneous terms are negligible.

The homogeneous terms are the ones that consist of a loop-integral over either an A-, B- or C-amplitude in Fig. 4.2. They are called homogeneous since we treat the scattering equation as a matrix equation $V = M + KV$, where then V is the vector of amplitudes, M is the inhomogeneous part and K is the kernel matrix. The homogeneous parts of the scattering amplitude can be derived to be as in Eqs. (4.37)–(4.45), where we define $A = A^{(A)} + A^{(B)} + A^{(C)}$, $B = B^{(A)} + B^{(B)} + B^{(C)}$ and $C = C^{(A)} + C^{(B)} + C^{(C)}$. First,

the A-amplitudes are written as

$$
iA^{(A)\,\sigma a}_{\quad\chi b}(\mathbf{k},\mathbf{p}) = - ig_1^2 \mathcal{C}^a_{i\sigma'}\mathcal{C}^{a'}_{j\sigma}\int\frac{\mathrm{d}^3q}{(2\pi)^3}\left(q_i+\frac{k_i}{5}\right)\left(k_j+\frac{q_j}{5}\right)
$$
$$
\times\, S_\mathrm{c}\left(E-\frac{k^2}{2m}-\frac{q^2}{2m},\mathbf{k}+\mathbf{q}\right)D\left(E-\frac{q^2}{2m},\mathbf{q}\right)A^{\sigma'a'}_{\chi b}(\mathbf{q},\mathbf{p})
$$
$$
-\,ih_1^{(J^\pi)}\mathcal{C}^\alpha_{a\sigma i}\mathcal{C}^\alpha_{a'\sigma'j}\int\frac{\mathrm{d}^3q}{(2\pi)^3}k_iq_jD\left(E-\frac{q^2}{2m},\mathbf{q}\right)A^{\sigma'a'}_{\chi b}(\mathbf{q},\mathbf{p}) \qquad (4.37)
$$

$$
iA^{(B)\,\sigma a}_{\quad\chi b}(\mathbf{k},\mathbf{p}) = - ig_1\tilde{g}_1 \mathcal{C}^a_{i\sigma'}\mathcal{C}^\tau_{j\sigma}\int\frac{\mathrm{d}^3q}{(2\pi)^3}\left(q_i+\frac{k_i}{5}\right)\left(k_j+\frac{q_j}{5}\right)
$$
$$
\times\, S_\mathrm{c}\left(E-\frac{k^2}{2m}-\frac{q^2}{2m},\mathbf{k}+\mathbf{q}\right)\tilde{D}\left(E-\frac{q^2}{2m},\mathbf{q}\right)B^{\sigma'\tau}_{\chi b}(\mathbf{q},\mathbf{p})
$$
$$
-\,ih_2^{(J^\pi)}\mathcal{C}^\alpha_{a\sigma i}\mathcal{C}^\alpha_{\tau\sigma'j}\int\frac{\mathrm{d}^3q}{(2\pi)^3}k_iq_j\tilde{D}\left(E-\frac{q^2}{2m},\mathbf{q}\right)B^{\sigma'\tau}_{\chi b}(\mathbf{q},\mathbf{p}) \qquad (4.38)
$$

$$
iA^{(C)\,\sigma a}_{\quad\chi b}(\mathbf{k},\mathbf{p}) = - ig_0g_1 \mathcal{C}^a_{i\sigma'}\mathcal{C}^0_{\sigma\sigma'}\int\frac{\mathrm{d}^3q}{(2\pi)^3}\left(q_i+\frac{4k_i}{5}\right)
$$
$$
\times\, S_\mathrm{n}\left(E-\frac{k^2}{2m}-\frac{q^2}{8m},\mathbf{k}+\mathbf{q}\right)B\left(E-\frac{q^2}{8m},\mathbf{q}\right)C_{\chi b}(\mathbf{q},\mathbf{p})
$$
$$
-\,ih_5^{(J^\pi)}\mathcal{C}^\alpha_{a\sigma i}\int\frac{\mathrm{d}^3q}{(2\pi)^3}k_iB\left(E-\frac{q^2}{8m},\mathbf{q}\right)C_{\chi b}(\mathbf{q},\mathbf{p})\,. \qquad (4.39)
$$

For completeness we have written the equations for general total spin and parity J^π, where the Clebsch-Gordan index α can take values according to $\alpha = -J, ..., J$. For the 0^+ channel we have that $\alpha = 0$ and for the 2^+ channel $\alpha = 2$. Note also that we set $h_4, h_5, h_6 = 0$ in the 2^+ channel, since these three-body interaction terms does not exist[1].

---

[1] The relevant three-body interactions that would appear in these diagram parts include the D-wave operator given in Eq. (4.7) and are of higher scaling dimension than 7

Continuing, the B-diagrams are derived as

$$
iB^{(A)\,\sigma\tau}_{\quad\chi b}(\mathbf{k},\mathbf{p}) = - ig_1\tilde{g}_1 \mathcal{C}^\tau_{i\sigma'}\mathcal{C}^{a'}_{j\sigma} \int \frac{\mathrm{d}^3q}{(2\pi)^3} \left(q_i + \frac{k_i}{5}\right)\left(k_j + \frac{q_j}{5}\right)
$$
$$
\times S_\mathrm{c}\left(E - \frac{k^2}{2m} - \frac{q^2}{2m}, \mathbf{k}+\mathbf{q}\right) D\left(E - \frac{q^2}{2m}, \mathbf{q}\right) A^{\sigma'a'}_{\chi b}(\mathbf{q},\mathbf{p})
$$
$$
- ih_2^{(J^\pi)}\mathcal{C}^\alpha_{\tau\sigma i}\mathcal{C}^\alpha_{a'\sigma'j} \int \frac{\mathrm{d}^3q}{(2\pi)^3} k_i q_j D\left(E - \frac{q^2}{2m}, \mathbf{q}\right) A^{\sigma'a'}_{\chi b}(\mathbf{q},\mathbf{p}) \qquad (4.40)
$$

$$
iB^{(B)\,\sigma\tau}_{\quad\chi b}(\mathbf{k},\mathbf{p}) = - i\tilde{g}_1^2 \mathcal{C}^\tau_{i\sigma'}\mathcal{C}^{\tau'}_{j\sigma} \int \frac{\mathrm{d}^3q}{(2\pi)^3} \left(q_i + \frac{k_i}{5}\right)\left(k_j + \frac{q_j}{5}\right)
$$
$$
\times S_\mathrm{c}\left(E - \frac{k^2}{2m} - \frac{q^2}{2m}, \mathbf{k}+\mathbf{q}\right) \tilde{D}\left(E - \frac{q^2}{2m}, \mathbf{q}\right) B^{\sigma'\tau'}_{\chi b}(\mathbf{q},\mathbf{p})
$$
$$
- ih_3^{(J^\pi)}\mathcal{C}^\alpha_{\tau\sigma i}\mathcal{C}^\alpha_{\tau'\sigma'j} \int \frac{\mathrm{d}^3q}{(2\pi)^3} k_i q_j \tilde{D}\left(E - \frac{q^2}{2m}, \mathbf{q}\right) B^{\sigma'\tau'}_{\chi b}(\mathbf{q},\mathbf{p}) \qquad (4.41)
$$

$$
iB^{(C)\,\sigma\tau}_{\quad\chi b}(\mathbf{k},\mathbf{p}) = - ig_0\tilde{g}_1 \mathcal{C}^\tau_{i\sigma'}\mathcal{C}^0_{\sigma\sigma'} \int \frac{\mathrm{d}^3q}{(2\pi)^3} \left(q_i + \frac{4k_i}{5}\right)
$$
$$
\times S_\mathrm{n}\left(E - \frac{k^2}{2m} - \frac{q^2}{8m}, \mathbf{k}+\mathbf{q}\right) B\left(E - \frac{q^2}{8m}, \mathbf{q}\right) C_{\chi b}(\mathbf{q},\mathbf{p})
$$
$$
- ih_6^{(J^\pi)}\mathcal{C}^\alpha_{\tau\sigma i} \int \frac{\mathrm{d}^3q}{(2\pi)^3} k_i B\left(E - \frac{q^2}{8m}, \mathbf{q}\right) C_{\chi b}(\mathbf{q},\mathbf{p}) . \qquad (4.42)
$$

Note that if we consider a field theory without the $1/2^-$ channel all of the B-diagrams are identically zero. Further, note that we set $h_6^{(2^+)} = 0$. Finally, the C-diagrams are given by

$$
iC^{(A)}_{\quad\chi b}(\mathbf{k},\mathbf{p}) = - 2ig_0 g_1 \mathcal{C}^a_{i\sigma'}\mathcal{C}^0_{\sigma\sigma'} \int \frac{\mathrm{d}^3q}{(2\pi)^3} \left(k_i + \frac{4q_i}{5}\right)
$$
$$
\times S_\mathrm{n}\left(E - \frac{k^2}{2m} - \frac{q^2}{8m}, \mathbf{k}+\mathbf{q}\right) D\left(E - \frac{q^2}{2m}, \mathbf{q}\right) A^{\sigma'a'}_{\chi b}(\mathbf{q},\mathbf{p})
$$
$$
- ih_5^{(J^\pi)}\mathcal{C}^\alpha_{a\sigma i} \int \frac{\mathrm{d}^3q}{(2\pi)^3} q_i D\left(E - \frac{q^2}{2m}, \mathbf{q}\right) A^{\sigma'a'}_{\chi b}(\mathbf{q},\mathbf{p}) \qquad (4.43)
$$

$$
iC^{(B)}_{\quad\chi b}(\mathbf{k},\mathbf{p}) = - 2ig_0\tilde{g}_1 \mathcal{C}^\tau_{i\sigma'}\mathcal{C}^0_{\sigma\sigma'} \int \frac{\mathrm{d}^3q}{(2\pi)^3} \left(k_i + \frac{4q_i}{5}\right)
$$
$$
\times S_\mathrm{n}\left(E - \frac{k^2}{2m} - \frac{q^2}{8m}, \mathbf{k}+\mathbf{q}\right) \tilde{D}\left(E - \frac{q^2}{2m}, \mathbf{q}\right) B^{\sigma'\tau}_{\chi b}(\mathbf{q},\mathbf{p})
$$
$$
- ih_6^{(J^\pi)}\mathcal{C}^\alpha_{\tau\sigma i} \int \frac{\mathrm{d}^3q}{(2\pi)^3} q_i \tilde{D}\left(E - \frac{q^2}{2m}, \mathbf{q}\right) B^{\sigma'\tau}_{\chi b}(\mathbf{q},\mathbf{p}) \qquad (4.44)
$$

$$
iC^{(C)}_{\quad\chi b}(\mathbf{k},\mathbf{p}) = - 2ih_4^{(J^\pi)} \int \frac{\mathrm{d}^3q}{(2\pi)^3} B\left(E - \frac{q^2}{8m}, \mathbf{q}\right) C_{\chi b}(\mathbf{q},\mathbf{p}) . \qquad (4.45)
$$

Of particular interest here is that the $C^{(C)}$ part is identically zero in the 2^+ channel, since we set $h_4^{(2^+)} = 0$.

The diagrams Eqs. (4.37)–(4.45) are written for general total spin and parity. If these diagrams are to be used for the calculation of an actual physical state we must first project the equations onto the J^π of the state under consideration. For example, if we are interested in the 0^+ channel, then we note that the ^{5}He+neutron legs must be in a relative P-wave. We can check this as

$$\underbrace{3/2^-}_{^5\text{He}(3/2^-)} \otimes \underbrace{1/2^+}_{\text{neutron}} \otimes \underbrace{1^-}_{\text{P−wave}} = \underbrace{\left(1^- \oplus 2^-\right)}_{\text{Spin } S} \otimes 1^-$$
$$= 0^+ \oplus 1^+ \oplus 2^+ \oplus 1^+ \oplus 2^+ \oplus 3^+ \qquad (4.46)$$

and

$$\underbrace{1/2^-}_{^5\text{He}(1/2^-)} \otimes \underbrace{1/2^+}_{\text{neutron}} \otimes \underbrace{1^-}_{\text{P−wave}} = \underbrace{\left(0^- \oplus 1^-\right)}_{\text{Spin } S} \otimes 1^-$$
$$= 1^+ \oplus 0^+ \oplus 1^+ \oplus 2^+ \ . \qquad (4.47)$$

Note also that a 0^+ can only be achieved through a spin $S = 1^-$. The same exercise but with another angular momentum can not give a 0^+. Similarly, the neutron-neutron legs must be in a relative S-wave to be able to result in a 0^+.

Projecting onto total spin and parity 0^+ we arrive at the integral equations (4.48)–(4.56), that were presented in Paper E.

$$iA^{(A)}_{(0+)}(k,p) = ig_1^2 \frac{2m}{3\pi^2} \int \mathrm{d}q\, q^2 K^{(AA)}_{(0+)}(k,q) D\left(E - \frac{3q^2}{5m}, 0\right) A_{(0+)}(q,p) \qquad (4.48)$$

$$iA^{(B)}_{(0+)}(k,p) = ig_1\tilde{g}_1 \frac{2m}{3\pi^2} \int \mathrm{d}q\, q^2 K^{(AB)}_{(0+)}(k,q) \tilde{D}\left(E - \frac{3q^2}{5m}, 0\right) B_{(0+)}(q,p) \qquad (4.49)$$

$$iA^{(C)}_{(0+)}(k,p) = ig_1 g_0 \frac{m}{\sqrt{6}\pi^2} \int \mathrm{d}q\, q^2 K^{(AC)}_{(0+)}(k,q) B\left(E - \frac{3q^2}{8m}, 0\right) C_{(0+)}(q,p) \qquad (4.50)$$

$$iB^{(A)}_{(0+)}(k,p) = ig_1\tilde{g}_1 \frac{2m}{3\pi^2} \int \mathrm{d}q\, q^2 K^{(BA)}_{(0+)}(k,q) D\left(E - \frac{3q^2}{5m}, 0\right) A_{(0+)}(q,p) \qquad (4.51)$$

$$iB^{(B)}_{(0+)}(k,p) = i\tilde{g}_1^2 \frac{2m}{3\pi^2} \int \mathrm{d}q\, q^2 K^{(BB)}_{(0+)}(k,q) \tilde{D}\left(E - \frac{3q^2}{5m}, 0\right) B_{(0+)}(q,p) \qquad (4.52)$$

$$iB^{(C)}_{(0+)}(k,p) = i\tilde{g}_1 g_0 \frac{m}{\sqrt{6}\pi^2} \int \mathrm{d}q\, q^2 K^{(BC)}_{(0+)}(k,q) B\left(E - \frac{3q^2}{8m}, 0\right) C_{(0+)}(q,p) \qquad (4.53)$$

$$iC^{(A)}_{(0+)}(k,p) = 2ig_0 g_1 \frac{m}{\sqrt{6}\pi^2} \int \mathrm{d}q\, q^2 K^{(CA)}_{(0+)}(k,q) D\left(E - \frac{3q^2}{5m}, 0\right) A_{(0+)}(q,p) \qquad (4.54)$$

$$iC^{(B)}_{(0+)}(k,p) = 2ig_0 \tilde{g}_1 \frac{m}{\sqrt{6}\pi^2} \int \mathrm{d}q\, q^2 K^{(CB)}_{(0+)}(k,q) \tilde{D}\left(E - \frac{3q^2}{5m}, 0\right) B_{(0+)}(q,p) \qquad (4.55)$$

$$iC^{(C)}_{(0+)}(k,p) = 2ig_0^2 \frac{m}{2\pi^2} \int \mathrm{d}q\, q^2 K^{(CC)}_{(0+)}(k,q) B\left(E - \frac{3q^2}{8m}\right) C_{(0+)}(q,p) \qquad (4.56)$$

To solve this coupled integral equation, which is defined by the scattering diagrams, we may search for zeros to the eigenvalue equation

$$\det\left(\mathbf{1} - K\right) = 0 \ . \qquad (4.57)$$
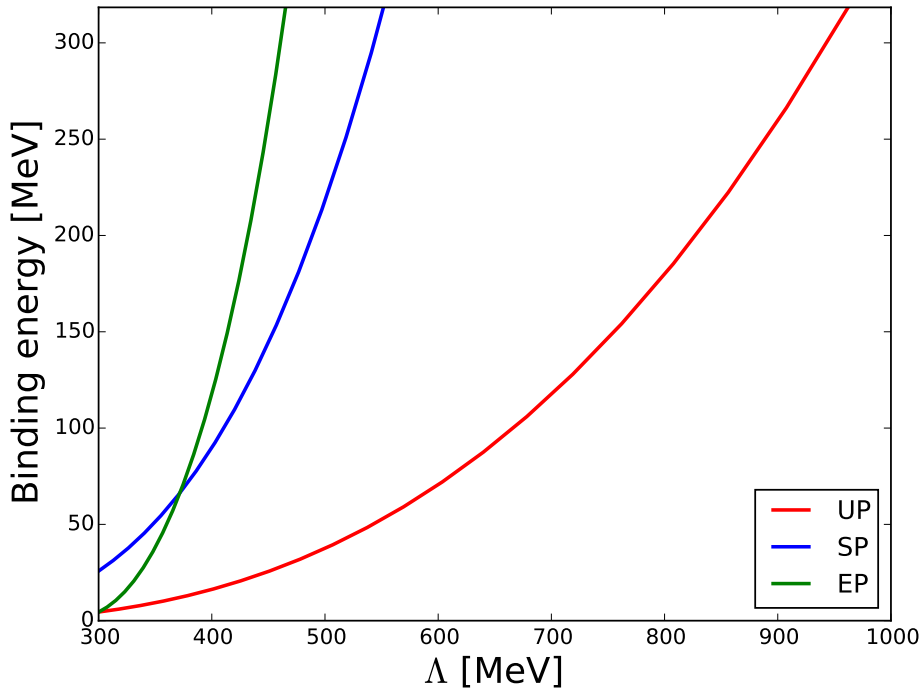
Figure 4.3: The ^{6}He binding energy as a function of the cutoff Λ. Only the dineutron and the $3/2^-$ channels are included. All the three-body interactions have been set to zero.

In doing this numerically we have replaced the momentum spans, $[0, \Lambda]$, with a Legendre mesh and absorbed the g-parameters into the definitions of the A-, B- and C-amplitudes.

4.4   Renormalization of bound states

In this section we will discuss the evaluation and renormalization of the 0^+ integral equations for negative energy, $E = -B$.

In Paper E we presented three different types of results. First, how the bound-state energy depends on the cutoff Λ when the three-body interactions are all set to zero. We do this by searching for energy solutions to the eigenvalue equation (4.57) for different cutoffs. The resulting $B - \Lambda$ dependence can then be presented graphically. Note that if the bound state energy is independent of the cutoff, then the field theory is already renormalized and no three-body interactions need to be included. Second, we present results for the running of the three-body parameters. These are obtained by fixing the bound-state energy and searching for H-solutions to the eigenvalue equation, for different cutoffs. With H-solutions we mean that we let one (or a set) of the three-body interactions
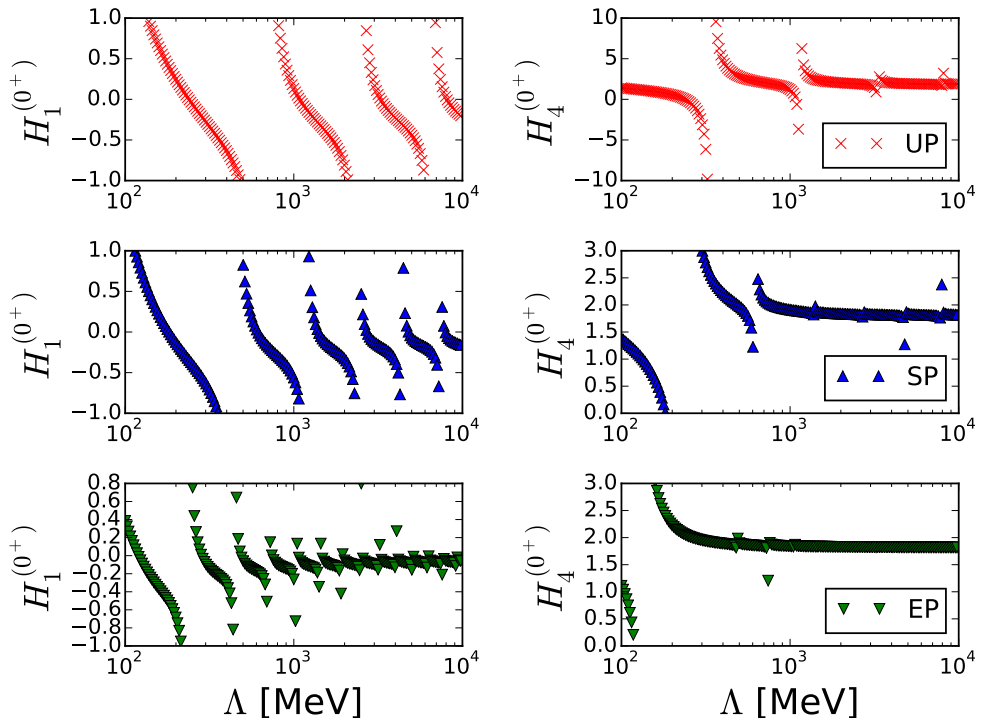
Figure 4.4: Limit cycles for the three different prescriptions, using either the $H_1^{(0^+)}$ or $H_4^{(0^+)}$ three-body interaction. Only the dineutron and the $3/2^-$ channels are included. The three-body parameter was fixed to the bound state energy $B = 1$ MeV.

be non-zero and we find the value of the related three-body interaction parameter when the determinant is zero for a fixed binding energy. The resulting $H - \Lambda$ plot is typically log-periodic. Third, we fix a three-body interaction such that the integral equations have a bound state solution. Then we use this three-body interaction to search for deep bound states. This procedure is then repeated for many different cutoffs, but with the same first bound state, to produce a convergence plot of the deep bound states. If the deep bound states do not converge with increasing cutoffs, then the system is not properly renormalized by the three-body interaction under consideration. It should be mentioned that these deep-bound states are of course not physical, or true, states of ^{6}He. However, they are well-defined observables within the field theory and as such a renormalization analysis of these states provide indications of whether the field theory is properly renormalized or not.

We begin by analyzing a field theory with only the dineutron and ^{5}He($3/2^-$) channels included, as was done in [12] and [13]. The $B - \Lambda$ result is shown in Fig. 4.3. The resulting cutoff dependence is clearly different for the three two-body prescriptions that have been
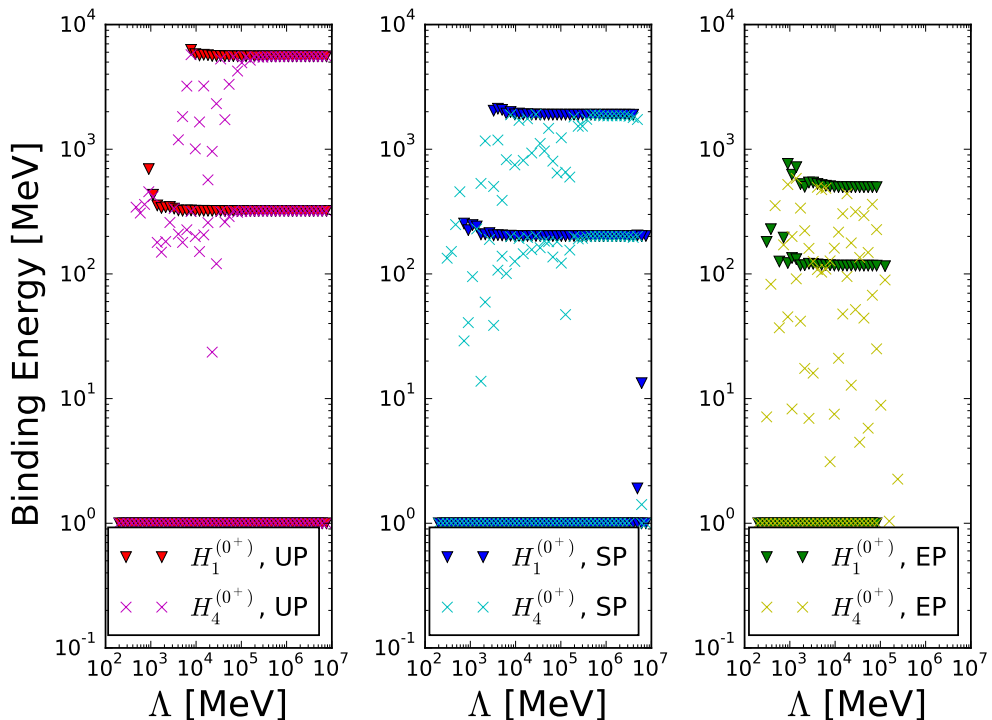
Figure 4.5: Convergence of deep bound states for the three different prescriptions, using either the $H_1^{(0^+)}$ or $H_4^{(0^+)}$ three-body interaction. Only the dineutron and the $3/2^-$ channels are included. The three-body parameter was fixed to the bound state energy $B = 1$ MeV.

used. However, the only conclusion that can be drawn from this figure is the fact that a three-body interaction is needed at LO to renormalize the system.

Continuing with the $H - \Lambda$ plot, which is shown in Fig. 4.4, we can clearly see the log-periodic limit cycles for the different prescriptions and the diagonal three-body interaction. In particular, note that the period differs for the three prescriptions. The period is shortest for the EP, indicating that additional bound states appear with high frequency in Λ. This is also connected to the rather steep rise of the bound-state energy in the $B - \Lambda$ plot for the EP. This should make it harder to numerically use the EP, since the spectrum might be messier than for the other prescriptions. We also tried to renormalize the field theory using the off-diagonal three-body interaction, $H_5^{(0^+)}$, but this was not possible since no bound-state solutions to the integral equations were found.

Finally, searching for deep bound states we generate the convergence plots in Fig. 4.5. The first thing to note is that for sufficiently large cutoff the deep bound states have converged, which is a good indicator that the field theory is properly renormalized. This
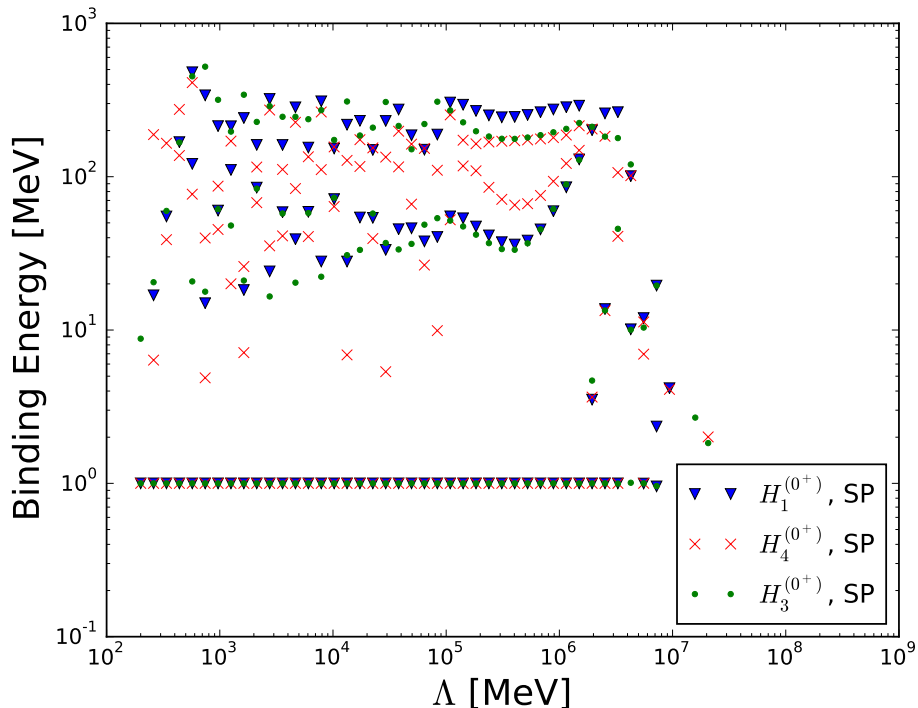
Figure 4.6: Non-convergence of deep bound states for a field theory where the $1/2^-$ channel is also included. Either the $H_1^{(0^+)}$, $H_4^{(0^+)}$ or $H_3^{(0^+)}$ three-body interaction is used. The three-body parameter was fixed to the bound state energy $B = 1$ MeV.

finding is true for both of the diagonal three-body interactions, except for the $H_4^{(0^+)}$ in the EP where the deep-states have yet to converge. The second important point is that both three-body interactions renormalize the deep-bound states to the same energy position. This result indicates that physical observables are independent on the choice between the two diagonal three-body interactions. As can be seen, however, the deep bound states converge much faster when the $H_1^{(0^+)}$ three-body interaction is used. These facts then motivate us to primarily use the simplest interaction, $H_1^{(0^+)}$, and they validate the choice of three-body interaction in Refs. [12] and [13]. The third important observation to note is that the three different prescriptions give differing spectra for the deep bound states. This means that the differences in the low-momentum physics of the three prescriptions can have large effects on observables.

We now turn to the treatment of a field theory where not only the ^{5}He$(3/2^-)$ and dineutron channels are included, but also the ^{5}He$(1/2^-)$ channel. We refer to this as the full field theory. In Fig. 4.6 we show a plot of how the deep-bound states depend

on the cutoff parameter Λ in the SP, where we have fixed one three-body interaction at a time to the bound-state energy $B = 1$ MeV. It is clear that none of the three-body interactions $H_1^{(0^+)}$, $H_4^{(0^+)}$ or $H_3^{(0^+)}$ can renormalize the deep bound states properly, since the energy positions of the deep-bound states do not converge. If we instead use one of the off-diagonal interactions $H_2^{(0^+)}$, $H_5^{(0^+)}$ or $H_6^{(0^+)}$ no bound-state solutions are found. As such, none of the dimension-7 three-body operators can by itself renormalize the full field theory. Note that we do not suggest that higher-dimension operators are needed. However, the conclusion of Paper E is that one most likely need to fix two different three-body interactions simultaneously to renormalize the deep bound states of the full field theory properly. Another explanation to the non-renormalization of the deep bound states could be that larger cutoffs are needed. Unfortunately we have been limited to $\Lambda \lesssim 2 \times 10^6$ MeV due to numerics. The theory might still be renormalizable at even higher cutoffs.

One can also perform a renormalization analysis using the EP. However, since the EP is much harder to renormalize properly than the SP we do not expect any improvements regarding the renormalization of the deep bound states. The numerical calculations that we did perform on the full field theory using the EP agrees with this conclusion. We have not used the UP for the full field theory.

4.5   Non-renormalization of resonant states

In this section we will analyze the renormalization of resonant states in the 0^+ channel of ^{6}He. Since there are renormalization issues in the bound-state sector for the full field theory, that is the field theory where the ^{5}He$(1/2^-)$ channel is also included, we will here focus on a field theory where only the dineutron and the ^{5}He$(3/2^-)$ channels are included.

We fixed the three-body interaction $H_1^{(0^+)}$ to the bound-state energy $B = 1$ MeV and performed searches for resonant states by solving the integral equations (4.48)–(4.56) for complex energy $E = E_{\mathrm{R}} + iE_{\mathrm{I}}$. In solving the integral equations we scanned the complex plane for a minimum of the absolute value of the determinant, $|\det(\mathbf{1} - K)|$, until a zero was found. We tried all three prescriptions (UP, SP and EP) to handle the non-physical two-body pole. For the SP and UP no resonances were found. The results for the EP are shown in Fig. 4.7, where the resonance position is given for cutoffs up to 10^5 MeV. For larger cutoffs the numerics began to break down. Note that there are no signs of convergence for the resonance position in Fig. 4.7. This result either indicates that one three-body interaction is not enough to renormalize the resonance, or that the calculation needs to be performed at a higher cutoff.

Alternatively, one can in principle have a situation where the resonance can be renormalized, but not simultaneously with the bound state. This scenario can, for example, be probed by searching for the resonance for different values of the three-body interaction $H_1^{(0^+)}$ and then compare the span of obtained complex energies for different cutoffs. If then the resonance is properly renormalized one would expect the Λ-dependent spans to converge as Λ increases, that is the set of resulting complex energies should converge to a limiting set. Note however that we do not demand that individual complex

()
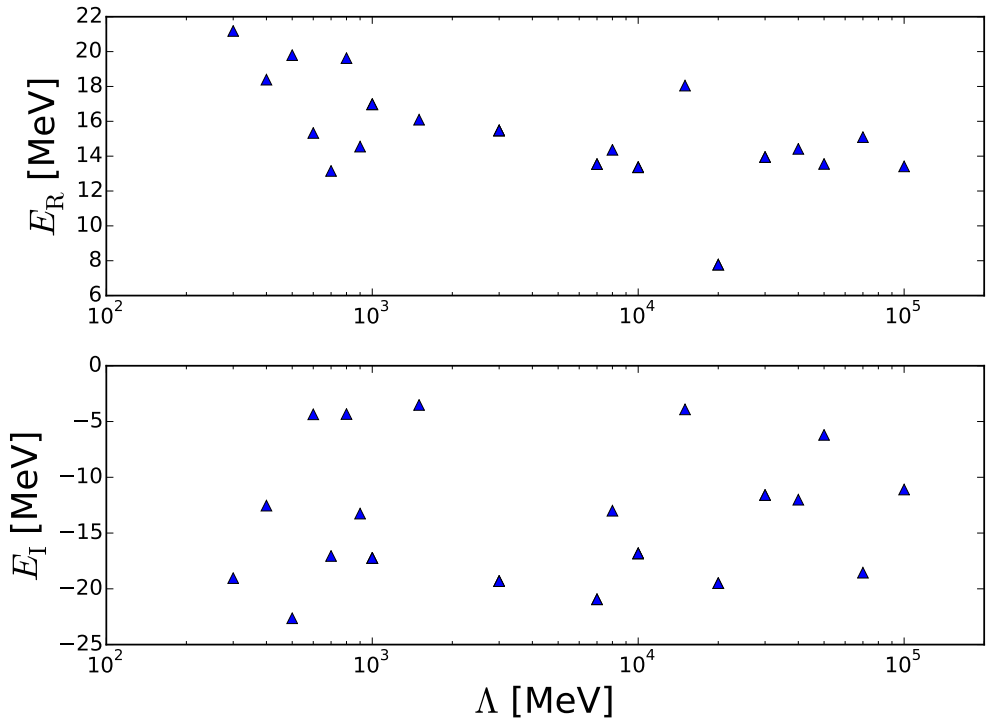
Figure 4.7: The cutoff dependence of the 0^+ resonant state. The $H_1^{(0^+)}$ three body parameter has been fixed to the bound state at $B = 1$ MeV. Note that the result does not seem to converge for cutoffs $\Lambda < 10^5$ MeV.

energies in these spans converge for fixed $H_1^{(0^+)}$. The result of this analysis is shown in the left panel of Fig. 4.8. As can be seen, the spans do not converge for $\Lambda \leq 10^5$ MeV. The conclusion is then that only one three-body interaction can not renormalize the system, at least not for the cutoffs $\Lambda \lesssim 10^5$ MeV that we are restricted to.

As a final attempt, we present an analysis where we fix two three-body interactions, the $H_1^{(0^+)}$ and $H_4^{(0^+)}$, to the bound state energy $B = 1$ MeV. This approach also results in Λ-dependent spans of complex energies when we search for the resonant state. We show these results in the right panel of Fig. 4.8. It is hard to tell with certainty whether these spans are converging or not and this suggests that we need to go to higher cutoffs to be able to draw any final conclusions. However, this result indeed looks much better compared to the field theory with only one three-body interaction included, shown in the left panel. As such we might have a situation where two three-body interactions are needed to renormalize the resonant 0^+ state and that cutoffs $\Lambda \gg 10^5$ MeV are needed to achieve convergence.
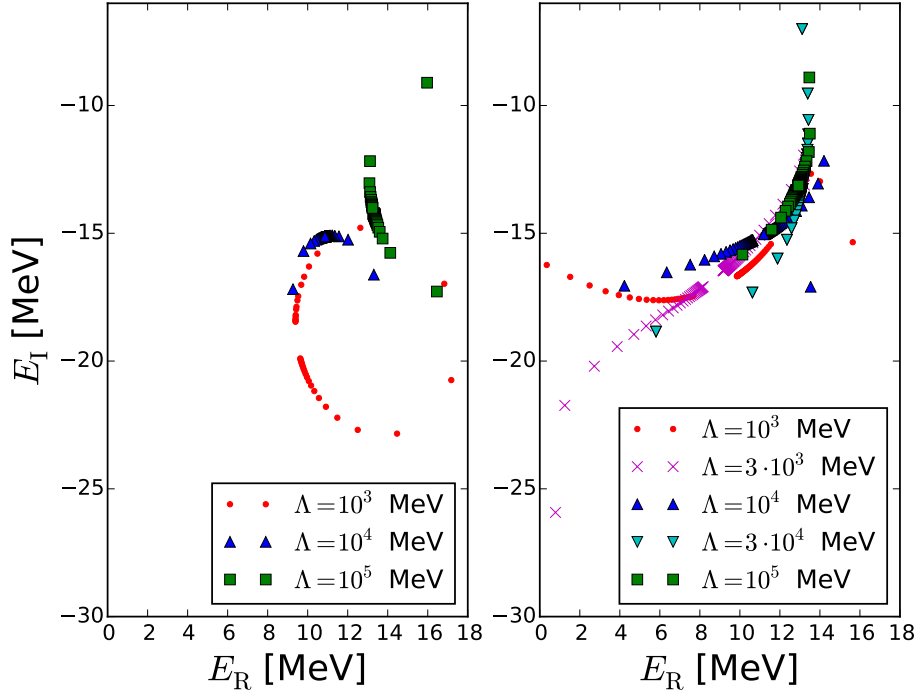
Figure 4.8: The cutoff dependence of the spans of the 0^+ resonant state. In the left panel the $H_1^{(0^+)}$ three body parameter is varied to generate the complex energy spans for the resonant state. In the right panel the $H_1^{(0^+)}$ and $H_1^{(0^+)}$ three body parameters are fixed to the bound state at $B = 1$ MeV and they then also generate complex energy spans for the resonant state.

5 Summary of papers

In Paper A we derived a formalism for the treatment of S-wave one-proton halo nuclei in EFT. We renormalized the interaction by matching to the ERE and continued by calculating the charge radius and radiative capture S-factor for the one-proton halo state $^{17}\text{F}^*$. Note that in the derivation of the radiative capture cross section we have a relative sign error between the core-photon and proton-photon diagrams. This error translates into a substantial error in the presented S-factor result, see Fig. 5 of Paper A. In Paper C we extended the formalism to include the effective-range correction and we found that the effective range is fine-tuned and that the system has a very large ANC. We also included an N^4LO electromagnetic operator that was used to produce an accurate fit to the measured radiative capture data. From this fit we could extract the threshold value of the S-factor and the ANC, which compares well with previous extractions. We also presented a result for the charge radius of $^{17}\text{F}^*$, using the extracted ANC as input. However, the uncertainties due to the EFT error was very large since a short-range operator is promoted due to the fine-tuning of the effective range.

In Paper B, the formalism was extended to include one-proton halo nuclei bound due to a P-wave proton-core interaction. For P-wave systems the effective range is needed already at LO to renormalize the interaction. This feature makes it harder to make predictions, since two parameters need to be fixed at LO. We circumvented this by matching to previously extracted ANCs, such that there was no need to extract the individual ERE parameters. The formalism was applied to study the ^8B proton halo, where we included both the ground and excited state of the ^7Be core. We focused on the calculation of the correlation between the threshold S-factor and the charge radius. The potency of such a correlation would be that it could constrain the S-factor through a planned future measurement of the charge radius.

In Paper D we present the heavy-core power counting. In this new power-counting scheme the mass number of the core nucleus is taken into account, which alters the order at which certain operators appear if the core is sufficiently heavy. We also derive how the finite-size contributions of the constituent particles enter the charge radius result. In a sense, the results of Paper D have been implicit in our previous conclusions regarding the charge radius in both Paper B and C. In Paper A we suggested that the calculated point-particle charge radius could be added to the finite-size contributions in quadrature, which seemed logical at the time since we had yet to discover that the system was very fine-tuned. The results in Paper D that concern one-nucleon halo charge radii are two-fold: First, we find that the point-particle contribution is demoted to higher order for one-neutron halos while it is unchanged for one-proton halos. Second, that the finite-size contributions enter at a higher order than the short-range operator for P-wave one-nucleon halos. This second point implies that the charge radius result of Paper B, for ^8B, can not be seen as being relative to the charge radius of the ^7Be core. There might also be other implications due to the heavy-core power counting presented in Paper D, for example there might be changes to how one treats heavy-core propagators in many-body calculations.

Paper E is somewhat separate from the other four papers since it concerns a three-body system, namely the two-neutron halo ^6He. As such there are no Coulomb interactions that

could complicate matters and since we only consider the renormalization of bound states there are actually no electromagnetic operators at all present. Instead, the complications arise due to the presence of many three-body interactions at the lowest scaling dimension. There is also an issue with the two-body sector of the field theory, where there are non-physical poles that need to be removed in some way. We discuss and analyze three such removal precriptions. Our finding is that only one three-body interaction is needed to renormalize the bound system when the dineutron and $^5\text{He}(3/2^-)$ channels are included. However, in the presence of the additional $^5\text{He}(1/2^-)$ field we found that the field theory was not renormalizable by only one three-body interaction.

6 Conclusion and outlook

In this thesis we have introduced Cluster EFT formalism for (i) one-proton halo states, (ii) three-body systems without Coulomb, and (iii) halo states with a heavy core. The proton-halo formalism was used to calculate the charge form factors and radiative capture S-factors for the one-proton halo states $^{17}\text{F}^*$ and ^8B. The three-body formalism was developed and used to analyze the renormalization of bound and resonant states of the two-neutron halo ^6He. Finally, we have discussed a new power counting for systems with a heavy core nucleus and derived the finite-size contributions to charge radii of one-nucleon halos.

The one-proton halo formalism was applied to the halo state $^{17}\text{F}^*(1/2^+)$, seen as an $^{16}\text{O}(0^+)$ core and a proton, bound due to an S-wave interaction, with an unnaturally large scattering length. In this system we noted that the Coulomb momentum is much larger than the binding momentum, $k_\text{C} \gg \gamma_0$, and that this large k_C/γ_0 ratio is at the core of many of the problems that we encountered. First, the ANC of the $1/2^+$ ^{16}O-proton channel is very large and this must be reflected by the wavefunction renormalization $\mathcal{Z} \sim 1/(1 - 3k_\text{C}r_0)$. As a consequence, the effective range is fine-tuned to be close to $1/(3k_\text{C})$. This implies that at LO, without the effective range included, there is no way to achieve a large ANC and as such the LO results will be severly off. Second, since $3k_\text{C}r_0 \sim 1$ we have a promotion of the undetermined short-range operator for the charge radius to N^2LO. This restricts us to NLO predictions for the charge radius calculation. Finite-size contributions can not be included since these enter at N^2LO together with the short-range operator. We also considered the radiative capture reaction $^{16}\text{O}(p, \gamma)^{17}\text{F}^*$ up to N^5LO and fitted the Cluster EFT model to measured data. Compared to the rather disappointing findings for the charge radius, the radiative capture result was clearly encouraging. First, since the S-factor was free of short-range contributions up to N^3LO, second, since the N^5LO result compares very well to the experimental data and, third, since we see a good order-by-order convergence.

We considered the one-proton halo $^8\text{B}(2^+)$, for which the ^7Be-proton interaction is of P-wave nature. This P-wave nature complicates the renormalization of the interaction by demanding that the effective range is included already at LO. In treating this system we included both the $3/2^-$ ground state and the $1/2^-$ excited state of ^7Be. The excited state only affects the radiative capture cross section if initial-wave scattering is included, which was not done in this thesis. However, it does affect the charge radius result for ^8B by making it about 10% larger. The inclusion of the excited state into the field theory also reduces the EFT error, since it increases the break-down scale of the theory and therefore makes the expansion parameter smaller. In considering both the charge radius and the astrophysical S-factor for ^8B we proposed to use a future measurement of the charge radius to constrain the S-factor. This proposal was shown as a LO correlation between these two observables. However, the error related to the charge radius calculation at LO is probably too large for the LO correlation to be of practical use. Moreover, due to the appearance of a short-range operator at NLO for the P-wave charge radius the correlation presently only exists at LO. A possible way around the large LO theoretical uncertainties is to include more physics into the field theory, thereby reducing the EFT

expansion parameter and the corresponding error. Note, however, that the uncertainty on the threshold S-factor is already very small. This is since the higher-order photon operators enter with additional powers of the photon momentum that scales as $\omega \sim k_{lo}^2$ at threshold. At higher c.m. energies the uncertainty on the S-factor increases rapidly.

For the ^{6}He nucleus we derived the integral equations for a field theory where the 0^+ dineutron and both the $3/2^-$ and $1/2^-$ ^{5}He channels are included. We analyzed the six three-body interactions that are of lowest scaling dimension and we discussed three different prescriptions of how to handle the unphysical poles of the P-wave dicluster propagators. When we solved the 0^+ integral equations we found that the theory could not be properly renormalized by only one three-body interaction if all three channels were included. Instead, using the simpler field theory with only the dineutron and the ^{5}He$(3/2^-)$ channels included we showed proper renormalization for deep bound states in the 0^+ using only one three-body interaction. But even for this simpler field theory we found that the 0^+ resonant states could not be renormalized with only one three-body interaction. This finding would imply a restriction on the predictability of the Cluster EFT treatment of three-body systems as many three-body interactions would need to be fixed for predictions to be made. However, one should mention the possibiliy that the theory is actually renormalized, but that we were unable to use large enough cutoffs. As it was, we were restricted to cutoffs $\Lambda < 10^7$ MeV.

Cluster EFT offers a systematic approach to make model-independent predictions of low-energy observables. However, it is restricted by appearances of short-range operators at rather low orders. With the heavy-core power counting that we have developed these restrictions are even enhanced for some systems and observables. For example, for one-neutron halos where the core is much heavier than the neutron the point-particle result for the charge radius is demoted from leading to sub-leading order, since the core recoil due to the photon interaction is very small. Instead, in the case of an S-wave system, the LO charge radius is given by the finite-size contributions of the constituents. For a P-wave one-neutron halo the heavy-core version of Cluster EFT is non-predictive at LO, since the LO charge radius is given by the undetermined short-range operator. Note however that not all systems are made less predictive in the heavy-core power counting. For proton halos there are no issues for the charge radius results due to the core being heavy. This is due to the fact that the photon also couples to the proton field, which has a larger recoil than that of the core field. One should mention that there are other important aspects of the heavy-core power counting. These regard the fact that the propagator of the heavy-core field is static at LO and the hope is that this might lead to simplifications in many-body systems.

There are several natural extensions to the work that has been presented in this thesis. A relatively straightforward outlook is to simply consider more states or systems in the one-proton halo formalism. For example, one can include the $5/2^+$ ground state of ^{17}F into the ^{16}O+proton field theory. This state is bound due to a D-wave interaction, which of course increases the complexity, but the hope is that the ground state is less fine-tuned than the excited state. One can see indications of this since the binding momentum of the ground state is ~ 30 MeV, which is still less than the Coulomb momentum but at least about the same order. When including this state, a more complete picture of the radiative capture cross section can be given. Other interesting systems to consider would

be ^{7}Be and ^{7}Li, seen as an α-particle plus a ^{3}He or triton, respectively. Such systems can be seen as halo-like and should be ideal testing grounds for the Cluster EFT formalism.

In the discussion on the ^{8}B charge radius we mentioned that one could include more physics into the field theory to be able to reduce the EFT uncertainty. One such piece of additional physics could be to include three-body dynamics, that is $\alpha+^3$He+proton. In such a field theory the uncertainty for the LO charge radius would be reduced significantly. However, a field theory consisting of three interacting charged particles is a non-trivial construction since one would need to derive three-body Coulomb propagators. On the other hand, if we had this formalism there would be some additional interesting systems to consider, for example the Hoyle state in ^{12}C or the ^{17}Ne two-proton halo. A simpler extension of the proton-halo formalism would be to treat three-body systems with one uncharged particle, for example ^{8}Li seen as $\alpha+^3$H+neutron. In such a field theory one only needs two-body Coulomb Green's functions. The ^{8}Li halo nucleus can also be considered to be of some interest, since it is the mirror state of ^{8}B and one should be able to calculate the charge radius to a rather high accuracy using such a three-body model.

Our effort towards the calculations of resonant states of ^{6}He has yet to produce renormalized and accurate results in the 0^+ channel. However, the situation might be better in other channels. For example in the 2^+ channel we showed that there are fewer three-body interactions at the lowest scaling dimension. However, while there is a bound 0^+ state, one should note that there is no such bound state in the 2^+ channel to fix any three-body interaction to. Instead one would, for example, have to fix one three-body interaction to the energy position and then predict the width of the resonance, assuming then that the field theory is renormalized by only one three-body interaction. This is a restriction, but a necessary one. In fact, the most desired outlook of our work on three-body resonances is towards a prediction of the width of the halo-like resonant state ^{26}O(0^+) and there we would need to fix the three-body interaction in the same fashion as for the 2^+ state. Note however that a field theory for ^{26}O will need to contain resonant D-wave ^{24}O+neutron channels, which may be a complication.

For the heavy-core power counting the main outlooks are to consider the heavy-core effect on additional observables, such as radiative capture, and to apply it to a three-body system with a heavy core. Further, a speculative idea is to consider the Born-Oppenheimer approximation from a field theory perspective and to derive higher-order corrections that can be applied systematically. If this is possible, it could be of great interest for both nuclear physics and computational chemistry.

In a broader perspective, Cluster EFT is a framework to make model-independent calculations of nuclear physics systems. However, it is dependent on the availability of cluster-nucleon and cluster-cluster data. Presently there are huge amounts of data for the nucleon-nucleon sector, which is the standard input for the Chiral EFT, while cluster data is less common. The hope and expectation for the future is that more cluster data will become available and that this data can then be used to fix the parameters of a particular Cluster EFT. Compared to the Chiral EFT, which has 16 parameters to be fitted at N^{2}LO, Cluster EFT is relatively mild with just a few undetermined short-range parameters. Therefore, Cluster EFT has potentially a very bright future.

References

[1] L. Platter, H.-W. Hammer, and U.-G. Meissner. On the correlation between the binding energies of the triton and the alpha-particle. *Phys. Lett.* **B607** (2005), 254–258. DOI: 10.1016/j.physletb.2004.12.068. arXiv: nucl-th/0409040 [nucl-th].

[2] I. Tanihata et al. Measurements of Interaction Cross-Sections and Nuclear Radii in the Light p Shell Region. *Phys. Rev. Lett.* **55** (1985), 2676–2679. DOI: 10.1103/PhysRevLett.55.2676.

[3] P. Hansen and B. Jonson. The Neutron halo of extremely neutron-rich nuclei. *Europhys. Lett.* **4** (1987), 409–414. DOI: 10.1209/0295-5075/4/4/005.

[4] P. Hansen, A. Jensen, and B. Jonson. Nuclear halos. *Ann. Rev. Nucl. Part. Sci.* **45** (1995), 591–634. DOI: 10.1146/annurev.ns.45.120195.003111.

[5] S. Weinberg. Phenomenological Lagrangians. *Physica* **A96** (1979), 327–340. DOI: 10.1016/0378-4371(79)90223-1.

[6] D. B. Kaplan. "Effective field theories". *Beyond the standard model 5. Proceedings, 5th Conference, Balholm, Norway, April 29-May 4, 1997*. 1995. arXiv: nucl-th/9506035 [nucl-th].

[7] E. Epelbaum, H.-W. Hammer, and U.-G. Meissner. Modern Theory of Nuclear Forces. *Rev. Mod. Phys.* **81** (2009), 1773–1825. DOI: 10.1103/RevModPhys.81.1773. arXiv: 0811.1338 [nucl-th].

[8] J. F. Donoghue. General relativity as an effective field theory: The leading quantum corrections. *Phys. Rev.* **D50** (1994), 3874–3888. DOI: 10.1103/PhysRevD.50.3874. arXiv: gr-qc/9405057 [gr-qc].

[9] S. Weinberg. Effective field theory, past and future. *Int. J. Mod. Phys.* **A31**.06 (2016), 1630007. DOI: 10.1142/S0217751X16300076.

[10] C. Bertulani, H.-W. Hammer, and U. van Kolck. Effective field theory for halo nuclei. *Nucl. Phys. A* **712** (2002), 37–58. DOI: 10.1016/S0375-9474(02)01270-8.

[11] P. F. Bedaque, H.-W. Hammer, and U. van Kolck. Narrow resonances in effective field theory. *Phys. Lett.* **B569** (2003), 159–167. DOI: 10.1016/j.physletb.2003.07.049.

[12] J. Rotureau and U. van Kolck. Effective Field Theory and the Gamow Shell Model: The ^{6}He Halo Nucleus. *Few Body Syst.* **54** (2013), 725–735. DOI: 10.1007/s00601-012-0455-6.

[13] C. Ji, C. Elster, and D. R. Phillips. ^{6}He nucleus in halo effective field theory. *Phys. Rev.* **C90**.4 (2014), 044004. DOI: 10.1103/PhysRevC.90.044004. arXiv: 1405.2394 [nucl-th].

[14] G. Hagen et al. Efimov Physics Around the Neutron-Rich ^{60}Ca Isotope. *Phys. Rev. Lett.* **111** (2013), 132501. DOI: 10.1103/PhysRevLett.111.132501. arXiv: 1306.3661 [nucl-th].

[15] B. Acharya, C. Ji, and D. Phillips. Implications of a matter-radius measurement for the structure of Carbon-22. *Phys. Lett.* **B723** (2013), 196–200. DOI: 10.1016/j.physletb.2013.04.055. arXiv: 1303.6720 [nucl-th].

[16] H.-W. Hammer and D. R. Phillips. Electric properties of the Beryllium-11 system in Halo EFT. *Nucl. Phys.* **A865** (2011), 17–42. DOI: `10.1016/j.nuclphysa.2011.06.028`. arXiv: `1103.1087 [nucl-th]`.

[17] G. Rupak, L. Fernando, and A. Vaghani. Radiative Neutron Capture on Carbon-14 in Effective Field Theory. *Phys. Rev.* **C86** (2012), 044608. DOI: `10.1103/PhysRevC.86.044608`. arXiv: `1204.4408 [nucl-th]`.

[18] B. Acharya and D. R. Phillips. Carbon-19 in Halo EFT: Effective-range parameters from Coulomb-dissociation experiments. *Nucl. Phys.* **A913** (2013), 103–115. DOI: `10.1016/j.nuclphysa.2013.05.021`.

[19] X. Zhang, K. M. Nollett, and D. Phillips. Marrying *ab initio* calculations and Halo-EFT: the case of $^7Li + n \to \,^8Li + \gamma$. *Phys. Rev.* **C89** (2014), 024613. DOI: `10.1103/PhysRevC.89.024613`. arXiv: `1311.6822 [nucl-th]`.

[20] R. Higa, H.-W. Hammer, and U. van Kolck. $\alpha\alpha$ scattering in halo effective field theory. *Nucl. Phys. A* **809** (2008), 171. DOI: `10.1016/j.nuclphysa.2008.06.003`.

[21] L. S. Brown and G. M. Hale. Field Theory of the d+t→n+alpha Reaction Dominated by a 5He* Unstable Particle. *Phys. Rev.* **C89** (2014), 014622. DOI: `10.1103/PhysRevC.89.014622`. arXiv: `1308.0347 [nucl-th]`.

[22] D. B. Kaplan, M. J. Savage, and M. B. Wise. A Perturbative calculation of the electromagnetic form-factors of the deuteron. *Phys. Rev.* **C59** (1999), 617–629. DOI: `10.1103/PhysRevC.59.617`. arXiv: `nucl-th/9804032 [nucl-th]`.

[23] X. Kong and F. Ravndal. Proton proton scattering lengths from effective field theory. *Phys. Lett.* **B450** (1999), 320–324. DOI: `10.1016/S0370-2693(99)00144-6`. arXiv: `nucl-th/9811076 [nucl-th]`.

[24] X. Kong and F. Ravndal. Coulomb effects in low-energy proton proton scattering. *Nucl. Phys.* **A665** (2000), 137–163. DOI: `10.1016/S0375-9474(99)00406-6`. arXiv: `hep-ph/9903523 [hep-ph]`.

[25] X. Kong and F. Ravndal. Proton proton fusion in leading order of effective field theory. *Nucl. Phys.* **A656** (1999), 421–429. DOI: `10.1016/S0375-9474(99)00314-0`. arXiv: `nucl-th/9902064 [nucl-th]`.

[26] S.-i. Ando and M. C. Birse. Effective field theory of 3He. *J. Phys.* **G37** (2010), 105108. DOI: `10.1088/0954-3899/37/10/105108`. arXiv: `1003.4383 [nucl-th]`.

[27] J. Vanasse et al. ^{3}He and *pd* Scattering to Next-to-Leading Order in Pionless Effective Field Theory. *Phys. Rev. C* **89** (2014), 064003. DOI: `10.1103/PhysRevC.89.064003`. arXiv: `1402.5441 [nucl-th]`.

[28] X. Zhang, K. M. Nollett, and D. Phillips. Marrying ab initio calculations and Halo EFT: the case of $^7Be + p \to \,^8B + \gamma$. *Phys. Rev.* **C89** (2014), 051602. DOI: `10.1103/PhysRevC.89.051602`. arXiv: `1401.4482 [nucl-th]`.

[29] J. Huang, C. Bertulani, and V. Guimaraes. Radiative capture of nucleons at astrophysical energies with single-particle states. *Atom. Data Nucl. Data Tabl.* **96** (2010), 824. DOI: `10.1016/j.adt.2010.06.004`. arXiv: `0810.3867 [nucl-th]`.

[30] C. Gagliardi et al. Tests of transfer reaction determinations of astrophysical S - factors. *Phys. Rev.* **C59** (1999), 1149–1153. DOI: `10.1103/PhysRevC.59.1149`. arXiv: `nucl-ex/9811005 [nucl-ex]`.

[31] R. Morlock et al. Halo Properties of the First 1/2+ State in F17 from the O16(p,γ)F17 Reaction. *Phys. Rev. Lett.* **79** (1997), 3837–3840. DOI: `10.1103/PhysRevLett.79.3837`.

[32] S. König, D. Lee, and H.-W. Hammer. Causality constraints for charged particles. *J. Phys. G: Nucl. Part. Phys.* **40** (2013), 045106. DOI: `10.1088/0954-3899/40/4/045106`.

[33] K. M. Nollett and R. Wiringa. Asymptotic normalization coefficients from ab initio calculations. *Phys. Rev.* **C83** (2011), 041001. DOI: `10.1103/PhysRevC.83.041001`. arXiv: `1102.1787 [nucl-th]`.

[34] P. Navrátil, R. Roth, and S. Quaglioni. Ab initio many-body calculation of the 7Be(p,gamma)8B radiative capture. *Phys. Lett.* **B704** (2011), 379–383. DOI: `10.1016/j.physletb.2011.09.079`. arXiv: `1105.5977 [nucl-th]`.

[35] G. Tabacaru et al. Scattering of Be-7 and B-8 and the astrophysical S(17) factor. *Phys. Rev.* **C73** (2006), 025808. DOI: `10.1103/PhysRevC.73.025808`. arXiv: `nucl-ex/0508029 [nucl-ex]`.

[36] B. Filippone et al. Measurement of the Be-7 (p, gamma) B-8 Reaction Cross Section at Low Energies. *Phys. Rev. Lett.* **50** (1983), 412–416. DOI: `10.1103/PhysRevLett.50.412`.

[37] F. Hammache et al. New measurement and analysis of the Be-7 (p, gamma) B-8 cross-section. *Phys. Rev. Lett.* **80** (1998), 928–931. DOI: `10.1103/PhysRevLett.80.928`. arXiv: `nucl-ex/9712003 [nucl-ex]`.

[38] F. Hammache et al. Low-energy measurement of the Be-7(p,gamma) B-8 cross-section. *Phys. Rev. Lett.* **86** (2001), 3985–3988. arXiv: `nucl-ex/0101014 [nucl-ex]`.

[39] M. Hass et al. A new measurement of the Be-7(p,gamma)B-8 cross-section with an implanted Be-7 target. *Phys. Lett.* **B462** (1999), 237–242. DOI: `10.1016/S0370-2693(99)00926-0`.

[40] F. Strieder et al. Absolute cross section of 7Be(p,gamma)8B. *Nucl. Phys.* **A696** (2001), 219–230. DOI: `10.1016/S0375-9474(01)01121-6`.

[41] L. Baby et al. A New precision measurement of the Be-7(p,gamma) B-8 cross-section with an implanted Be-7 target. *Phys. Rev. Lett.* **90** (2003), 022501. DOI: `10.1103/PhysRevLett.90.022501`. arXiv: `nucl-ex/0208005 [nucl-ex]`.

[42] A. Junghans et al. Precise measurement of the Be-7(p,gamma) B-8 S factor. *Phys. Rev.* **C68** (2003), 065803. DOI: `10.1103/PhysRevC.68.065803`. arXiv: `nucl-ex/0308003 [nucl-ex]`.

[43] A. Junghans et al. Updated S factors for the Be-7 (p, gamma) B-8 reaction. *Phys. Rev.* **C81** (2010), 012801. DOI: `10.1103/PhysRevC.81.012801`.

[44] E. Adelberger et al. Solar fusion cross sections II: the pp chain and CNO cycles. *Rev. Mod. Phys.* **83** (2011), 195. DOI: `10.1103/RevModPhys.83.195`. arXiv: `1004.2318 [nucl-ex]`.

[45] X. Zhang, K. M. Nollett, and D. R. Phillips. Halo effective field theory constrains the solar ^{7}Be + p → ^{8}B + γ rate. *Phys. Lett.* **B751** (2015), 535–540. DOI: `10.1016/j.physletb.2015.11.005`. arXiv: `1507.07239 [nucl-th]`.